Bidirectional Electric Vehicle Charger Control

Houssein Al Attar

CENTRALE NANTES

THÈSE DE DOCTORAT DE

L'ÉCOLE CENTRALE DE NANTES

ÉCOLE DOCTORALE N° 601
Mathématiques et Sciences et Technologies de l'Information et de la Communication
Spécialité : *Génie Électrique*

Par
Houssein AL ATTAR

Bidirectional Electric Vehicle Charger Control

Thèse présentée et soutenue à l'Ecole Centrale de Nantes, le 14 octobre 2022
Unité de recherche : UMR 6004, Laboratoire des Sciences du Numérique de Nantes (LS2N)

Rapporteurs avant soutenance :

Marco LISERRE — Full Professor, Christian-Albrechts-Universität zu Kiel, Allemagne
Hervé GUEGUEN — Professeur des Universités, CentraleSupélec Campus Rennes, Cesson-Sévigné

Composition du Jury :

Président :	Patrick COIRAULT	Professeur des Universités, Université de Poitiers
Examinatrices :	Zohra KADER	Maître de conférences, INP de Toulouse
	Miassa TALEB	Ingénieure de recherche, Renault, Guyancourt
Dir. de thèse :	Malek GHANES	Professeur des Universités, Ecole Centrale de Nantes
Co-encadrant :	Mohamed HAMIDA	Maître de conférences, Ecole Centrale de Nantes

Acknowledgement

This work was carried out within the Chair of Renault-Centrale Nantes, in the Laboratory of Digital Sciences of Nantes (Laboratoire des Sciences du Numérique de Nantes LS2N) within the CODEx team.

First of all, I would like to thank from the bottom of my heart my supervisors, my thesis director Malek GHANES, my co-supervisor Mohamed HAMIDA and my supervisor in Renault Miassa TALEB, for the quality of their support, their precious advice, and their confidence during these three years of research in order to produce this brilliant work.

Then, I would like to thank deeply the members of the jury for their participation and their evaluation of this dissertation: Marco LISERRE and Hervé GUEGUEN, for having accepted the task of being reporters for this dissertation; as well as Patrick COIRAULT and Zohra KADER as examiners.

I would also like to thank the administrative team of the Ecole Centrale de Nantes for ensuring that the work is carried out under the right conditions.

Ever since I can remember, my parents and relatives have supported me in every step and given me the courage and confidence that got me here.

I couldn't have undertaken this journey without my wife who was always by my side, giving me all the emotional and practical support I could ever need.

Table of Contents

List of Figures

List of Tables

List of Symbols

EV	Electric Vehicle
$G2V$	Grid to Vehicle
$V2G$	Vehicle to Grid
$V2H$	Vehicle to Home
$V2L$	Vehicle to Load
$V2X$	Vehicle to Everything
PFC	Power Factor Correction
DAB	Dual Active Bridge
SRC	Series Resonant Converters
PFM	Pulse Frequency Modulation
PWM	Pulse Width Modulation
PSM	Phase Shift Modulation
GI	Gain Inversion
MFC	Model Free Control
AST	Adaptive Super Twisting
$SVPWM$	Space Vector Pulse Width Modulation
L_r	Series inductor of LLC converter
C_r	Series capacitor of LLC converter
L_m	Parallel inductor of LLC converter
ZVS	Zero Voltage Switching
ZCS	Zero Current Switching
n	Transformer ratio
V_{DC}	DC bus voltage
V_b	Battery voltage
P	Converter Power
FHA	First Harmonic Approximation
EDF	Extending Describing Function
f_{0c}	Feedforward switching frequency in G2V
f_{0d}	Feedforward switching frequency in V2X
X	Full decision vector
f_{min}	Minimum authorized switching frequency
f_{max}	Maximum authorized switching frequency

General Introduction

0.1 Framework and problem statement

Community involvement is necessary to build an all-electric future that benefits everyone. Pollution problems have become more and more worrying in recent years, and the development of low-polluting or completely "clean" vehicles has taken on great importance.

Photovoltaic, wind, fuel cell, battery, and supercapacity technologies are among the promising renewable energy and energy storage sources for easing the global power-generation crisis. In order to take advantage of the fluctuating nature of renewable energy systems, power electronic converters have become a crucial component of power systems from generation to distribution sectors [4]. A bidirectional converter is frequently used as an interface for Energy Storage Systems (ESSs).

Several means of transport of low-polluting type are currently being developed by major automobile manufacturers. Understanding the advantages of electric mobility over the unsustainable usage of Internal Combustion Engines (ICE) can clarify the reason why the popularity of Electric Vehicles (EVs) is increasing. The usage of ICE has played a significant role in the overall production of greenhouse gases (GHGs), degradation of the environment, and climate change over years [5]. As a result of this detrimental effect, an uprising appeared to find a sustainable solution to the degrading effect brought on by the continued usage of ICE vehicles. Different countries around the world have established different objectives and aim to develop green energy. The EV is one mean by which this goal might be attained. The EV might have a huge impact on the society. It represents the main support of the e-mobility as presented in Figure 1. Using an EV can help to minimize CO2 emissions and health concerns caused by smog.

Figure 1 – Overview of e-mobility ecosystem [1]

Battery charging is an important element to take into account for the development of EVs. Different systems have been developed trying to best meet charging requirements. Two major types of EV chargers have been defined: OnBoard or AC chargers and OffBoard or DC chargers (see Figure 2).

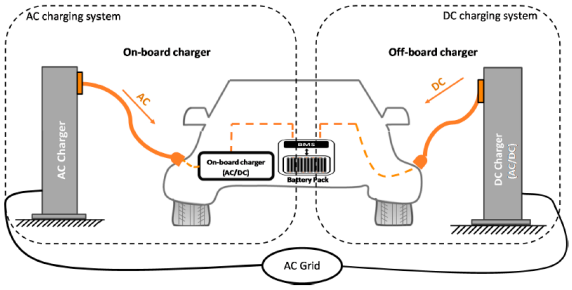

Figure 2 – OnBoard and OffBoard chargers [2]

The OnBoard charger is generally embedded in the vehicle. It is often designed for lower kilowatts of power transfer. The main advantage of the "classic" charger is the ability to connect easily (use of the classic socket) and to fully charge the battery pack ensuring its longevity. Its main drawbacks are that it requires a long charging time and adds significant weight and cost to the vehicle. In contrast, the characteristics of OffBoard chargers make it possible to play the role of "station service" and can be adopted with higher power transfer (>50 kW) and output voltages [6]. However, the installation of these infrastructures (terminals, inductive chargers) requires large financial means, which will limit their number and therefore their interest.

Despite the special efforts that have been made to reduce the cost and volume of chargers, the OnBoard charger remains for the car manufacturer a penalizing element for the EV.

EVs have a High Voltage (HV) Li-on battery pack beside an OnBoard charger. Figure 3 shows a typical setup of the EV's power management system. For safety purposes, galvanic isolation is normally enforced between the battery pack and the grid-side DC link [7].

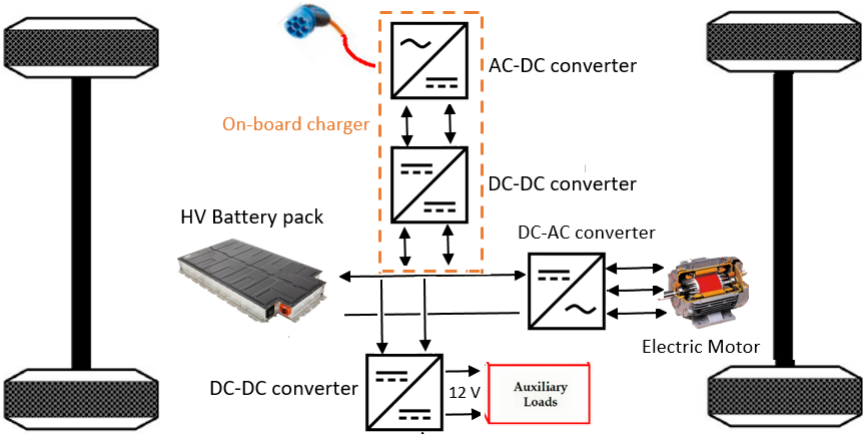

Figure 3 – EV power management system

The notion of Grid to Vehicle (G2V) describes how electric vehicle batteries are charged from the power grid. By integrating the bidirectional charger technology, it becomes possible to deliver energy in the other direction, from EV batteries to Grid (V2G) or to Home/Load (V2H/L). The energy stored in the EV battery can then be used as a current source (in V2G) or a voltage source (in V2H/V2L). Vehicle to Everything (V2X) mode is the name given to the battery discharging operating mode. EVs, according to this concept, are not only electrical loads, but also an electrical energy storage. An EV in V2X mode offers reactive and active power regulation, load balancing, and tracking of variable renewable energy sources [8]. The battery charger must then be able to ensure the conversion in both directions of energy flow, and thus becomes bidirectional: charging/discharging. As a result, EVs with bidirectional battery chargers [9] can be connected into the smart grid, transforming the energy market dramatically. As shown in Figure 4, the EV charger can be considered as the association of two conversion stages: an AC-DC part followed by an isolated DC-DC converter.

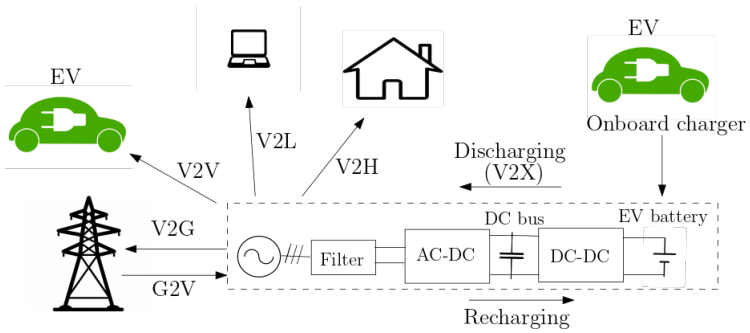

Figure 4 – EV bidirectional charger topology

Both functions (charging or G2V and discharging or V2X) are provided by the charger, presented in Figure 4, composed of bidirectional AC-DC and DC-DC converters.
The AC-DC converter is a Power Factor Correction (PFC), which is used to ensure the grid current control. Meanwhile, the DC-DC converter is used to maintain the DC bus voltage and guarantee the battery charging/discharging without any voltage ripple.

The choice of the topology of AC-DC and DC-DC converters defines the characteristics of the charger. More elements (inductors or capacitors) in the converter structure will maybe increase its efficiency, but apparently the size will increase and the charger cost will be higher. First of all, to guarantee the bidirectional charger operation, the converters should be able to operate in the two directions with a high efficiency. The AC-DC converter in G2V mode becomes a DC-AC converter in V2G mode and the DC-DC converter should be reversible. A tradeoff between the complexity of the converter design, the complexity of the control, and the high efficiency should be taken into account.

An OnBoard battery charger is constrained by sizing, weight, and cost. It should be implemented either with a unidirectional or bidirectional power flow. The dimensions of

the DC-DC converter are an essential part of the OnBoard charger sizing. The advantages of decreasing DC-DC converter's dimensions include a reduced sizing, weight, and cost of the charger and an improved reliability.

Isolated bidirectional DC-DC converters [10, 11, 12] are used as a key device for interfacing the storage devices between a DC bus and a battery with high power applications. There are many topologies of isolated converters, such as Dual Active Bridge (DAB) converters [13] and Series Resonant Converters (SRC) [14], but they suffer from soft switching property loss at high input voltage and with light load. DC-DC LLC resonant converters [15, 16, 17, 18] are commonly selected for applications that demand a high power density, such as the EV charger.

In this thesis, the full-bridge DC-DC LLC resonant converter [19, 15] and its control are investigated to suit the application features of the bidirectional EV charger, which include a wide range of battery voltage and high power density [20, 21].

The use of DC-DC LLC converters is common in numerous industrial applications [22]. The DC-DC LLC resonant converter is a popular isolated DC-DC topology because of its appealing advantages: Zero-Voltage Switching (ZVS) for power MOSFETs, and Zero-Current Switching (ZCS) for the diodes in a wide operating zone; simple circuit setup with low components count; and high power density with high switching frequency [23].

For DC-DC LLC resonant converters, the most frequently adopted modulation strategy is Pulse Frequency Modulation (PFM). The switching frequency feasible zone is defined between minimum and maximum authorized values to guarantee ZVS conditions. This frequency feasibility constraint provides a cost minimization challenge related to both software and hardware implementation in the EV charger. However, when the PFM strategy is adopted for wide input/output voltage and power ranges in the OnBoard battery charger in V2X mode, a wide operating switching frequency range is required to meet the system voltage gain requirement. This wide switching frequency range causes a loss in the soft switching operation [18, 24], which results in a low conversion efficiency and control performance.

DC-DC LLC converters with the PFM strategy are not preferred in wide voltage range applications due to the following: large switching frequency variations are necessary that reduce the performance of the converter's Electro-Magnetic Interference (EMI); designing and optimizing magnetic components is difficult; converter efficiency is reduced due to higher conduction and circulating current losses; and power density is reduced due to the large size of the magnetic components. Furthermore, in the case of low power loads, the PFM strategy causes an efficiency degradation and low control performance due to a wide switching frequency demand. As a result, DC-DC LLC converters that operate at a fixed switching frequency are favorable in applications involving a large voltage gain range and can effectively address the aforementioned problems. According to the existing literature, there are two categories of control techniques for DC-DC LLC converters that use fixed switching frequency: Phase-Shift Modulation (PSM) and Pulse Width Modula-

tion (PWM). These two startegies will be investigated in the thesis to improve the control performance within a wide range of the battery voltage and high power density, as well as avoid the PFM strategy limitations (efficiency degradation at low power loads, switching frequency saturation,...).

In the last phase of this thesis, another EV charger topology, which had not been scheduled from the thesis beginning, is studied. A bidirectional single-phase EV charger including the DAB converter topology is studied. Unlike resonant converters, such as SRC and LLC that use auxiliary inductors and capacitors, DAB uses fewer passive components which makes it easier to control, less expensive in terms of cost, and less in space. The high frequency transformer that DAB uses to achieve galvanic isolation increases protection and guarantees that charging standards are met in high voltage applications like EV chargers.

0.2 Motivation

This work is conducted in the frame of the the project Chair between Centrale Nantes and Renault about EV performances. It is classified under the research axis about energy management and control of the EV charging and static converters.
The aim of this thesis is to carry out an investigation on control strategies design of the bidirectional EV charger in order to improve the performance and the efficiency. A part of the dissertation is dedicated to provide an optimized design of the structure which is beneficial for the manufacturer to reduce the cost and the charger sizing. DC-DC converters (such as LLC and DAB) for EV charger application are studied. Many modulation strategies are implemented and compared in order to improve the converter feasibility zone and cover the whole operating zone of the EV charger. Robust non-linear control laws are proposed as well to ensure the robustness with respect to unexpected disturbances. The control techniques are applied to the bidirectional EV charger, including the AC-DC converter, and simulated for real EV charger models in both G2V and V2G modes.

Consequently, this thesis would be of benefit to the following:

- Academic and Research Institutions: the thesis would act as a standard for researchers that examine applications for EV chargers
- EV Automobile Company: the thesis will be helpful to the manufacturers of EVs, like Renault and others
- Investors: the study will encourage both public and private investment in the field of EV charging technology
- Users of EV: electric car owners can expand their knowledge in the EV charging process.

0.3 Thesis organisation and contributions

Chapter 1: State of the art: The aim of this chapter is to provide a literature review of different bidirectional DC-DC converter topologies, as presented in Section 1.2, in order to highlight the advantages and limitations of each of them and provide a comparative study in terms of converter efficiency, design and control complexity. Furthermore, Section 1.3 introduces the principle of several modulation strategies to control the DC-DC converters, such as Pulse Frequency Modulation (PFM), Pulse Width Modulation (PWM) and Phase Shift Modulation (PSM).

On the other hand, the goal of Section 1.4 is to study the bidirectional DC-DC LLC resonant converter for high power applications like EV charger, to present modelling approaches such as large and small signal modelling, and different control and optimization strategies proposed in the literature. Section 1.5 focuses on the control techniques implemented for an EV charger in G2V and V2G modes.

Chapter 2: Modulation Strategies and Optimized Design of LLC Converter: To the best of our knowledge, existing control solutions for the DC-DC LLC converter are mostly related to battery voltage or DC current regulations. The new challenge of this chapter is to ensure the DC bus voltage control and improve the efficiency within both power and battery voltage ranges in V2X mode. The main contribution leads to design the control laws based on the DC-DC LLC transfer function Gain Inversion (GI). Three conventional modulation strategies based on an averaged small signal DC-DC LLC dynamic model converter with First Harmonic Approximation (FHA) are presented in Section 2.2. PFM is firstly studied. Then, PWM and PSM based GI control are designed to avoid PFM drawbacks. The benefits and the limitations of each strategy are highlighted. A comparative study between the different strategies is conducted with respect to the control performance and converter efficiency.

From another perspective, the new challenge of Section 2.3 is to design an optimization strategy to minimize the DC-DC LLC converter cost and improve the control frequency feasibility zone, for a wide variation of battery voltage and converter power, in the charging (G2V) and discharging (V2X) modes simultaneously. To the best of our knowledge, this optimization problem, in the case of a bidirectional (G2V and V2X) charger, is not yet considered in the literature. An optimal design that considers the control stability equations in the optimization algorithm is elaborated. The obtained results show a significant converter cost decrease and important expansion of control frequency feasibility zones. A comparative study between initial and optimized values, in G2V and V2X modes, is conducted according to the converter efficiency.

Chapter 3: Robust Control Strategies Design of LLC Converter: The main contribution of this chapter is to provide robust control laws combined with the PSM strategy in order not only to cover the whole operating zone but also to guarantee the robustness against different disturbances and uncertainties in the DC-DC LLC converter system.

Section 3.2 highlights a control strategy based on the Model Free Control (MFC). The control law is implemented without the prior knowledge of the mathematical and complex model of the DC-DC LLC converter.

The new challenge of Section 3.3 is threefold. Firstly, an improved model of the DC-DC LLC converter based on the PSM strategy is developed. The aim of this model is to provide enough information of the LLC dynamics (partially known) in order to get a system's relative degree equal to one with respect to the control (i.e. the DC bus voltage in function of the phase shift), to be used in the control design in Section 3.3.2. It also helps to provide a stability proof of the internal LLC converter dynamics in Section 3.3.3. Secondly, the non-linear Adaptive Super Twisting Control (ASTC) combined with the PSM strategy is proposed in Section 3.3.2. The existing control laws applied to the PSM are based on the PI controller which requires the knoweldge of the LLC model and disturbances' boundaries making them less robust. From here appears the importance of a non-linear robust control, such as the ASTC, which can be implemented without the knoweldge of the boundaries of disturbances (current and voltage disturbance, parameter's variation) existing in the LLC model. The effect of disturbances is effectively compensated by the adaptive control gain of the ASTC with no control gain overestimation and chattering reducing compared to other sliding mode controllers. Moreover, to the best of our knowledge, the stability of the DC-DC LLC converter dynamics has not been adequately examined while the PSM strategy is applied due to the LLC model's complexity. Thus, the third main contribution, in Section 3.3.3, consists of developing a formal stability proof of the DC-DC LLC converter dynamics, using the small signal perturbation theory, to provide necessary requirements for the ASTC stability.

To verify the effectiveness of the proposed control strategies, simulation results are presented in Section 3.3.4 under several disturbances, which demonstrate a great agreement with the theoretical analysis. A comparison of the ASTC, and MFC and the conventional control laws is conducted in terms of the control performance and efficiency, proving the advantage of the PSM strategy combined with robust control laws (ASTC and MFC).

Chapter 4: Bidirectional Electric Vehicle Charger Control This chapter proposes a hybrid control strategy for the bidirectional EV charger to ensure DC bus voltage and grid current control for the whole operating zone of the bidirectional EV charger. Compared to the literature, a bidirectional EV charger including an AC-DC Vienna topology connected to two DC-DC LLC converters is studied in this chapter. In order to avoid the PFM strategy drawbacks when the DC-DC LLC converter is saturated in both G2V and V2G modes, different solutions are proposed to improve the performance and the efficiency. In chapter 2, modulation strategies with fixed switching frequency (PWM and PSM) are proposed to improve the DC-DC LLC converter performance in V2G mode. In this chapter, the aim is to compare the performance when the DC-DC LLC converter is alone as studied in chapter 2, and when it is implemented in the EV charger. In Section 4.4, two approaches, in G2V mode, are presented and implemented for the DC-DC LLC converter

in the EV charegr. Section 4.4.1 presents the PFM strategy with variable DC bus request. Section 4.4.2 focus on the design of a backstepping control strategy to control the DC bus by the help of the AC-DC converter. Section 4.5 highlights the PSM strategy, applied to the DC-DC LLC converter alone in chapter 2, in order to avoid the PFM limitation in V2G mode. Outside of the saturation zones, PFM strategy is still applied. Compared to the DC-DC LLC converter alone, the results highlight the advantage of the proposed control strategies in improving the charger efficiency and control performance in both G2V and V2G modes.

Chapter 5: Bidirectional DAB Charger Control In this chapter, another topology of the bidirectional EV charger is studied. A single phase charger with the DAB topology is highlighted. The interest in this topology, compared to the LLC resonant one, arises from the fact that it provides less components which is beneficial in terms of cost, and easier to control. A state of the art about the control of DAB converters is presented in Section 5.2. Most existing work in the literature focused on the study of different modulation strategies for the DAB converter alone or as a part of an EV charger either in an open loop without a phase shift control law or in a battery voltage or current closed loop without any power factor correction. The charger's synoptic is described in Section 5.3. In Section 5.4, different modulation strategies, such as Single Phase Shift (SPS) and Dual Phase Shift (DPS), are highlighted with their main advantages and drawbacks. Section 5.5 develops the proposed control strategy for the DAB charger that aims to ensure the control of the AC grid current and the DC bus voltage, as well as improve the charger efficiency in both G2V and V2G modes. The modulation strategies are implemented based on the proposed control algorithm. Section 5.6 presents the simulation results, based on a real-world DAB charger model, for some operating points in order to validate the effectiveness of the proposed control strategy. A comparative study between SPS and DPS modulations is conducted in terms of the control performance and charger efficiency.

General Conclusion This part draws the conclusion of this thesis by highlighting the main contributions and results and opening future perspectives.

0.4 Publications

This thesis has given rise to 5 patents submitted to INPI, one journal paper published and one submitted, 4 international conferences and 1 book chapter accepted.

0.4.1 Patents

– Al Attar Houssein, Taleb Miassa, Ghanes Malek, and Maloum Abdelmalek (2021). Stratégie de commande PSM d'un convertisseur DCDC LLC par inversion de gain dans le mode V2X pour application VE. Submitted to INPI. PJ-21-0039. [25]

- Al Attar, H., Taleb, M., Hamida, M., and Maloum, A. (2021). Stratégies de commande PWM d'un convertisseur DCDC LLC par inversion de gain dans le mode V2X pour application VE. Submitted to INPI. PJ-21-0024. [26]
- Al Attar Houssein, Ghanes Malek, Hamida Mohamed, and Taleb Miassa, (2021). Control performances improvement for bidirectional EV charger. Submitted to INPI. PJ-21-0544. [27]
- Al Attar Houssein, Ghanes Malek, Hamida Mohamed, and Taleb Miassa, (2022). Adaptive control design of DC-DC LLC converter with phase shift modulation in V2X mode for EV charger application. Submitted to INPI. PJ-22-0011. [28]
- Al Attar Houssein, Ghanes Malek, Hamida Mohamed, and Taleb Miassa, (2022). Model Free Control design of DC-DC LLC converter with phase shift modulation in V2X mode for EV charger application. Submitted to INPI. PJ-22-0009. [29]

0.4.2 Journal papers

- Al Attar Houssein, Ghanes Malek, Hamida Mohamed, and Taleb Miassa, *LLC DC-DC Converter Performances Improvement for Bidirectional Electric Vehicle Charger Application*, World Electric Vehicle Journal, 13(1), 2022. (published) [21]
- Al Attar Houssein, Hamida Mohamed, Ghanes Malek, Barbot Jean Pierre and Taleb Miassa, *Adaptive Control Design and Stability Analysis of the Bidirectional DC-DC LLC Converter*, IEEE Transactions on Control Systems Technology, 2022. (submitted) [30]

0.4.3 Conference papers

- Al Attar Houssein, Ghanes Malek, Hamida Mohamed, and Taleb Miassa, *Control strategies design and comparison of DC-DC LLC converter in V2X mode for electric vehicle charger application*, 2021 IEEE Conference on Control Technology and Applications (CCTA), San Diego, Unites States, August 08-11, 2021, pp. 1154-1159 (published) [20]
- Al Attar Houssein, Ghanes Malek, Hamida Mohamed, and Taleb Miassa, *Model Free Control Design of DC-DC LLC Converter with Phase Shift Modulation in V2X Mode for EV Charger Application*, 2022 IEEE Conference on Control Technology and Applications (CCTA), Trieste, Italy, August 22-25, 2022 (accepted) [31]
- Al Attar Houssein, Ghanes Malek, Hamida Mohamed, and Taleb Miassa, *Electric Vehicle Charger Control Design Combining Phase Shift Modulation with an Adaptive Super Twisting Algorithm*, 2022 IEEE 16th International Workshop on Variable Structure Systems VSS, Rio de Janeiro, Brazil, September 11-14, 2022 (accepted) [32]

– Al Attar, H., Hamida, M. A., Ghanes, M., and Taleb, M., *Bidirectional Electric Vehicle Charger Control Design with Performance Improvement*, 2022 IEEE Conference of the Industrial Electronics Society (IECON), Brussels, Belgique, October 17-20, 2022 (accepted) [33]

0.4.4 Book chapters

– Al Attar Houssein, Ghanes Malek, Hamida Mohamed, and Taleb Miassa, *DC-DC Converters: Modelling and Control Strategies*, in Power Electronics Converters and their Control for Renewable Energy Applications, Elsevier, 2023 (accepted) [34]

1

State of the art

1.1 Introduction

The microgrid's stability, resilience, and power quality are all enhanced by having reliable energy storage devices [21, 8, 35]. Batteries or energy storage devices can be connected to the microgrid on their own or in conjunction with a distributed energy supply. Regardless of the microgrid type, DC-DC converters play a critical role in interfacing Distributed Energy Storage (DES) devices with the microgrid [36, 37]. Bidirectional DC-DC Converters (BDC) [10, 11, 12] are increasing in importance. BDC are frequently chosen for applications requiring great power density and energy efficiency, such as electric vehicle chargers and renewable energy systems. With this topology, power can flow in both directions and the converter could be used as a buck-boost converter in the forward and reverse modes. DC-DC converters can be found in many areas. The construction of interface systems, like bidirectional chargers, between the grid and vehicle energy storage is one of the most technologically challenging aspects of implementing energy management systems. Most existing topologies of bidirectional isolated DC-DC converters are studied in this chapter. The characteristics and the limitations of each topology are highlighted. A comparative study between these topologies is conducted in terms of some essential parameters (efficiency, design complexity, soft switching, control strategies and reversibility).

Several modulation strategies are applied for DC-DC converters to generate the switches (MOSFETs) control signals. The principle of PFM, PWM and PSM strategies is presented in this chapter.

There are many topologies of DC-DC converters, such as Dual Active Bridge (DAB) converters [13, 38] and Series Resonant Converters (SRC) [14], that are implemented in

the industrial applications. However, they suffer from soft switching property loss at high input voltage and with light load. For applications that require a high power density and good energy efficiency, resonant DC-DC converters are widely used. The isolated bidirectional DC-DC LLC resonant converter [18, 39] is widely taken into account for control purposes in order to improve converter efficiency over a wide range of power and input/output voltages in industrial applications [21, 15]. The large signal model based on Extending Describing Function (EDF) [40, 41, 42] is proposed for the DC-DC LLC converter. When big signal transient disruption occurs, these models give sufficient dynamic information of the DC-DC LLC converter. However, because these models are nonlinear, the control's design is more difficult. Small signal modelling [20, 21, 43] consists of using harmonic approximation to obtain more simplified model. Small signal transfer functions can be derived which is more comfortable with control strategies design. For DC-DC LLC resonant converter, the most frequently adopted modulation strategy is PFM. However, when PFM strategy is adopted for a wide input/output range application in reverse operating mode, there is a low conversion efficiency. Therefore, many different modulation strategies such as PWM and PSM strategies are proposed to increase the DC-DC LLC converter feasibility operating with an improved efficiency. Control laws, such as PI and sliding mode controllers, are proposed and implemented in the literature beside the adopted modulation strategy for the DC-DC LLC converter.

Furthermore, in terms of hardware, several research works studied the DC-DC LLC converter in order to improve the efficiency by an optimized design of the LLC structure. Finding the optimal values of the DC-DC LLC converter inductor and capacitor affects directly the control performance and leads to reduce the volume and the cost that is beneficial especially for industrial applications.

Isolated bidirectional DC-DC converters [10, 11, 12] are used as a key device for interfacing the storage devices. Electric mobility represents a significant technology of transport for the society, resulting in more efficient mobility. This technology of transport is mainly supported by EV, where the batteries are charged from the power grid, which defines the concept of Grid-to-Vehicle (G2V). However, it is possible to send energy in the opposite way, i.e. from the EV batteries to the power grid in the concept of Vehicle-to-Grid (V2G). An EV in V2G mode offers reactive and active power regulation, load balancing, and tracking of variable renewable energy sources [8]. The bidirectional EV charger is one of the main applications of the bidirectional isolated DC-DC converters. In this technology, BDC are presented between a DC bus link connected to an AC-DC converter and a high voltage battery pack, in order to ensure the battery charging/discharging. The control strategy of the EV charger consists of two control algorithms: AC-DC and DC-DC controllers. The controllers should be implemented in order to ensure the grid, DC bus and battery stability. Different control laws are implemented in the literature for the AC-DC and DC-DC converters in the EV charger.

Based on this state of the art, our book chapter [34] has been produced.

1.2 Bidirectional DC-DC converters for high power applications

1.2.1 Overview

There are two big families of DC-DC converters: Non isolated and isolated converters. Non isolated converters [44] consist of transferring the energy from one side to the other one without isolation stage between the two sides. On the other hand, isolated converters come in a variety of topologies and offer the electrical isolation between the input and the output sides with a high frequency transformer. Therefore, the study in this chapter concentrate on the family of isolated bidirectional DC-DC converters.

Safety of design

Under all operating circumstances, insulation and galvanic separation must be permitted for the duration of the battery charger's service life. Thus, to achieve galvanic isolation and safe operation, an isolated transformer is typically used between the AC side and battery pack [45]. Therefore, while having a simple construction, being inexpensive, having fewer components, being compact in size, and being lightweight, basic non-isolated DC-DC converters like buck converters and boost converters cannot be employed in EV charging applications [46]. To handle the wide range of battery voltages in the battery charging system, isolated converter has the capacity to deliver a greater output voltage with varying turns ratios of the transformer.

High power-density

While using a transformer in a DC-DC converter can boost reliability and offer galvanic isolation, it also makes the system bulkier, heavier, and more expensive than non-isolated chargers [47]. Due to the possibility of minimizing the volume of the transformer and other magnetic and passive components at high frequencies, the converter's overall cost and size are decreased. Therefore, increasing switching frequency is the most efficient way to get a larger power density in an isolated DC-DC converter [47].

Soft switching

DC-DC converters operating can be categorized into two groups: hard switching and soft switching. In Table 1.1, Hard switching and Soft switching are compared [44].

Hard switching	Soft switching
Large switching losses	Near zero switching losses
Limited range of switching frequency	High range of switching frequency
Low efficiency	High efficiency
Low cost	High cost due to more number of components
High EMI due to high di/dt and dv/dt	Low EMI loss
Low power density	High power density
Easy control	Complex control

Table 1.1 – Comparison between hard switching and soft switching

Soft switching is available in two modes: Zero Voltage Switching (ZVS) and Zero Current Switching (ZCS). With ZVS, the voltage across the MOSFET should be canceled before directing it to close [48]. With ZCS, the current flowing through the MOSFET should be eliminated before instructing it to open. ZCS is particularly useful at low converter voltages, where the MOSFETs are subjected to rather high currents.
Power losses during the switching on/off period rise with the switching frequency. Large switching frequencies result in high switching losses and Electro-Magnetic Interference (EMI) emissions, which would subsequently limit the conversion efficiency. Soft-switching technology, such as ZVS and ZCS, is typically used to address this problem [49].

1.2.2 DC-DC converter topologies

Dual Active Bridge (DAB)

An interesting topology is Dual Active Bridge (DAB) converter. Two H bridges are linked by a high frequency transformer with a series inductor as shown in Figure 1.1 [50].

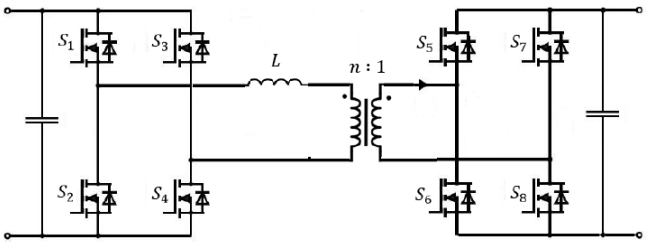

Figure 1.1 – Dual Active Bridge (DAB) converter

Over the last two decades, many studies have been published on this topology, with a focus on its bidirectional feature for energy storage systems. Low device and component stresses, tiny filter components, minimal switching losses (due to ZVS), high power density and efficiency, bidirectional power flow capabilities, buck-boost operation, and low sensitivity to system parasitics are all advantages of this design. Under light load situations,

however, ZVS is lost, and soft-switching is impossible to maintain when the operating voltages at the ports are too high. Nonetheless, great performance and efficiency, as well as the other benefits described above, are noteworthy[50].
Many ways for extending the ZVS operating range have been proposed, and they are based on two primary concepts. The first method involves using extra circuit components such an inductor, a capacitor, and a snubber circuit. While this strategy increases the load range for ZVS, it also causes large conduction losses and raises the design cost. Another option is to phase shift the two half-bridge legs of a full bridge and use ZCS at the left-leg transition and ZVS at the right-leg transition without any additional hardware.
Snubber capacitors are installed across all switches in the DAB, as shown in Figure 1.2, to restrict switching transients, reduce current/voltage spikes, and minimize Electromagnetic Compatibility (EMC) issues associated with high $\frac{dv}{dt}$ [51].

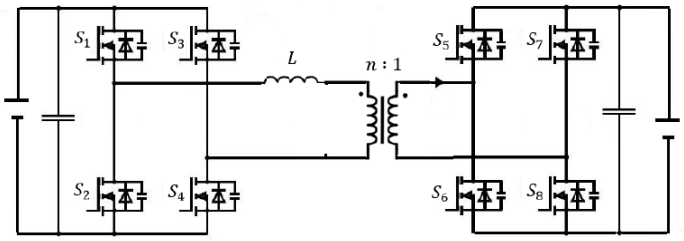

Figure 1.2 – DAB with snubbers

Dual Bridge Series Resonant Converter (DBSRC)

Due to their advantages of operation, resonant converters like the Dual-Bridge Series Resonant Converter (DBSRC) can operate at higher frequencies. For broad fluctuations in load or supply voltage, all switches can work in ZVS or ZCS, which is desirable in many applications. Because the resonant current and voltage are nearly sinusoidal due to the nature of resonance, those parameters can be approximated by merely its fundamental component without sacrificing too much precision for design purposes [52]. Figure 1.3 shows DBSRC [52].

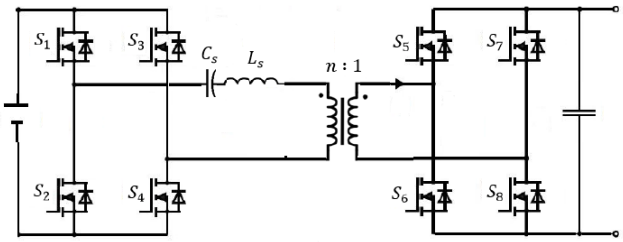

Figure 1.3 – Dual Bridge Series Resonant Converter (DBSRC)

A series LC resonant tank and an HF transformer are used to connect two full bridges. The circuit structure's symmetry allows it to manage bidirectional power flow.

The HF transformer's leakage inductance is employed as part of the resonant inductance. The resonant tank's series capacitor will also assist in blocking the dc current component emerging from any asymmetry in device drop, etc., preventing the transformer from being saturated. For bidirectional power flow, C_s can be split into two portions and placed on both sides of the HF transformer (but having the same value of equivalent capacitance as if solely on the primary side)[52]. It was possible to obtain ZVS for primary-side switches and ZCS for secondary-side switches.

Asymmetric LLC resonant converters

Due to its high efficiency and wide working range, the LLC resonant converter emerges as the most appealing alternative among the several options.
The bidirectional asymmetric LLC resonant converter [15, 17, 18] is presented in Figure 1.4. The resonant tank composes from a series capacitor C_r, a series inductor L_r, a parallel inductor L_m and a high frequency transformer with a turns-ratio of n.

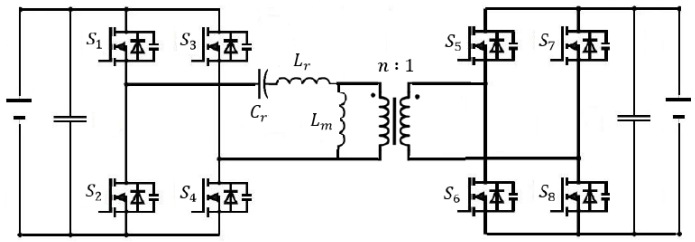

Figure 1.4 – Asymmetric LLC converter

The full-bridge at the primary side is used to apply a square-wave voltage to the resonant tank in the forward mode. There will be a near-sinusoidal alternating current flowing the resonant circuit. To improve the conversion efficiency, the secondary side switches are used for synchronous rectification [17]. Due to the non-symmetric nature of the resonant-tank, the LLC gain transfer function for the reverse mode is different from the forward mode [17]. When the converter is operated in the forward mode, very little power is lost. On the primary side, ZVS is always obtained, while on the secondary side, ZCS is always attained [17]. While in the reverse mode, the converter is expected to produce excellent power conversion efficiency. However, some of the unidirectional originator's intrinsic benefits have been lost. On the secondary side, ZCS is no longer attained, and there is a difficulty to maintain the ZVS range, resulting in lower efficiency. Turn-off currents are large at high output voltages, and switching losses are considerable [17].

CLLC resonant DC-DC converters

Many soft-switching BDC have been acclaimed and extensively documented, with an emphasis on removing switching losses, lowering EMI, and attaining a desirable high-

frequency operational ability and, thus, power density without losing efficiency. CLLC resonant tank is a way to achieve soft switching for the proposed LLC converter. The overall component count may be considerably lowered without any additional soft-switching auxiliary circuits and by being snubberless. The proposed converter also has a very broad input range [53]. Figure 1.5 displays the asymmetric CLLC resonant topology [54].

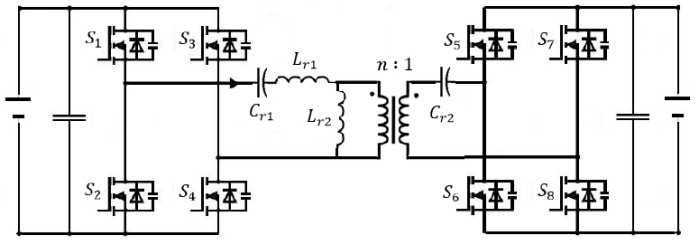

Figure 1.5 – Asymmetric CLLC converter

The resonant inductors L_{r1} and L_{r2} combine the leakage inductor of the transformer's primary and secondary windings. Automatic flux balancing and high resonant frequency are achieved by the resonant capacitors C_{r1} and C_{r2} [53]. Soft switching resonant topologies have recently piqued people's interest. Without any snubber circuits, a bidirectional full-bridge CLLC resonant converter was introduced. This topology can work with primary switches and secondary rectifiers that are soft-switched. Furthermore, without any clamp circuits, the voltage stresses of the power switches are limited to the input and output voltages. Because of the unequal turn numbers of the transformer and the asymmetric construction of the resonant networks, this converter performs differently in forward and backward power conversion modes [53].
Symmetric CLLC resonant network is presented in Figure 1.6 [54].

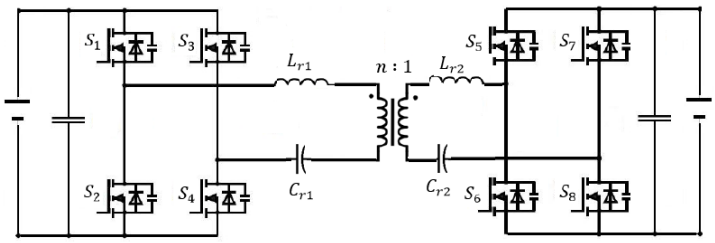

Figure 1.6 – Symmetric CLLC converter

It is clearly seen that the symmetric CLLC is same as Symmetric DBSRC. Because the symmetric CLLC resonant network includes ZVS capability for inverter switches and soft commutation capability for rectifier switches, this converter can operate under high power conversion efficiency. Furthermore, because the switch voltage of the primary and secondary power stages is constrained by the input and output voltages, the suggested design does not require any snubber circuits to alleviate the voltage stress of the switching

devices. In addition, the efficiency of power conversion in both directions is identical [55, 54].

In comparison to classic DAB and DBSRC, CLLC resonant converters use frequency modulation that makes control more difficult. Moreover, the CLLC network needs more resonant components that increases size and cost. On the other hand, DAB and DBSRC use phase shift modulation that does not require a complex control [54].

Symmetric LLC resonant converter

During the high voltage input, the classic resonant topologies listed above have numerous drawbacks. The high circulating energy and considerable switching loss that occur with the high voltage input are their principal drawbacks. Symmetric LLC resonant converter [39] is shown in Figure 1.7.

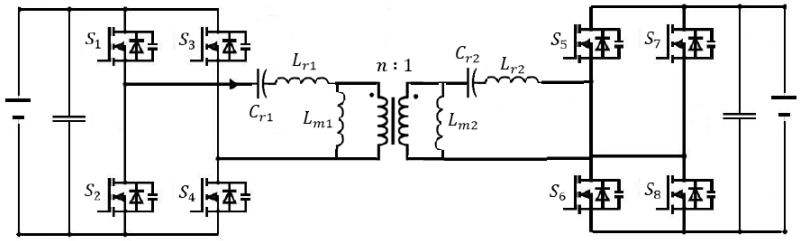

Figure 1.7 – Symmetric LLC converter

This converter offers a limited switching frequency range with light load and ZVS capability with no load, compared to the aforementioned standard resonant converters [39]. For both forward and reverse modes, the bidirectional symmetric LLC resonant converter demonstrates a high efficiency [39].

1.2.3 General comparison

Starting with the DAB converter and by comparing it with the other bidirectional DC-DC topologies already seen in the last sections, a comparative study which elaborate the advantages and the limitations for each topology has been conducted.
The DAB converter presented in Figure 1.1 has the following advantages: ZVS capability, adjustable voltage gain and control easy. But with wide voltage variation, the DAB converter suffers from: Loss of ZVS (require active clamping and more elements), higher turn-off loss, higher circulating current (conduction loss) and decreasing in Soft-switching range under light load.
The DBSRC is presented in Figure 1.3. Due to the nature of resonance, it is possible to accomplish ZVS for switches at the primary-side and ZCS for switches at secondary-side. But high dimensions of the resonant tank (additional capacitor) and additional costs are presented. At high input voltage, there is a possibility of losing the soft switching property. The problem of soft switching with light load still exist.

The asymmetric LLC converter (Figure 1.4) has the possibility of ZVS on the primary side and ZCS on the secondary and it can be operate at wide input voltage range comparing with the last topologies. On the other hand, because of the resonant-tank is not symmetric, there is a difference of the gain equation and the efficiency between the two operating modes (forward and reverse). Furthermore, while the DC-DC LLC converter is predicted to have a high efficiency in both operating modes, some of the unidirectional originator's intrinsic advantages are being lost (reduced ZVS zone in the reverse mode resulting in lower efficiency) and large switching losses occur at high output voltages.
With the asymmetric CLLC converter (Figure 1.5), for a wide range of voltage gain, inverter switches have the capability to operate with ZVS and rectifier switches have the possibility to operate with ZCS in the two operating modes which the bidirectional property can be achieved unlike the asymmetric LLC converter. But, in terms of design and cost, it has additional two capacitors and one inductor, and the bidirectional transition speed is slow.
Moreover, the symmetric CLLC converter (or DBSRC with symmetric resonant tank) presented in Figure 1.6 has the following advantages: ZVS capability for inverter switches as well as soft commutation capability for rectifier switches. Whereas, the drawbacks of this topology are: Additional two capacitors and one inductor and a high switching frequency is required.
Finally, the symmetric LLC converter (Figure 1.7) is proposed as a performed bidirectional DC-DC topology. Comparatively to others convertres, it has a wide ZVS, which leads to the switching losses reduction. This topology has less circulating energy and less switching/conduction losses during the high input voltage than the others. Solving the problems at light load (narrow switching frequency range at light load) is possible. Finally, it has a high efficiency in both charging and discharging modes. However, the disadvantages can be summarized by: Additional capacitors and inductors, more complex design procedure (design the resonant tank for the two modes and for the two sides) and more complex control.

1.2.4 Summary

Starting from the history of the DC-DC converters, by discovering many topologies for the isolated bidirectional DC-DC converters, it was clear that each topology has the owner characteristics and the related limitations. A comparison table that summarizes the comparative study between the different topologies is illustrated in Figure 1.8.

DC-DC topology	Design simplicity	ZVS range	Number of passive components	Cost/size	Efficiency	EMI	Control simplicity
DAB	★★★★★	★★	★	★	★★	★	★★★★
DBSRC	★★★★	★★★	★★	★★	★★★	★★	★★★★
Asymmetric LLC	★★★	★★★	★★★	★★★	★★★	★★★	★★★
Asymmetric CLLC	★★	★★★★	★★★★	★★★★	★★★★	★★★★	★★
Symmetric CLLC	★★	★★★★	★★★★	★★★★	★★★★	★★★★	★★
Symmetric LLC	★	★★★★★	★★★★★	★★★★★	★★★★★	★★★★★	★

★ : Lowest ★★★★★ : Highest

Figure 1.8 – Comparison table of DC-DC topologies

Thus, based on the requirements and desired performance for the implementation of the bidirectional DC-DC topology, a tradeoff between, on the one hand, the design and control complexity, cost and size, and on the other hand, the ZVS range and efficiency should be taken into account.

1.3 Modulation strategies

1.3.1 Pulse Frequency Modulation (PFM)

PFM strategy [56] consists of varying switching frequency of MOSFETs control signals where the full bridge's power MOSFETs are regulated in complementary mode at duty 50%. Variations in the signal are represented by changes in the frequency of the pulses, as shown in Figure 1.9.

Figure 1.9 – PFM scheme

It should be noted that PFM strategy is one of most frequently adopted modulation strategies for DC-DC resonant converters.

1.3.2 Pulse Width Modulation (PWM)

The PWM approach [57] employs a rectangular pulse wave with a variable pulse width, as shown in Figure 1.10, resulting in a variation in the waveform's average value.

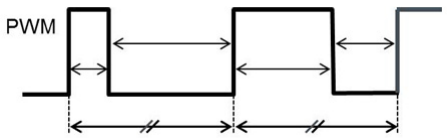

Figure 1.10 – PWM scheme

The intersective approach, which just requires a sawtooth or triangle waveform (easily made with a simple oscillator) and a comparator, is the simplest way to generate a PWM signal. The PWM signal is in the high state when the value of the reference signal is greater than the modulation waveform, and it is in the low state otherwise. The key idea behind the PWM technique is that the duty cycle can change the square wave input voltage of the resonant circuit.

1.3.3 Phase Shift Modulation (PSM)

The PSM technique [58] is a method of modifying the phase shift angle between two signals with a constant signal frequency. The converter is controlled by varying the phase shift between the MOSFETs control signals, with fixed switching frequency and fixed duty cycle. As shown in Figure 1.11, the phase shift angle between left and right arms in the identical H-bridge (MOSFET S6 and MOSFET S7 respectively) in Figure 1.4 is defined as controlled phase shift angle θ, where the duty cycle is fixed at 0.5 for all MOSFETs and with fixed switching period T.

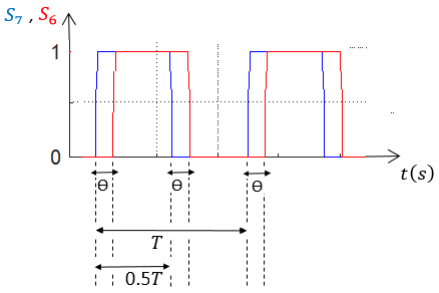

Figure 1.11 – MOSFETs signals in PSM strategy

1.4 DC-DC LLC resonant converter study

1.4.1 Modelling techniques of DC-DC LLC converter

Establishing a representative dynamic model of the LLC resonant converter presented in Figure 4.4 is necessary in order to create an appropriate control method.

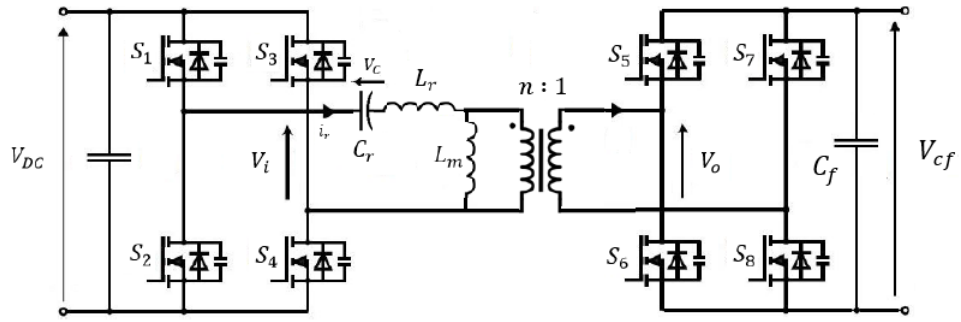

Figure 1.12 – DC-DC LLC resonant converter structure

To build small signal models in PWM converters, the state space average approach is commonly used in modelling methodologies. However, because the operating frequency is not constant and the energy is largely conveyed through the fundamental components of the voltage and current waveforms, it is not appropriate to a frequency-controlled resonant converter [43].
LLC resonant converters contain the resonant circuit that consists of series resonant inductor, capacitor and a parallel magnetic inductor. On the other hand, the LLC resonant converter is a nonlinear system due to the presence of switching frequency harmonics, nonlinear coupling between AC and DC model variables, and the LLC resonant circuit. There are two modelling approaches: Large signal modelling and Small signal modelling.

Large signal modelling

The large signal model can be split into three parts [39]: write the non-linear dynamic state equations, use variables' harmonic approximation and apply the Extended Describing Function (EDF) [40, 41, 42] for non linear terms approximation.
The LLC converter resonant tank receives a square wave voltage created by the full-bridge. The equivalent circuit, in the forward mode, is shown in Figure 1.13. The output capacitor's parasitic resistor is ignored [59].

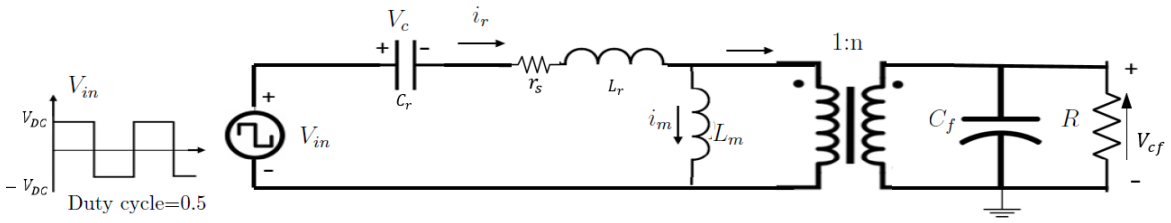

Figure 1.13 – Equivalent circuit of the LLC resonant converter in the forward mode

Based on the LLC equivalent circuit in Figure 1.13, the non-linear dynamic equations [42, 59, 40] are defined, by applying the Kirchhoff's laws, as in Equations (1.1), (1.2), (1.3) and (1.4):

$$\frac{di_r}{dt} = \frac{1}{L_r}V_{in} - \frac{r_s}{L_r}i_r - \frac{1}{L_r}V_c - \frac{n}{L_r}sign(i_r - i_m)V_{cf} \tag{1.1}$$

$$\frac{dV_c}{dt} = \frac{1}{C_r} i_r \tag{1.2}$$

$$\frac{di_m}{dt} = \frac{n}{L_m} V_{cf} sign(i_r - i_m) \tag{1.3}$$

$$C_f \frac{dV_{cf}}{dt} = n|i_r - i_m| - \frac{1}{R} V_{cf} \tag{1.4}$$

where V_{in} is a square wave voltage produced by the full bridge switches and applied to the resonant tank in the forward mode, and i_r, V_c, i_m, and V_{cf} are state variables.
The three AC state variables i_r, V_c, and i_m are decomposed into sine and cosine components, and the derivatives are equal to zero to yield the steady-state values, using the sinusoidal approximation. On the other hand, this decomposition provides two states for each AC variable, resulting in a seventh-order dynamic model. The approximation for the series resonant current and its derivative can be presented as follows in Equations (1.5) and (1.6) respectively [42, 59, 40].

$$i_r(t) = i_{rs}(t)\sin(w_s t) - i_{rc}(t)\cos(w_s t) \tag{1.5}$$

$$\frac{di_r}{dt} = (\frac{di_{rs}}{dt} + w_s i_{rc})\sin(w_s t) - (\frac{di_{rc}}{dt} - w_s i_{rs})\cos(w_s t) \tag{1.6}$$

Beside this harmonic approximation, and in order to approximate the nonlinear terms in the dynamic equations, the Extending Describing Function (EDF) [42] is used. The EDF concept is a strong mathematical tool for modelling and studying the dynamic behavior of resonant converters. By breaking modulated waveforms into sine and cosine waveforms, this method combines time domain and frequency domain analysis to derive the model. The fundamental harmonic terms can be used to approximate the nonlinear terms. The nonlinear terms could be expressed as presented in Equations (1.7), (1.8) and (1.9) [42, 59, 40].

$$V_{in}(t) = F_1(d, V_{in})\sin(w_s t) \tag{1.7}$$

$$sign(i_r - i_m) = F_2(i_s, i_p)\sin(w_s t) - F_3(i_c, i_p)\cos(w_s t) \tag{1.8}$$

$$|i_r| = F_4(i_s, i_c) \tag{1.9}$$

where the EDF parameters are F1 (d, V_{in}), F2 (i_s, i_p, v_{cf}), F3 (i_s, i_p, v_{cf}), and F4 (i_s, i_c).
$i_p = \sqrt{(i_{rs} - i_{ms})^2 + (i_{rc} - i_{mc})^2}$, where $i_s = i_{rs} - i_{ms}$ and $i_c = i_{rc} - i_{mc}$ are the sine and cosine components of the secondary current $(i_r - i_m)$ respectively, and d is the duty cycle which is fixed at 50%.

The EDF parameters are defined as in Equations (1.10), (1.11), (1.12) and (1.13).

$$F_1(d, V_{in}) = \frac{4V_{DC}}{\pi} \sin \pi d = \frac{4V_{DC}}{\pi} \tag{1.10}$$

$$F_2(i_s, i_p) = \frac{4}{\pi} \frac{i_s}{i_p} \tag{1.11}$$

$$F_3(i_c, i_p) = \frac{4}{\pi} \frac{i_c}{i_p} \tag{1.12}$$

$$F_4(i_s, i_c) = \frac{2}{\pi} i_p \tag{1.13}$$

By making use of EDF terms and the harmonic approximations, splitting the sine and cosine terms, the following Equations (1.14), (1.15), (1.16), (1.17), (1.18), (1.19) and (1.20) are obtained [42, 59, 40].

$$\frac{di_{rs}}{dt} = \frac{4V_{DC}}{\pi L_r} - w_s i_{rc} - \frac{r_s i_{rs}}{L_r} - \frac{V_{cs}}{L_r} - \frac{4n\,(i_{rs} - i_{ms})\,V_{cf}}{\pi\, L_r\, i_p} \tag{1.14}$$

$$\frac{di_{rc}}{dt} = w_s i_{rs} - \frac{r_s i_{rc}}{L_r} - \frac{V_{cc}}{L_r} - \frac{4n\,(i_{rc} - i_{mc})\,V_{cf}}{\pi\, L_r\, i_p} \tag{1.15}$$

$$\frac{dV_{cs}}{dt} = -w_s V_{cc} + \frac{i_{rs}}{C_r} \tag{1.16}$$

$$\frac{dV_{cc}}{dt} = w_s V_{cs} + \frac{i_{rc}}{C_r} \tag{1.17}$$

$$\frac{di_{ms}}{dt} = -w_s i_{mc} + \frac{4n\,(i_{rs} - i_{ms})\,V_{cf}}{\pi\, L_m\, i_p} \tag{1.18}$$

$$\frac{di_{mc}}{dt} = w_s i_{ms} + \frac{4n\,(i_{rc} - i_{mc})\,V_{cf}}{\pi\, L_m\, i_p} \tag{1.19}$$

$$\frac{dV_{cf}}{dt} = \frac{2n\, i_p}{\pi\, C_f} - \frac{nV_{cf}}{R\, C_f} \tag{1.20}$$

These equations represent the large-signal dynamic model of the DC-DC LLC converter in the forward mode.

When a large signal transient disruption occurs, this model guarantee enough dynamic information for the DC-DC LLC converter. However, this model is used with the PFM strategy that needs wide switching frequencies to cover the entire operating zone. A wide switching frequency causes the DC-DC LLC converter saturation, prevents to achieve a good control performance and reduce the efficiency. For this reason, this model will be rewritten, in chapter 3, combined with the PSM strategy that can avoid the PFM limita-

tions. Furthermore, the proposed model based on PSM strategy allows us to design and apply non-linear robust controllers, such as the ASTC presented in chapter 3, in order to ensure the control robustness against the disturbances.

Small signal modelling

The LLC resonant converter's control-to-output transfer function represents the ratio of the output voltage V_o to small signal fluctuations in the switching frequency f_s. Modelling the LLC resonant converter's small signal characteristics is particularly difficult because common averaging techniques, such as state space models, are not applicable [60]. For the LLC resonant converter, a unique model of the small signal characteristics of the control-to-output transfer will be presented. The functioning and analysis of the converter can be explained using analogies to Frequency Modulation (FM) and Amplitude Modulation (AM) as shown in Figure 1.14 [60].

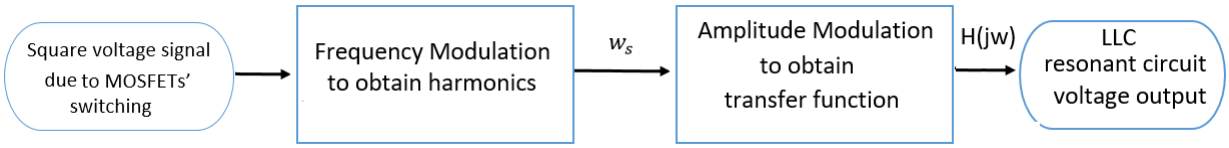

Figure 1.14 – Small signal model concept

FM is used to obtain the switching frequency and harmonics, whereas the role of AM is to generate the transfer function of the LLC voltage gain.
A frequency modulated square wave signal is presented mathematically as in Equations (1.21) [60].

$$V_{in}(t) = \sum_{n=1,3,5,\ldots}^{\infty} \frac{4V_{DC}}{n\pi} \sin\left(n2\pi f_s t\right) \tag{1.21}$$

where $V_{in}(t)$ represents the input square voltage of the LLC resonant tank from the DC bus side (Figure 4.4), and f_s is the switching frequency ($w_s = 2\pi f_s$).
A more accurate picture of the true dynamics of the converter can be noticed by including the third and fifth harmonics in the model, as shown in Equation (1.22).

$$\begin{aligned} V_{in}(t) = & \frac{4V_{DC}}{\pi} \sin\left(w_s t\right) \\ & + \frac{4V_{DC}}{3\pi} \sin\left(3w_s t\right) \\ & + \frac{4V_{DC}}{5\pi} \sin\left(5w_s t\right) \end{aligned} \tag{1.22}$$

Assuming that the voltage signal can be only represented by the fundamental component in order to simplify the model design, the equivalent circuit model is presented in Figure 1.15 [60]:

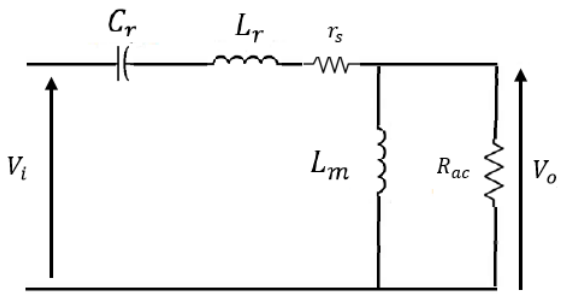

Figure 1.15 – Equivalent small signal LLC circuit in the forward mode

Based on this figure, the gain transfer function of the DC-DC LLC converter H can be obtained as in Equation (1.23).

$$H(s) = \frac{V_o}{V_i} = \frac{R_{ac}.L_m.C_r.s^2}{L_m.L_r.C_r.s^3 + (R_{ac}.C_r.(L_m + L_r) + L_m C_r r_s).s^2 + (L_m + r_s C_r R_{ac}).s + R_{ac}} \tag{1.23}$$

The higher order harmonics make a major contribution to the total transfer function, and it is necessary to include them to represent the full dynamics of the control-to-output transfer function. However, including the third and fifth harmonics makes the model and control design more complex.
It should be noted that the small signal model concept applied to the DC-DC LLC converter in the forward mode (i.e. G2V mode), presented in this section, will be used in chapter 2 to represent the DC-DC LLC converter in the reverse mode (i.e. V2X mode). The aim is to generate the transfer function in the case of each modulation strategy (PFM, PWM and PSM) applied to the DC-DC LLC converter. The obtained transfer functions allow us, as detailed in chapter 2, to design and apply linear controllers such as the GI based on the PI controller.

1.4.2 Control of DC-DC LLC converter

Due to the intended soft-switching properties, the LLC resonant topology is chosen for the high power applications. In order to ensure good performance of the DC-DC LLC converter, it is necessary to define a control strategy based on an improved LLC dynamic model and able to reach all the operating points. To build small signal model in power converters, the state space average approach is commonly used. However, because the operating frequency is not constant and the energy is largely conveyed through the fundamental components of the current and voltage signals, it is not appropriate to a frequency-controlled resonant converter. The voltage transfer functions are obtained using the First Harmonic Approximation (FHA) [61, 24]. An averaged LLC converter model is illustrated by ignoring the effect of the LLC resonant circuit dynamics. Small signal modelling [62, 63] enables for the creation of a LLC transfer function based on an averaged mode, making control simple [64]. However, it fails to account for non-linear and uncertain

effects, such as the DC-DC LLC converter structure, which impacts the robustness of the control law in the face of system perturbations and results in a reduced operating zone. For the DC-DC LLC converter, models based on the Extending Describing Function (EDF) have been presented [42, 40]. When an unexpected disturbance arises, these models give adequate LLC converter dynamic information. With these models, it is possible to create a mathematical model that describes the dynamics of the DC-DC LLC converter's variables. The model is still nonlinear and complex, making the control law design difficult.

Many control laws, such as PID controller and sliding mode control, have been proposed in the literature for the DC-DC LLC converter based on large or small signal models. In [43], a simple PI controller is used to regulate the resonant current flowing in the LLC resonant circuit by varying the phase shift. In [65], a combined sliding mode-PI control strategy is implemented to reduce the chattering phenomenon. By adjusting the DC bus voltage, a PI controller is implemented to ensure the battery voltage regulation in [66]. In [40, 67], sliding mode control is used to insure the battery voltage stability by varying the switching frequency and the duty cycle respectively.

PFM is generally adopted with the DC-DC LLC resonant converter by varying the switching frequency of the MOSFETs' control signals [68, 69]. ZVS is required to provide good performances and high efficiency for the entire operating zone [70]. The switching frequency feasible zone is established as a range between a minimum and maximum permissible value in order to ensure the ZVS [18, 24]. This feasibility constraint creates a cost-cutting challenge in the EV charger in terms of the software implementation and hardware design. However, by using the PFM strategy, the DC-DC LLC converter has limitations to operate in ZVS for a wide voltage and power variation ranges. There is a significant constraint imposed in front of the control stability over the whole operating zone. These constraints are obviously imposed on the OnBoard charger. As a result, the LLC resonant converters lose their soft switching characteristics, lowering efficiency and restricting bidirectional power transmission possibilities with the PFM strategy for a wide operating zone. PSM strategy [71, 72] is proposed to get around this constraint. With a fixed switching frequency, the PSM strategy is proposed to expand the DC-DC LLC converter's feasibility zone with an efficiency improvement [73, 74, 75]. In order to obtain the greatest ZVS performance across a wide range of output voltage and load, a two-phase interleaved LLC converter with a simple PWM control and fixed switching frequency is presented in [72]. In [74], a controlled duty-cycle-switching frequency modulation approach is studied for a wide voltage range of the DC-DC LLC converter that provides ZVS and output voltage control while improving efficiency under light loading conditions. The best combination of the duty cycle and switching frequency is chosen to provide both ZVS operating and output voltage control. [75] proposes a three-variable modulation approach, allowing the LLC resonant converter to operate with a wider voltage gain range. Soft switching is achieved by frequency control. The phase-shift control is provided to control the power transfer while keeping the output voltage constant. Fur-

thermore, calculating the duty cycle depending on load conditions aids in the elimination of reverse power flow. For high efficiency conversion, an integrated DAB–LLC DC-DC converter is studied in [76] with the DC-DC LLC converter carrying the majority of the power. At high input voltage, the DAB converter provides output voltage regulation by applying controlled phase shift between the LLC bridge and the DAB bridge, while at low input voltage, the variable LLC gain ensures voltage distribution regulation between converters.
[75] examined a dual phase LLC resonant converter for wide input voltage range applications with phase shift modulation. In order to control power transfer and keep the output voltage constant while the input voltage fluctuated, phase shift control was used. A 1.5 kW prototype of the suggested converter and modulation system with 210–400–V input and 80–V output is constructed and tested.
For PV applications, [77] developed a dual input single resonant tank LLC converter. The authors implemented independent maximum power point tracking (MPPT) for each panel using a phase shift PWM control. A 500W prototype with an output voltage regulated at 220 V dc and an input voltage range of 25V to 50V was created to show the effectiveness of the control technique.
A fixed frequency phase shift modulated LLC resonant converter was proposed in [23]. A phase shift was added between the square waves, with frequencies that are always tuned to the resonant frequency, to control the output voltage. The 1kW prototype that has been proposed is made to change 390 V input to 100–420 V output.
To provide good tracking accuracy with relatively reduced energy consumption, a control technique based on sliding mode control and linear state feedback is proposed in [78]. Moreover, the adaptive control is proposed in the literature [79] to regulate the voltage of power converters with unknown power load.

Stability analysis is critical to LLC converters. In [80] and [81], the envelope model of the DC-DC LLC converter is used to show the theoretical behavior of the DC-DC LLC converter stability using the resonant current control loop and the output voltage control respectively. Nyquist analysis has been used to examine the converter loop gains. Moreover, during a significant disturbance, the stability of the DC-DC LLC converter is investigated in [82], and a trigger control strategy is presented to ensure converter stability by expanding the LLC operating zone. Via the trigger control, the switching frequency is imposed to the peak frequency by monitoring the polarity of the resonant currents, which prevents the converter from the capacitive operating zone. In [83], a simple equivalent LLC circuit model based on a simplified EDF approach is proposed. A third-order equivalent model is generated. The frequency dynamics can be accurately predicted using the equivalent model. To properly build the feedback control, analytical study for all transfer functions has been given.

To summarize, existing control solutions for the DC-DC LLC converter are related to battery voltage or current control in the forward mode (G2V mode). In most cases, the

battery voltage varies over a reduced range (12-200 V) and the converter operates at a narrow power zone (500-2000 W). Furthermore, the existing control laws in the literature, combined with the different modulation strategies, are based on the popular PI controller. Compared to what existing in the literature, the proposed control strategies for the DC-DC LLC converter in this thesis aim to ensure the DC bus voltage control for a bidirectional EV charger application in both G2V and V2X modes. The battery voltage is constant and imposed by the BMS where it varies between 250 and 430 V, and the power varies between 0 and 11 kW. A linear controller with the GI method, combined to PFM, PWM and PSM in V2X mode, is developed in chapter 2 based on a small signal model. In fact, the tunning of the PI controller was found complex in order to provide a tradeoff fastness/stability. The advantages of the GI include a faster response as well as trajectory tracking in order to avoid an imortant current transformer which may cause a transformer saturation.
On the other hand, the linear controllers, such as the PI and GI, require the knoweldge of the DC-DC LLC model and are sensible to unexpected disturbances. Therefore, non-linear control laws, such as MFC and ASTC, are proposed in chapter 3 in order to ensure the control robustness against the disturbances with unkown boundaries. A stability proof of the internal LLC dynamics with the PSM strategy, that is not yet examined, is also given in chapter 3 based on an improved LLC model.

1.4.3 Optimized design of DC-DC LLC converter

Several research studies have been elaborated to optimally design the DC-DC LLC resonant converter. In [84], an optimal design methodology for the LLC resonant converter in battery charging applications is studied based on Time-Weighted Average Efficiency (TWAE). The TWAE index presents the average weight of conversion efficiency, which covers power losses of major components, during the battery charging period and it is proposed as the objective function to optimize the converter parameters. The optimization variables are the three resonant parameters: L_r, C_r, and L_m. Each of them is bound by physical constraints. The resonant frequency is often set between the minimum and maximum frequency to achieve ZVS. The optimization algorithm is based on calculating the current, voltage, and frequency of the converter under typical charging conditions. An important TWAE is achieved. Moreover, instead of minimizing the components stresses, a proper choice of the converter parameters resulting in an improved MOSFETS control operation has been performed in [85]. The power MOSFETS drain-sources have been derived to realize the ZVS operation. Soft switching is achieved for all power devices under all operating conditions. The optimized design is achieved for different regulated output voltages (35–165 V) under different loads (0–3 A) and input voltages (320–370 V). In [11], a power converter with a multi-operating mode is proposed. The topology can work as a bidirectional DC-DC converter. The controller is implemented based on a state-

space averaging model. A weight decrease in the power converter in the electric vehicle is obtained. A double-boost DC-DC converter for electric vehicles is designed in [86]. A feedforward double closed-loop control is proposed based on the small-signal model. The proposed converter showed an improved efficiency compared to other topologies. In [87], an optimal algorithm is applied to a three-port multidirectional DC-DC converter to increase efficiency and reduce energy costs using a droop control method. A novel multilevel DC-DC converter is proposed in [88] to enhance the performances of traditional multilevel DC-DC converters using an impedance source that reduces the number of sub-modules and improves the system efficiency. [89] presents an adjustable robust optimization to improve the performances of the microgrid system by increasing the absorption ratio of renewable energy in G2V and V2G modes of EV. In [90], an optimization methodology is designed to obtain optimal scheduling of smart charging of EVs considering the requirements, such as time specifications as is the case. An optimal design of a multi-resonant converter for interfacing electrolyser stack to DC voltage source is studied in [91]. The design improves ZVS but not throughout the whole operating range. Isolated single input, dual output DC-DC converters for EVs is studied in [92]. The proposed control strategy consists of regulating two different output voltages by varying the duty cycle and switching frequency to improve the converter efficiency. Furthermore, [16, 93] show an optimal design methodology under the worst operation condition (minimum input voltage with maximum output power or maximum input voltage with minimum output power). Some constraints are included to obtain the suitable design area, such as operation mode, voltage stress for resonant capacitor, ZVS operation for primary switches, and resonant tank root-mean-square current. The main drawback related to this methodology is based on the fact that the DC-DC LLC converter is designed to operate in the above resonant frequency region, thus the control instability issue under light load operation may occur due to the circuit parasitics. [94, 95, 96] highlight an optimized transformer design for LLC converter to reduce core volume and conduction losses in the transformer windings for high power density. In addition to that, it provides the necessary isolation and required voltage-conversion and magnetizing inductance for efficient converter operation. It also makes a significant contribution to the weight and size of the overall converter. In [97], computer-aided design optimization is proposed to design LLC converters to optimize the converter efficiency. A mode solver technique is proposed to handle LLC converter steady-state solutions. The mode solver utilizes numerical non-linear programming techniques to solve LLC-state equations and determine operation mode. The objective function is the calculated efficiency. The fmincon function of MATLAB optimization toolbox is applied as the optimizer to solve this non-linear, constrained, and continuous optimization problem. In [98, 99], an optimized design of parameters of the main circuit of the LLC resonant converter is proposed to reach the maximum controllability characteristics. A selection of compromise between conduction losses, switching losses and regulation range with stable ZVS condition is considered. The optimization model is developed based on

the First Harmonic Approximation (FHA) analysis.
However, the proposed optimization strategies in the literature are mostly intended to minimize the cost and weight of the DC-DC LLC converter and guarantee soft-switching property in one operation mode, i.e. G2V mode [84, 85, 93, 97, 98, 99]. Moreover, the DC-DC LLC converter is designed based on a reduced battery voltage (12–48 V) [16, 93, 97, 98, 99, 94, 95, 96] and converter power (20–1000 W) [85, 16, 93, 97, 98, 99, 94, 95, 96]. To the best of our knowledge, an optimization algorithm, which takes into consideration the DC-DC LLC converter behavior in the two operation modes G2V and V2G for a bidirectional charger application, is not yet considered in the literature.
In chapter 2, an optimization strategy is proposed to minimize the DC-DC LLC converter cost and improve the control frequency feasibility zone, for a wide variation of the battery voltage (240–430 V) and converter power (0–11 kW), in G2V and V2G modes simultaneously. An optimal design that considers the G2V and V2G control stability equations in the optimization algorithm is elaborated.

1.5 Electric vehicle charger control

Electric vehicle (EV) charging technology is becoming more important. The EV On-Board Charger (OBC) consists of an AC-DC converter followed by a DC-DC converter. The well known mode is Grid-to-Vehicle (G2V) mode which represents the battery charging mode. The batteries are charged from the power grid through OnBoard or OffBoard chargers. However, due to the capacity of the EVs to store energy, using bidirectional battery chargers, it is possible to send energy in the opposite way, i.e. from the EV batteries to the power grid. This operation mode is identified as Vehicle-to-Grid (V2G). The V2G operation mode can also be used to stabilize the power grid and to support large-scale renewable energy integration [100].
Based on the defined topology of AC-DC and DC-DC converters, the control strategies make it possible to ensure the system stability (battery voltage or DC bus voltage, grid current,...) while respecting specifications (speed, precision, efficiency). As presented in Figure 1.16, there is a control strategy for each converter in order to generate the gate pulses.

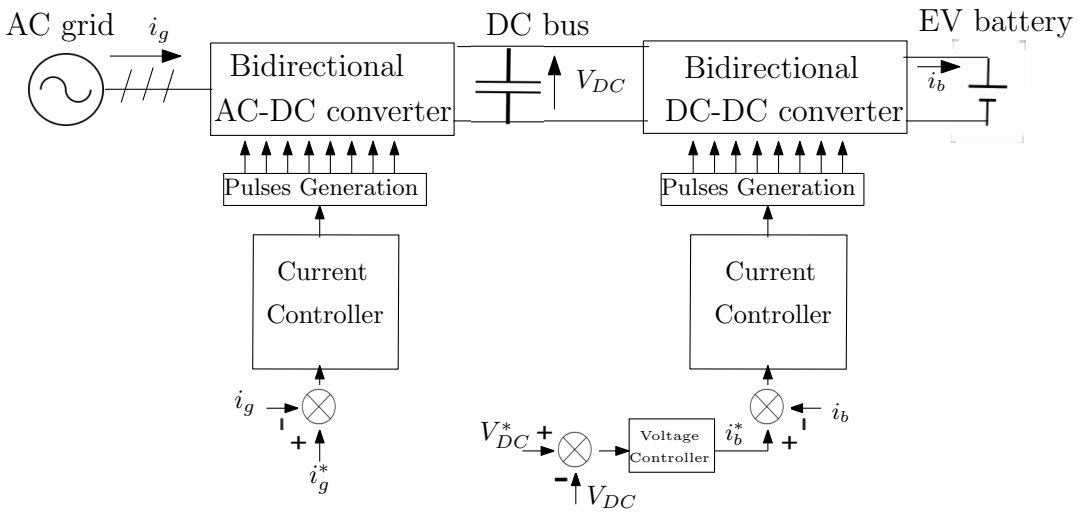

Figure 1.16 – AC-DC and DC-DC converters' control in a bidirectional EV charger

The bidirectional charger must be able to return energy to the grid while respecting control performance, and charge an EV's battery pack with the fewest possible harmonic currents. In order to choose which two topologies (AC-DC and DC-DC converters) to combine to create a bidirectional charger, [101] has been covered some of the power electronic topologies of bidirectional AC-DC and DC-DC converters that meet these requirements.

In [102], a unique Eight-Switch Inverter (ESI) can transmit electrical energy between the DC-link (attached to the battery) and the electric traction system as a DC-AC inverter and operate as a bidirectional single-phase AC-DC battery charger with V2G mode. Additionally, as presented in Figure 1.16, a bidirectional-interleaved DC-DC converter with a dual-loop controller is elaborated to be used to connect the ESI to a low-voltage battery in order to reduce battery current ripple and improve the DC system efficiency with a smaller inductor size. To further reduce the THD of the input current in charging/V2G modes, an enhanced AC-DC controller based on Proportional-Resonant Control (PRC) is presented.

The thesis [103] focuses on the combination of two power electronic converters found in the EV configuration: the OBC and the 400V/14V DC-DC converter that connects the high and low voltage batteries. A three-port parallel resonant topology that supports ZVS has been created. The converter ensures galvanic isolation while enabling high efficiency in conversion modes with a bidirectional power flow between the energy sources and OBC. In the second part of the work, the characteristics of the DC-DC converter are studied in order to optimize the control and operating strategy.

Due to its simplicity, a three-phase two-level Voltage Source Inverter (VSI) is the recommended topology for battery charging systems. It is typically attached to a DC-DC converter stage. The thesis [104] suggests an alternative two-stage architecture based on a three-phase unfolding inverter (unfolder) to reduce size and weight compared to the typical two-stage converter. In order to directly connect each DC-DC stage output with its associated phase, the unfolder operates at line frequency. The line-frequency oper-

ating produces very little switching loss and very few current harmonics in the unfolder but cannot control the line currents. Instead, the high-frequency DC-DC stage control them. A robust rotating-frame controller is proposed by the combination of a feedforward controller and an integral output feedback controller tuned using linear quadratic regulator.

A single stage PV based EV charger connected to the grid is presented in [105]. The bidirectional power flow is supported by this charger. The AC-DC converter is used to compensate the reactive power (Figure 1.16). The charging station's control is based on the reference active and reactive power commands.

The purpose of [106] is to offer an accurate bidirectional charging control method for plug-in hybrid electric vehicles by taking into account the State of Charge (SoC) of the batteries and to ensure voltage and frequency regulation. According to the available power, the proposed technique can simultaneously control the grid's voltage and frequency during the charging period as well as the charge of linked batteries.

For a hybrid electric vehicle that uses a fuel cell as its primary energy source and a supercapacitor and battery as backup power sources, a double integral sliding mode controller has been proposed in [107]. An LCC-S compensation network-based wireless charging system has been elaborated to charge energy storage devices. Lyapunov stability theory has confirmed the stability of the suggested control structure.

Battery life and charging time may be impacted by the input current of an EV charger with important total harmonic distortion (THD) and output voltage ripple distortion. [108] details a universal EV charger's whole design process, with a focus on the control algorithm. In order to ensure efficient battery charging, a novel control method based on the combination of Voltage-Oriented Control (VOC) and Sinusoidal Pulse-Width Modulation (SPWM) approach is developed.

Compared to the literature, a bidirectional EV charger including an AC-DC Vienna topology connected to two DC-DC LLC converters is studied in chapter 4. Control strategies, that aim to ensure the DC bus voltage and grid current control, are applied to the charger for the whole operating zone in both G2V and V2G modes. On the other hand, a single phase EV charger including the DAB converter topology is studied in chapter 5. The DAB converter is used to ensure the DC bus voltage and grid current control.

1.6 Conclusion

Starting from the history of DC-DC converters, a study of many topologies of bidirectional isolated DC-DC converters has been firstly generated in this chapter. The characteristics and limitations related to each topology have been presented. A comparative study between these topologies in terms of some essential parameters, such as converter efficiency, design complexity, control complexity, input/output voltage range and soft switching (ZVS or ZCS) range, has been studied. It is confirmed that, based on the

requirements, a tradeoff between the design complexity and cost, and the desired performance should be taken into account.
Furthermore, the modulation strategies for DC-DC converters, such as PFM, PWM and PSM, have been presented. It should be noted that in chapter 2, these modulation strategies are applied to the DC-DC LLC converter. A comparative study between them is highlighted in terms of performance and efficiency.
Resonant converters are widely used for high density and high power applications, such as EV charger which requires a high efficiency. The bidirectional DC-DC LLC resonant converter has been studied. In order to implement control strategies, two modelling approaches of LLC converter such as large and small signal modelling have been presented. The principle of each modelling process has been defined. The advantages and drawbacks have been highlighted. These modelling approaches are applied in the forward mode, whereas our proposed approaches are designed in the reverse mode. In chapter 2, a small signal model associated to each modulation strategy is investigated. In addition, the large signal model, proposed in the literature with the PFM strategy, will be rewritten in chapter 3 combined with the PSM strategy in order to design non-linear robust controllers.
Several control strategies, proposed in the literature for the LLC resonant converter, have been presented. The drawbacks of the PFM strategy push to implementt fixed switching frequency strategies, such as PWM and PSM. Existing control solutions are related to battery voltage or current control in the forward mode and based on the popular PI controller. Compared to the literature, this thesis aims to ensure the DC bus voltage control with a wide battery voltage and power variations. In chapter 2, a linear control algorithm, based on the GI method, is proposed in the reverse mode to ensure a fast and stable response compared to the PI controller. On the other hand, the linear controllers, such as the PI and GI, are less robust against unexpected disturbances. Therefore, non-linear control laws, such as MFC and ASTC, are proposed in chapter 3 in order to ensure the control robustness against the disturbances with unkown boundaries.
Moreover, many optimization strategies have been proposed in the literature in order to optimally design the LLC structure and improve its performance. In chapter 2, an optimization strategy considering the G2V and V2G control equations, which is not yet considered in the literature, is proposed to minimize the DC-DC LLC converter cost and improve the control frequency feasibility zone, for a bidirectional EV charger application.
Further, many research studies focus on the EV charger control in the literature. Usually, the studied EV charger consists of two stages: AC-DC and DC-DC converters. The AC-DC converter is usually used to ensure the grid current stability, while the role of the DC-DC converter controller is to guarantee the battery charging/discharging. In this thesis, two different bidirectional charger topologies, motivated by an industrial collaboration, are presented. In chapter 4, a bidirectional EV charger, divided into an AC-DC Vienna topology and two DC-DC LLC converters, is studied. On the other hand, a single phase EV charger including the DAB converter topology is studied in chapter 5. In

terms of control, the aim compared to the literature, with the two charger topologies, is to guarantee the DC bus voltage and grid current control for the entire operating zone in both G2V and V2G modes.

2

Modulation Strategies and Optimized Design of LLC converter

2.1 Introduction

The most frequently adopted modulation strategy for DC-DC LLC resonant converter is Pulse Frequency Modulation (PFM). However, for a wide input/output voltage range in V2X mode, PFM strategy requires a wide operating switching frequency range to meet the system voltage gain requirement. Wide switching frequency ranges cause soft switching operation losses, resulting in a low conversion efficiency. To improve the DC-DC LLC converter efficiency, the new challenge is twofold.

On the one hand, achieving improvements consists of a DC bus voltage control for the DC-DC LLC converter with fixed switching frequency strategies. In the literature, the small signal model is applied for the DC-DC LLC converter in G2V mode. The aim of this chapter is to provide a small signal model of the DC-DC LLC converter in V2X mode in order to generate the transfer function in the case of each modulation strategy (PFM, PWM and PSM).

To the best of our knowledge, existing control solutions for this type of converter are mostly related to battery voltage or current control and based on the PI controller over narrow volatge and power ranges. The goal of this chapter is to ensure the DC bus voltage control for a bidirectional EV charger application. The battery voltage is constant and imposed by the BMS where it varies between 250 and 430 V, and the power varies between 0 and 11 kW. A Gain Inversion (GI) method, combined to PFM, PWM and PSM, is developed to provide a fast and stable DC bus voltage response, and avoid the transformer saturation.

The results of this part are presented in our paper [20], and patents [25] and [26]. The key points of this part can be summarized as follows:

- Small signal DC-DC LLC dynamic model design with First Harmonic Approximation (FHA) in V2X mode;
- Design and implementation of three modulation strategies: PFM, PWM and PSM based on FHA;
- Design of control laws based on the DC-DC LLC transfer function Gain Inversion (GI);
- Highlight on the benefits and limitations of PFM, PWM and PSM;
- Comparison between the different modulation strategies in terms of control performance and efficiency at V2X mode;

On the other hand, a solution in terms of the hardware optimization is proposed. The proposed optimization strategies of the DC-DC LLC converter in the literature are mostly intended in one operation mode, i.e. G2V mode, based on narrow voltage and power ranges. To the best of our knowledge, an optimization algorithm, which takes into consideration the DC-DC LLC converter behavior in the two operation modes G2V and V2G for a bidirectional charger application, is not yet considered in the literature.
The main contribution is to design an optimization strategy, including the G2V and V2X control equations, to minimize the DC-DC LLC converter cost and to improve the control performance and the EV charger efficiency for a wide variation of the battery voltage (240–430 V) and converter power (0–11 kW) in both G2V and V2X modes. The aim is to increase the control frequency feasibilty zone. The control constraints are based on the control strategy studied in the first section of this chapter (and presented in our paper [20]), where PFM, based on a GI method, is implemented to regulate the DC bus voltage. The results of this part are presented in our journal paper [21]. The main contributions can be summarized as follows:

- Optimized design of DC-DC LLC converter dimensions;
- EV charger cost and sizing minimization;
- Important improvement of the control frequency feasibility zone for V2X mode;
- Total reduction in the control frequency saturation zone for G2V mode;
- Improvement of the control performance and converter efficiency for a bidirectional EV charger application with a wide battery voltage and power variation;

2.2 Modulation strategies design based on gain inversion

The full-bridge DC-DC LLC resonant converter's configuration is shown in Figure 2.1.

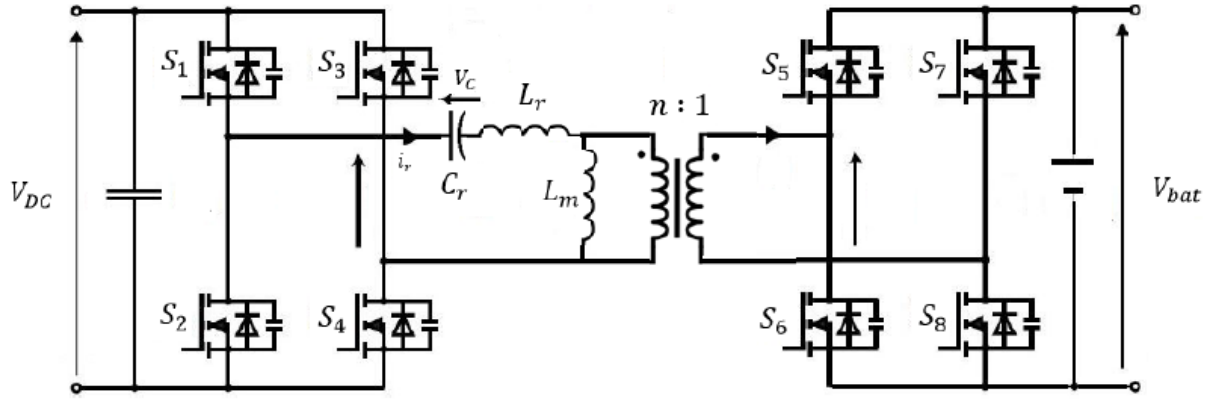

Figure 2.1 – DC-DC LLC resonant converter

Figure 2.1 includes the DC bus capacitor, switching network, resonant circuit, and battery model. Switches S_1-S_8 with anti-parallel diodes and snubber capacitors make up the switching network. A resonant inductor L_r, a magnetizing inductor L_m, and a resonant capacitor C_r make up the resonant tank. The high frequency transformer with turns ratios of n ensures the galvanic isolation. The battery model is represented by the constant DC voltage source. It should be noted that there is an output filter circuit, which is not represented in Figure 2.1, before the battery model that aims to reduce the battery current ripple. The voltage V_{DC} is the DC bus voltage which represents the output voltage of the AC-DC stage of the EV charger, while V_{bat} is the battery voltage and P is the converter power.

2.2.1 Pulse Frequency Modulation

Small-signal modeling based on First Harmonic Approximation (FHA) methodology [24] is used to examine the dynamics of the DC-DC LLC converter. The FHA is based on the following assumptions:

- The input voltage is modelled as an ideal sinusoidal voltage source, which represents only the fundamental component ignoring all the higher-order harmonics;
- The output filter capacitor, the leakage inductance of the transformer and the MOSFETs' effect are ignored.

Pulse Frequency Modulation (PFM) strategy consists of varying the switching frequency of MOSFETs' control signals, where the power MOSFETs of the full bridge are controlled in complementary at duty 0.5.

G2V mode

For G2V mode, the power MOSFETs of the full-bridge in the primary side (S1-4) of the transformer are controlled in complementary at duty 0.5 ignoring the dead-time, whereas the diodes of the full -bridge in the secondary side are used for rectification. The

equivalent model of the DC-DC LLC resonant converter (Figure 2.1), using small-signal modeling with FHA, can be obtained as shown in Figure 2.2 [24, 109].

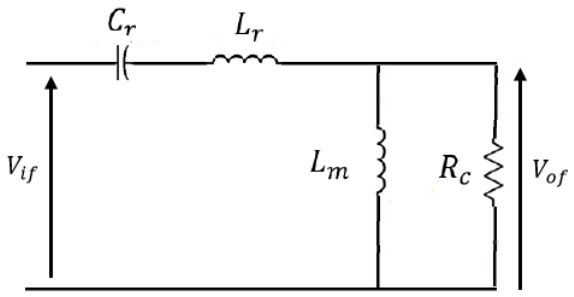

Figure 2.2 – FHA equivalent model of DC-DC LLC converter in G2V mode.

The equivalent resistance R_c is given, based on FHA [24], by Equation (2.1):

$$R_c = n^2 \frac{8}{\pi^2} \frac{V_{bat}^2}{P} \tag{2.1}$$

The input voltage waveform of the resonant tank in Figure 2.1 can be expressed in Fourier series, whose fundamental component V_{if} has the following expression (2.2) [24]:

$$V_{if} = \frac{2\sqrt{2}}{\pi} V_{DC} \tag{2.2}$$

For the secondary side, the rectifier is driven by a square wave output voltage with a fundamental component V_{of} (2.3) [24]:

$$V_{of} = \frac{2\sqrt{2}}{\pi} n\, V_{bat} \tag{2.3}$$

Based on the equivalent model of the DC-DC LLC converter in G2V mode (Figure 2.2), the gain transfer function magnitude is given by Equation (2.4):

$$|G| = \frac{V_{of}}{V_{if}} = \frac{n.V_{bat}}{V_{DC}} = \frac{|-R_c\, L_m\, C_r\, w^2|}{|-L_m\, L_r\, C_r\, w^3\, j - (R_c\, C_r\, (L_m + L_r))\, w^2 + L_m\, w\, j + R_c|} \tag{2.4}$$

With $w = 2\pi f$, where f is the switching frequency.

The DC-DC LLC transfer function is represented by the DC bus voltage/battery voltage ratio. A switching frequency control of the H-bridge will adapt the gain of the DC-DC LLC converter and allows to regulate the DC bus voltage to a certain setpoint (450 V).

DC bus voltage regulation based on a GI method for DC-DC LLC with wide variations in both the battery voltage (240–430 V) and power (0–11 kW) is proposed in [109]. The H-bridge of the DC-DC LLC converter ensures a constant DC voltage at the DC bus by MOSFET signals regulation. The GI makes it possible to obtain an expression (feedforward) of the switching frequency which depends on the parameters of the resonant

circuit, the power request, the DC bus voltage and the battery voltage. The feedforward switching frequency f_{0c} is defined based on Equation (2.4), to ensure a DC bus voltage at the input of the DC-DC LLC converter, as a solution of the following Equation (2.5):

$$a\,w^6 + b\,w^4 + c\,w^2 + d = 0 \tag{2.5}$$

where the parameters a, b, c and d are expressed as follows:

$$a = {L_m}^2\,{L_r}^2\,{C_r}^2 \tag{2.6}$$

$$b = R_c^2\,C_r^2\,(L_r + L_m)^2 - 2\,L_m^2\,L_r\,C_r - R_c^2\,L_m^2\,C_r^2\,\frac{V_{DC}^2}{(n\,V_{bat})^2} \tag{2.7}$$

$$c = L_m^2 - 2\,R_c^2\,C_r\,(L_m + L_r) \tag{2.8}$$

$$d = R_c^2 \tag{2.9}$$

By taking $y = w^2$, Equation (2.5) can be transformed into the following cubic Equation (2.10):

$$a\,y^3 + b\,y^2 + c\,y + d = 0 \tag{2.10}$$

By solving Equation (2.10) using what is known as the Tschirnhaus–Vieta approach for cubic equations, the feedforward switching frequency f_{0c} can be obtained as follows in Equation (2.15):

$$p = \frac{3\,a\,c - b^2}{3\,a^2} \tag{2.11}$$

$$q = \frac{2\,b^3 - 9\,a\,b\,c + 27\,a^2\,d}{27\,a^3} \tag{2.12}$$

$$M = 2\sqrt{\frac{-p}{3}} \tag{2.13}$$

$$\phi = arccos(\frac{3\,q}{M\,p}) \tag{2.14}$$

$$f_{0c} = \frac{1}{2\pi}(\sqrt{M\,cos(\frac{\phi}{3}) - \frac{b}{3\,a}}) \tag{2.15}$$

In Figure 2.3, f_{0c} is presented according to the battery voltage and power variations.

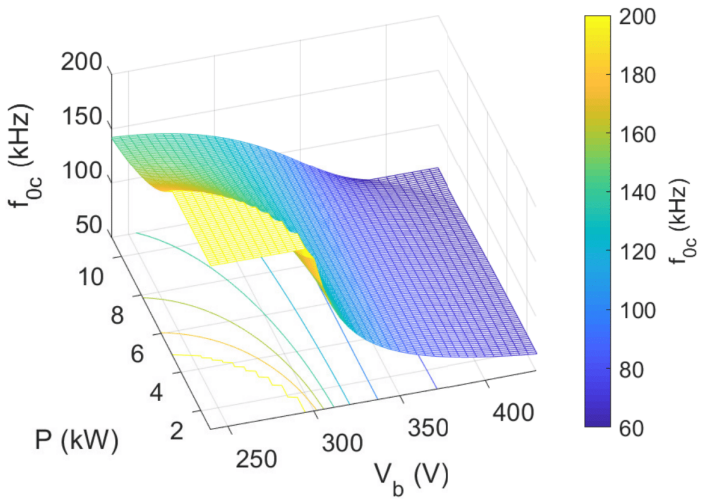

Figure 2.3 – Feedforward frequency in G2V mode according to battery voltage and power variation.

It should be noted that the switching frequency feasible zone is limited between the minimal authorized switching frequency f_{min}=60 kHz and the maximal authorized switching frequency f_{max}=200 kHz.
According to Figure 2.3, the yellow zone represents an operating zone where the control frequency is saturated at f_{max} (200 kHz). It is clearly seen that there is a small frequency saturation zone in G2V mode for low battery voltages and low powers, which corresponds to the yellow zone of the figure. The closed loop PFM control strategy is presented in Figure 2.4, where f is the controlled switching frequency.

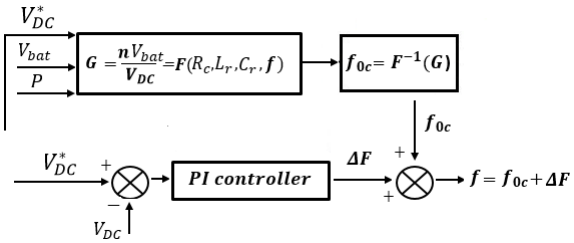

Figure 2.4 – PFM strategy closed loop control block in G2V mode

By calculating f_{0c} using the GI, its application is not sufficient to cancel the static error between the measured DC bus voltage and the setpoint due to the parametric dispersions and the simplifying assumptions (related to FHA and defined in the beginning of this section). A PI controller with an output Δf has been added to f_{0c} until the DC bus voltage static error tolerance becomes acceptable ($\leq$ +- ϵ).

V2X mode

The dynamics of the DC-DC LLC converter are investigated using the small-signal modeling technique based on FHA. For V2X mode, the power MOSFETs of the full-bridge in the secondary side of the transformer (S5-8) are controlled in complementary

at duty 0.5 ignoring the dead-time, whereas the diodes of the full -bridge in the primary side are used for rectification.

The input voltage waveform of the resonant tank, in Figure 2.1, can be expressed in V2X mode, as in Equation (2.16) [20]:

$$V_{if} = \frac{2\sqrt{2}}{\pi} n V_{bat} \tag{2.16}$$

The rectifier is driven by a square wave output voltage with a fundamental component V_{of} in Equation (2.17):

$$V_{of} = \frac{2\sqrt{2}}{\pi} V_{DC} \tag{2.17}$$

The equivalent model of the DC-DC LLC resonant converter (Figure 2.1) can be obtained, using small-signal modeling with FHA, as shown in Figure 2.5 [20].

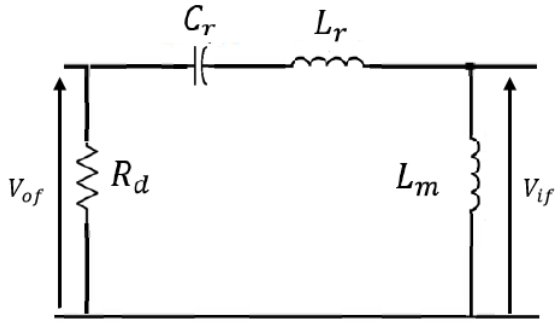

Figure 2.5 – FHA equivalent model of DC-DC LLC converter in V2X mode.

The equivalent resistance R_d is given, based on FHA [20], by Equation (2.18):

$$R_d = \frac{8}{\pi^2} \frac{V_{DC}^2}{P} \tag{2.18}$$

Based on the FHA equivalent model of the DC-DC LLC converter in V2X mode in Figure 2.5, the gain transfer function can be expressed as in Equation (2.19):

$$|G| = \frac{V_{of}}{V_{if}} = \frac{V_{DC}}{n V_{bat}} = \frac{|R_d.C_r\, wj|}{|1 - L_r C_r w^2 + R_d C_r wj|} \tag{2.19}$$

The feedforward switching frequency f_{0d}, resulting from the GI method, is defined based on Equation (2.19) as a solution of the following Equation (2.20):

$$A w^4 + B w^2 + 1 = 0 \tag{2.20}$$

where the parameters A and B are defined in Equations (2.21) and (2.22), respectively:

$$A = {L_r}^2 {C_r}^2 \tag{2.21}$$

$$B = R_d^2 C_r^2 - 2 L_r C_r - \frac{(n V_{bat})^2}{{V_{DC}}^2} {R_d}^2 C_r^2 \tag{2.22}$$

By taking $v = w^2$, Equation (2.20) can be transformed into the following Equation (2.23):

$$A\,v^2 + B\,v + 1 = 0 \tag{2.23}$$

By solving Equation (2.23), the feedforward switching frequency f_{0d} can be expressed as in Equation (2.24):

$$f_{0d} = \frac{1}{2\pi}\sqrt{\frac{-B + \sqrt{B^2 - 4\,A}}{2\,A}} \tag{2.24}$$

In Figure 2.6, f_{0d} is presented according to the battery voltage and power variation.

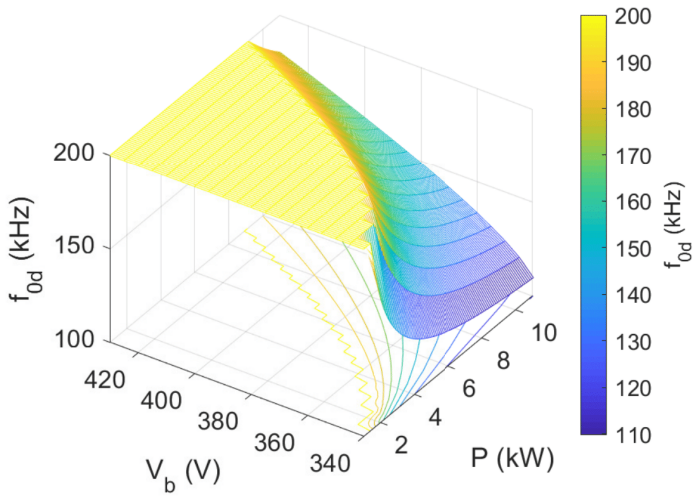

Figure 2.6 – Feedforward frequency in V2X mode according to battery voltage and power variation.

Based on Figure 2.6, there is an important yellow zone that corresponds to a switching frequency of 200 kHz due to the fact that the switching frequency is limited between 60 kHz and 200 kHz. Thus, it is clearly seen that the switching frequency saturation zone in V2X mode (yellow zone) is much higher than that in G2V mode (see Figure 2.3). This gives a low efficiency and low control performance with PFM strategy in the reversible operation mode of the EV charger. The closed loop PFM control strategy based on the GI in V2X mode is presented in Figure 2.7.

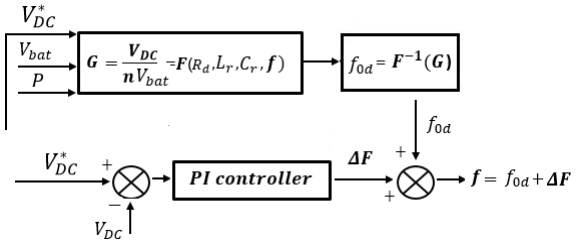

Figure 2.7 – PFM strategy closed loop control block in V2X mode

In Figures 2.8 and 2.9, an example with V_{bat}=350 V and P=9000 W is presented.

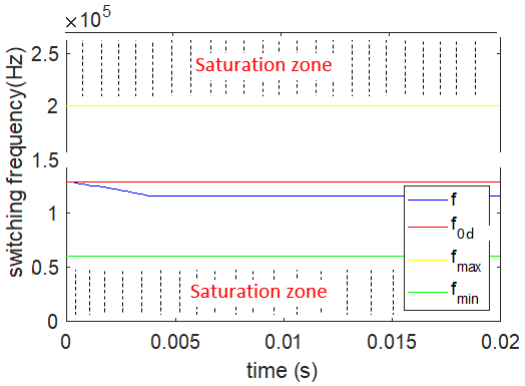

Figure 2.8 – Switching frequency with PFM for V_{bat}= 350 V and P= 9000 W

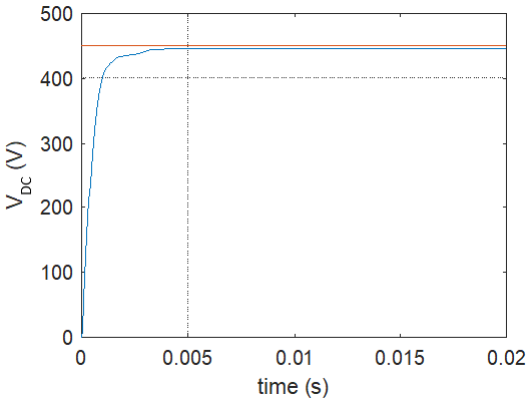

Figure 2.9 – DC bus voltage with PFM for V_{bat}= 350 V and P= 9000 W

The switching frequency f (Figure 2.8) decreases, due to the integral action of the controller, from its feedforward value (130 kHz) and reaches 118 kHz at steady state. As shown in Figure 2.9, it is clearly seen that, for this operating point, the DC bus voltage is regulated with an acceptable voltage tracking error (5 V).

In Figures 2.10 and 2.11, an example with V_{bat}=350 V and P=2000 W is shown. It should be noted that this operating point belongs to the saturation zone.

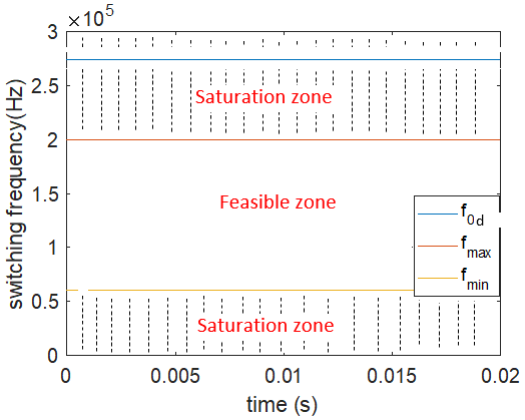

Figure 2.10 – Feedforward frequency with PFM for V_{bat}= 350 V and P= 2000 W

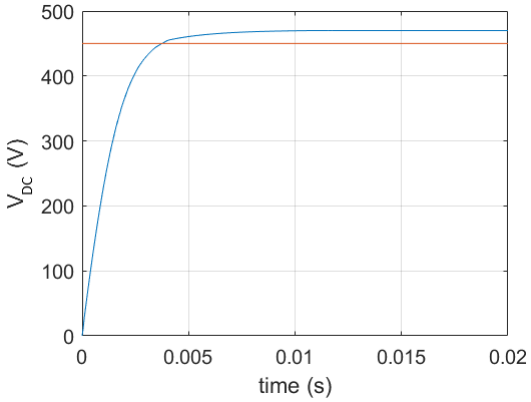

Figure 2.11 – DC bus voltage with PFM for V_{bat}= 350 V and P= 2000 W

From Figure 2.10, the feedforward frequency f_{0d} presents a value (275 kHz) out of the frequency feasible zone. To respect the frequency feasibility condition, the switching frequency f is saturated at 200 kHz, which causes an important DC bus voltage tracking error (20 V) as shown in Figure 2.11.

The control frequency range, depending essentially on the elements of the resonant tank i.e L_r, C_r and n, the power request P, the DC bus voltage V_{DC} and the battery voltage V_{bat}, is therefore not sufficient to reach all operating points.
In order to be able to regulate the DC bus voltage in the saturation zone, a modulation strategy with fixed switching frequency can be implemented. Outside of the saturation zone, PFM strategy can be used.

2.2.2 Pulse Width Modulation

The main concept of the Pulse Width Modulation (PWM) strategy is that the square wave input voltage of the resonant circuit can be varied by changing the duty cycle with fixed switching frequency. The resonant tank impedance, impacting the gain value (Equation (2.19)), is a function of the switching frequency. PWM strategy is implemented based on FHA. The switching frequency f is fixed and the DC bus voltage is regulated by the variable duty cycle D.
PWM presents the advantage to operate at lower switching frequencies than the switching frequencies of the conventional PFM control method.
The fundamental component of input voltage waveform of the resonant tank has the following expression that depends on D [67]:

$$V_{if} = \frac{\sqrt{2}}{\pi} n V_{bat} [1 - cos(2D\pi)] \tag{2.25}$$

The fundamental component of the square wave output voltage is:

$$V_{of} = \frac{2\sqrt{2}}{\pi} V_{DC} \tag{2.26}$$

The transmission gain of resonant tank for PWM mode G' is determined based on FHA [67] and given by:

$$|G'| = \frac{V_{DC}}{n\,V_{bat}} = \frac{1 - cos(2\pi D)}{2}\,|G| \tag{2.27}$$

where G is defined in Equation (2.19).

The voltage gain of the converter is regulated by varying the duty ratio instead of increasing the switching frequency. The closed loop PWM control law is designed as shown in Figure 2.12.

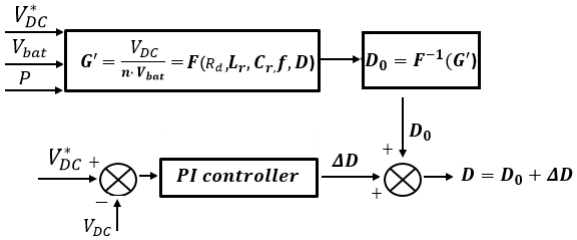

Figure 2.12 – PWM strategy closed loop control block in V2X mode

Based on PWM gain G' in Equation (2.27), the feedforward duty cycle D_0 is defined using the gain inversion with a fixed switching frequency f. Then, it is added to a PI output to cancel the static voltage error. The advantage of this control strategy based on gain inversion is that the duty cycle regulation of the DC-DC LLC converter doesn't have a wide bandwidth, which causes a gradual rise of the DC bus voltage at transient state.

An example with V_{bat}= 350 V and P= 2000 W and f= 200 kHz is presented. The controlled duty cycle D is shown in Figure 2.13 which starts to rise up until the DC bus voltage reaches the reference, when it reaches 0.385. Figure 2.14 shows that, at steady state, the DC bus voltage oscillates around the reference with an acceptable voltage tracking error (2 V).

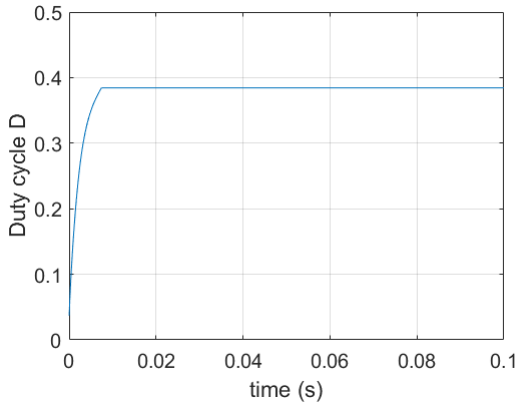

Figure 2.13 – Duty cycle with V_{bat}= 350 V and P= 2000 W

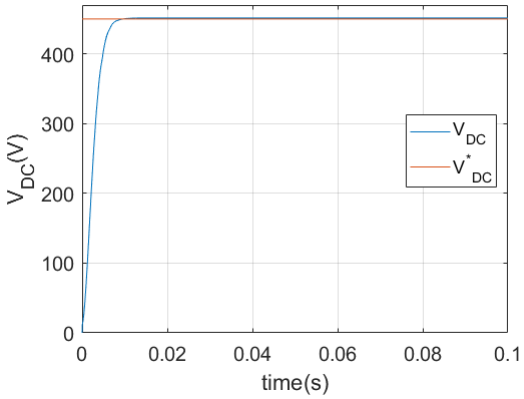

Figure 2.14 – DC bus voltage with PWM for V_{bat}= 350 V and P= 2000 W

On the other hand, the duty cycle variation should be limited to respect FHA and obtain proper resonant operation of the DC-DC LLC resonant converter. When the duty cycle variation is far from 0.5, FHA is no longer valid [67, 110]. ZVS property can also be lost in this case. However, an acceptable DC bus regulation error can be obtained involving significant corrective action by the PI controller. It should be noted that to guarantee ZVS operation with PWM strategy, the duty cycle must change around 0.5. Thus, when investigating ZVS operation for the whole operation points with PWM strategy, it is necessary to add higher order harmonic components to the fundamental component for a more precise analysis. The modelling study with more harmonics in the case of PWM strategy leads to a complex model to control.

2.2.3 Phase Shift Modulation

To overcome the drawbacks of the PFM strategy and avoid the limitations of the PWM strategy, the Phase Shift Modulation (PSM) strategy presented in our paper [20] is a highly efficient method for achieving the DC-DC LLC converter fixed operating frequency.
The DC-DC gain is adjusted by varying the phase shift between the MOSFETs' control signals, with both fixed switching frequency and duty cycle. The controlled phase shift affects the fundamental harmonic of the input voltage.
As shown in Figure 2.15, the phase shift angle between left (MOSFET S6 (inversely S5)) and right arms (MOSFET S7 (inversely S8)) in the identical H-bridge in Figure 2.1 is defined as the controlled phase shift angle θ, where the duty cycle is set to 0.5 for all MOSFETs.

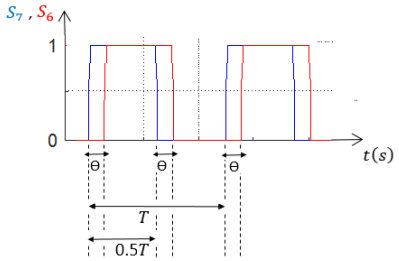

Figure 2.15 – Mosfets signals in PSM strategy

Based on small signal FHA modelling, by using Asynchronous Clamped Mode (ACM) [17, 71], the fundamental component of the input voltage waveform of the resonant tank has the following expression which depends on θ :

$$V_{if} = \frac{n\,V_{bat}}{\sqrt{2}\pi}\sqrt{[10 + 6cos(\theta\pi)]} \tag{2.28}$$

The fundamental value of the square wave resonant tank output voltage is:

$$V_{of} = \frac{2\sqrt{2}}{\pi}\,V_{DC} \tag{2.29}$$

The transmission gain of the resonant tank for the PSM strategy G" is given by:

$$|G"| = \frac{V_{DC}}{n\,V_{bat}} = \frac{\sqrt{(10 + 6cos(\theta\pi)}}{4}\,|G| \tag{2.30}$$

where G is defined in Equation (2.19) and the phase shift θ is varied between 0 and 0.5. The closed loop control law is designed in Figure 2.16.

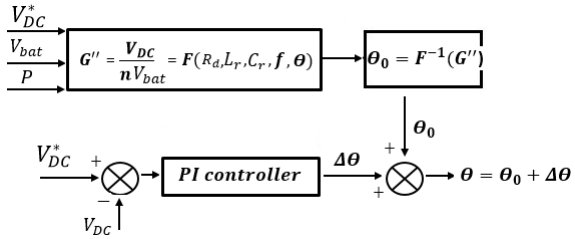

Figure 2.16 – PSM strategy closed loop control block in V2X mode

Based on the PSM gain G" in Equation (2.30), the feedforward phase shift angle θ_0 is defined by the GI. The phase shift θ_0 is added to the output of a PI controller in order to ensure the DC bus voltage control around a defined request V_{DC}^*.
The PSM strategy based on GI makes it possible to have a progressive rise in the DC bus voltage towards its reference with an acceptable overshoot percent tolerance without any soft start strategy implementation.
Figure 2.17 shows an example with V_{bat}= 350 V, P= 2000 W and f= 200 kHz. At steady state, the DC bus voltage oscillates around the reference within an acceptable voltage

error tolerance (5 V). The controlled phase shift angle is presented in Figure 2.18 which oscillates around 0.115 at steady state.

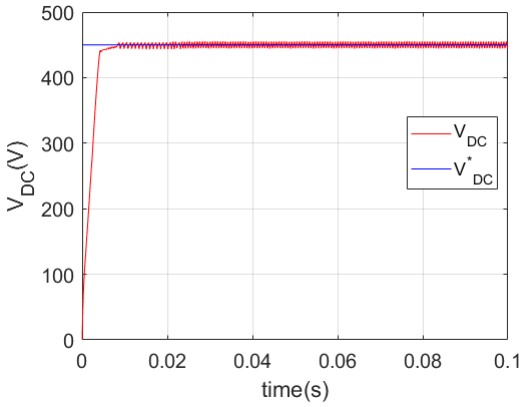

Figure 2.17 – DC bus voltage with PSM for V_{bat}= 350 V and P= 2000 W

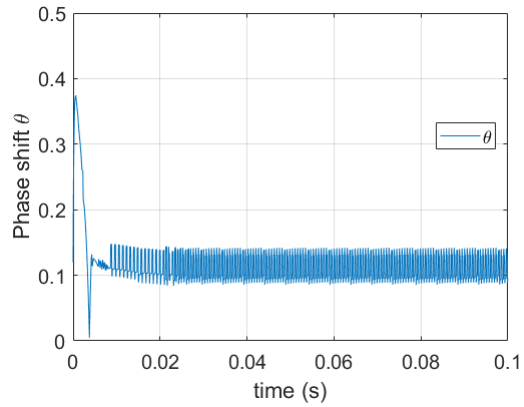

Figure 2.18 – Phase shift response with PSM for V_{bat}= 350 V and P= 2000 W

2.2.4 Modulation strategies comparison

Firstly, it should be noted that the work is done using MATLAB/SIMULINK (discrete solver). The parameter settings are shown in Table 2.1.

$C_f(\mu F)$	75	$K_p(PFM)$	40
$C_r(\eta F)$	80	$K_i(PFM)$	1
$L_r(\mu H)$	30	$K_p(PWM)$	0.00005
$L_m(\mu H)$	120	$K_i(PWM)$	0.00001
n	1.6	$K_p(PSM)$	0.005
$\epsilon(V)$	5	$K_i(PSM)$	0.0001

Table 2.1 – Table of LLC parameters and control gains

In this section, the different LLC modulation strategies: PFM, PWM and PSM, are compared in V2X mode in terms of control system performance (overshoot percent, rising

time and tracking error), and DC-DC LLC converter efficiency.
For V_{bat}= 350 V and P= 2000 W (operating point from the saturation zone), the DC bus voltage responses are compared for the different strategies in Figure 2.19.

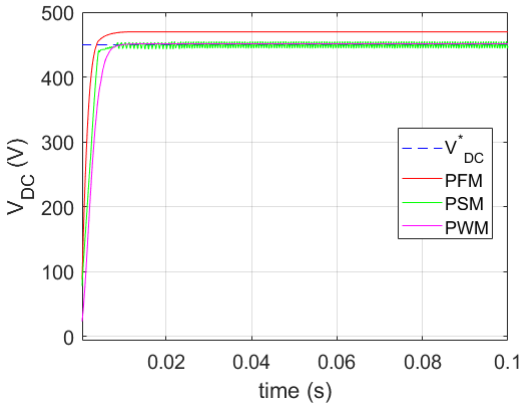

Figure 2.19 – DC bus voltage response comparison with V_{bat}= 350 V and P= 2000 W

The important voltage tracking error with the PFM strategy could be avoided when using PWM and PSM strategies, where DC bus voltage error has an acceptable tolerance around 5 V. In Figure 2.20, a comparison table based on the DC bus voltage responses is highlighted.

V_{bat}=350 V --- P=2000 W	PFM	PWM	PSM
Switching frequency f (kHz)	230 (f_0), f saturated at 200 kHz	200	200
Maximal voltage tracking error (V)	20	2	5
Settling time (s)	/*	0.009	0.006
Rising time (s)	/*	0.005	0.0035
Efficiency (%)	78.7	79	89

* : Important control tracking error

Figure 2.20 – Strategies comparison table with V_{bat}= 350 V and P= 2000 W

It is clearly seen that PSM strategy is faster than PWM strategy in terms of rising and settling times. Figures 2.21 and 2.22 show an efficiency comparison between PFM, PWM and PSM strategies accordinng to the power variation for some battery voltages.

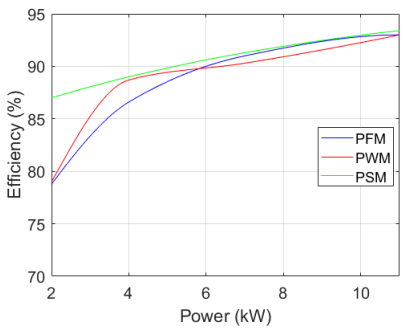

Figure 2.21 – Efficiency comparison with V_{bat}= 350 V

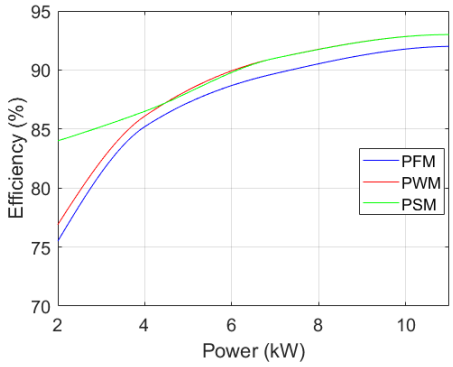

Figure 2.22 – Efficiency comparison with V_{bat}= 420 V

It should be noted that the efficiency is calculated by dividing the averaged output power (at DC bus side) by the averaged input power (at battery side) as expressed in Equation (2.31):

$$Efficiency = \frac{P_{DC}}{P_{bat}} = \frac{V_{DC}\, I_{DC}}{V_{bat}\, I_{bat}} \tag{2.31}$$

where I_{DC} is the mean value of the DC bus current, and I_{bat} is the mean value of the battery current.

At low powers, as shown in Figures 2.21 and 2.22, there is a high efficiency degradation with PFM strategy (high switching losses due to high switching frequency demand). It can clearly be seen that PWM strategy couldn't improve LLC efficiency at low powers load due to duty cycle variation out of ZVS condition related to FHA. PSM strategy, with fixed switching frequency and fixed duty cycle, has an improved efficiency, around 87% (With V_{bat}= 350 V in Figure 2.21) and 84% (With V_{bat}= 420 V in Figure 2.22) for P=2000 W, compared to the one of PFM and PWM strategies.

At high powers, with V_{bat}= 350 V in Figure 2.21, PFM strategy presents a high efficiency which is the case of operating points where the control frequency is non-saturated (outside of the yellow zone in Figure 2.6). In this zone, PFM strategy could be applied, whereas with V_{bat}= 420 V in Figure 2.22, PWM and PSM strategies have a better efficiency than PFM strategy which is the case of operating points in the saturation zone.

It is confirmed that PWM strategy has good control performance, but without efficiency improvement at low power loads because FHA model conditions are not satisfied. This result is coherent with the comparison table in Figure 2.20. Conversely to PWM strategy, PSM strategy, with fixed duty cycle 0.5, doesn't have a FHA constraint and can avoid PFM strategy drawbacks with good control performance and an improved converter efficiency for the whole operating zone.

As a summary, the PSM strategy based on the linear GI controller has been proposed in this section 2.2. This control strategy can be seen as a software solution in order to improve the charger performance and efficiency. Knowing that besides the software solution, a hardware solution can be also another way to improve not only the charger performance but also the charger cost and sizing. In the next section 2.3, an optimization

strategy is developed in order to optimally design the hardware of the DC-DC LLC converter for the bidirectional EV charger application.

2.3 Optimized design including control constraints

An OnBoard battery charger is constrained by sizing, weight, and cost. It should be also implemented either with unidirectional or bidirectional power flow. The dimensions of the DC-DC LLC converter are an essential part of the OnBoard charger sizing. The advantages of decreasing DC-DC LLC converter dimensions include reduced sizing, weight, and cost of the charger and improved reliability.

For DC-DC LLC resonant converters, the most frequently adopted modulation strategy is Pulse Frequency Modulation (PFM). The switching frequency feasible zone is defined between a minimum and maximum authorized value to guarantee Zero Voltage Switching (ZVS) condition. This frequency feasibility condition provides a cost minimization challenge related to both software and hardware implementations in the EV charger. However, when the PFM strategy is adopted for wide input/output range application in the onboard battery charger in V2X mode, a wide operating switching frequency range is required to meet the system voltage gain requirement. A wide switching frequency range causes soft switching operation loss, which results in low conversion efficiency and control performances.
The DC-DC LLC converter parameters, such as C_r, L_r, and L_m, directly affect the OnBoard charger performance. On one hand, they have an important effect on the control frequency feasibility for a wide operating zone. The feedforward switching frequency, in G2V and V2X modes, depends essentially on them. On the other hand, they affect the OnBoard charger sizing and cost.
The DC-DC LLC converter is controlled by varying the switching frequency with the PFM strategy based on a small signal modeling approach using the gain transfer function inversion method. The LLC parameters cause an important control frequency saturation zone, especially in V2X mode, where the switching frequency is out of the feasibility zone.

The new challenge is to design an optimization strategy to minimize the DC-DC LLC converter cost and improve the control frequency feasibility zone, for a wide variation of battery voltage and converter power, in the charging (G2V) and discharging (V2X) modes simultaneously. To the best of our knowledge, this optimization problem, in the case of a bidirectional (G2V and V2X) charger, is not yet considered in the literature. An optimized design that considers the control stability equations in the optimization algorithm is elaborated. The obtained results show a significant converter cost decrease and important expansion of control frequency feasibility zones. A comparative study between initial and optimized values, in G2V and V2X modes, is conducted according to the converter efficiency.

2.3.1 LLC parameters effect analysis

G2V mode

The equivalent LLC model based on small-signal modeling in Figure 2.2 shows that L_r, C_r, and L_m are the main parameters to define the resonant circuit sizing. Moreover, the LLC gain transfer function presented in Equation (2.4) depends on these parameters. Thus, any change in the value of any of them will affect the feedforward switching frequency f_{0c} defined in Equation (2.15). The effect of the variation of L_m, L_r, and C_r in f_{0c} is studied for G2V mode for some operating points with fixed DC bus voltage and transformer ratio.
It should be noted that L_{m0}, L_{r0}, and C_{r0} are the initial values of the DC-DC LLC converter.

- L_r effect:
  With $L_m = L_{m0}$, $C_r = C_{r0}$, $V_{bat} = 420$ V and by varying P ($P_{min} < P < P_{max}$), f_{0c} is presented in Figure 2.23 for different operating points according to the variation of L_r.

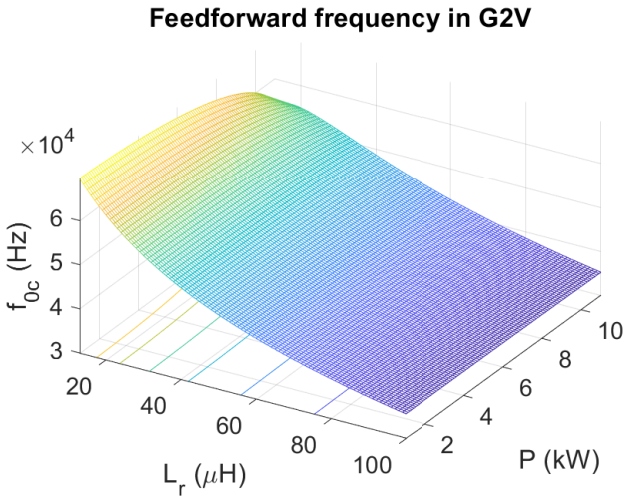

Figure 2.23 – G2V feedforward frequency in function of L_r.

It is clearly seen that f_{0c} increases with the decrease in L_r.

- C_r effect:
  With $L_m = L_{m0}$, $L_r = L_{r0}$, $V_{bat} = 420$ V and by varying P, f_{0c} is presented in Figure 2.24 for different operating points according to the variation of C_r.

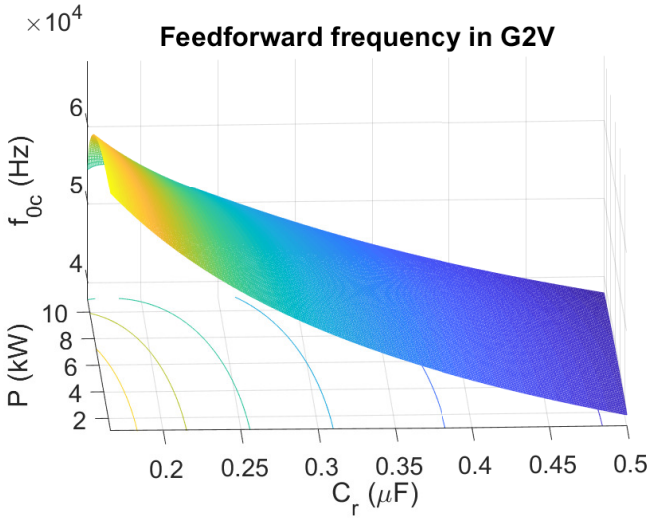

Figure 2.24 – G2V feedforward frequency in function of C_r.

It is confirmed that f_{0c} increases with the decrease in C_r too, but at a lower rate than in the case of L_r.

- L_m effect:
  With $L_r = L_{r0}$, $C_r = C_{r0}$, $V_{bat} = 420$ V and by varying P, f_{0c} is presented in Figure 2.25 for different operating points according to the variation of L_m.

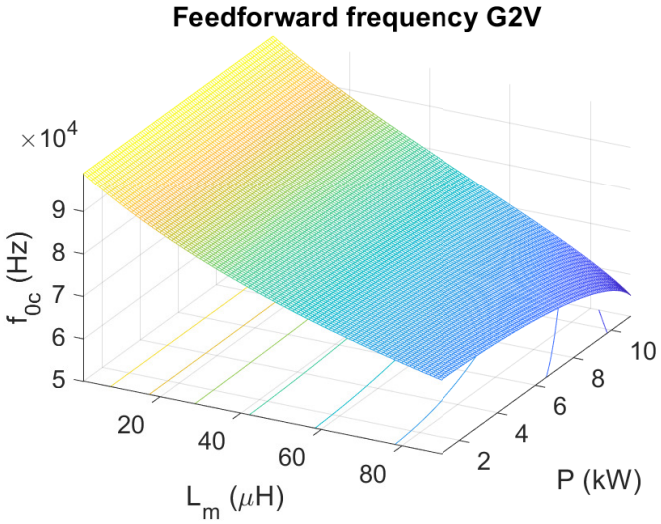

Figure 2.25 – G2V feedforward frequency in function of L_m.

It is clearly seen that f_{0c} increases with the decrease in L_m.

V2X mode

In V2X mode, the equivalent LLC model, presented in Figure 2.5, is based on the small-signal modeling with FHA. Thus, it should be noted that L_m does not affect the feedforward switching frequency f_{0d} in Equation (2.24) obtained from Equation (2.19).

The effect of the variation of L_r and C_r in f_{0d} is studied for V2X mode for some operating points with fixed DC bus voltage and transformer ratio.

- L_r effect:
  With $C_r = C_{r0}$, $V_{bat} = 420$ V and by varying P, f_{0d} is presented in Figure 2.26 for different operating points according to the variation of L_r.

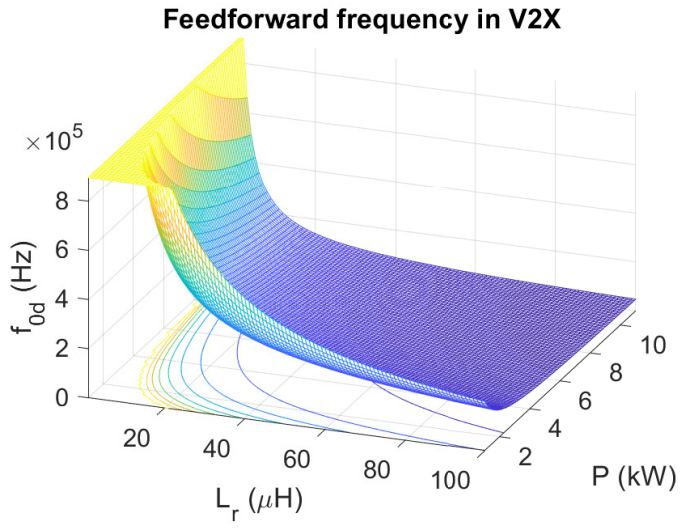

Figure 2.26 – V2X feedforward frequency in function of L_r.

It is clearly seen that f_{0d} increases with the decrease in L_r.

- C_r effect:
  With $L_r = L_{r0}$, $V_{bat} = 420$ V and by varying P, f_{0d} is presented in Figure 2.27 for different operating points according to the variation of C_r.

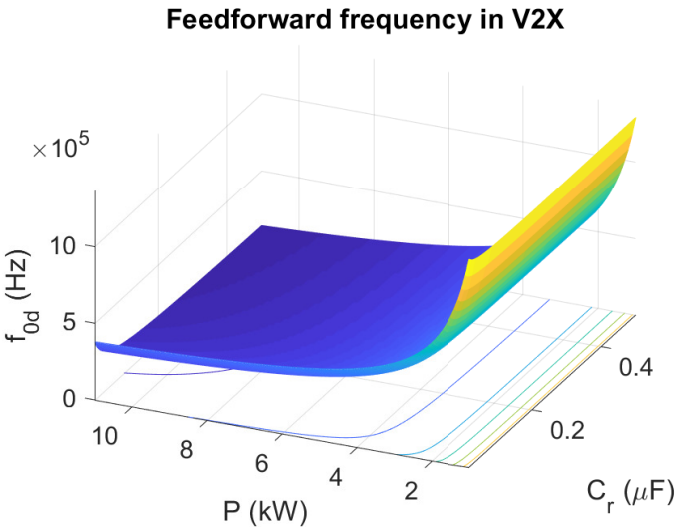

Figure 2.27 – V2X feedforward frequency in function of C_r.

It is confirmed that f_{0d} increases with the decrease in C_r too.

Summary

Table 2.2 summarizes the effect of the decrease in the LLC parameters, L_r, C_r, and L_m, on the feedforward frequencies f_{0c} and f_{0d}.

LLC Parameters	$\boldsymbol{f_{0c}}$	$\boldsymbol{f_{0d}}$
L_r	Increase	High increase
C_r	Increase	Very low increase
L_m	Increase	None

Table 2.2 – Effect of LLC parameters decrease on feedforward switching frequencies.

Based on this study of the LLC parameters effect on the feedforward switching frequency in G2V and V2X modes, it is confirmed that f_{0c} and f_{0d} are inversely proportional to L_r, C_r, and L_m. f_{0c} and f_{0d} should respect ZVS condition and not exceed the minimum and maximum authorized frequencies. Thus, there is a balance between cost and sizing minimization and control performances improvement. In the next section, an optimal algorithm design will be a new challenge to reach the target points.

2.3.2 Optimization strategy design

The aim of the optimization is to find the optimum L_r, C_r, and L_m that minimize the cost and sizing of the charger and improve the control frequency feasibility in G2V and V2X modes simultaneously.

The optimization problem can be expressed by 5 decision variables as presented in Equation (2.32):

$$X = \begin{bmatrix} L_r & C_r & L_m & f_{0c} & f_{0d} \end{bmatrix} = \begin{bmatrix} X(1) & X(2) & X(3) & X(4) & X(5) \end{bmatrix} \tag{2.32}$$

f_{0c} is the feedforward switching frequency in G2V mode defined in Equation (2.15).
f_{0d} is the feedforward switching frequency in V2X mode defined in Equation (2.24).

To obtain an optimization problem according to the battery voltage and power variation, the decision vector becomes:

$$X_{ij} = \begin{bmatrix} X(1)_{ij} & X(2)_{ij} & X(3)_{ij} & X(4)_{ij} & X(5)_{ij} \end{bmatrix} \tag{2.33}$$

where the indexes i and j represent the battery voltage and the converter power vectors, respectively, with:

$$V_{min} \leq V_{bat}(i) \leq V_{max}$$

$$P_{min} \leq P(j) \leq P_{max}$$

The optimal design of the resonant circuit should guarantee control stability in both G2V and V2X modes. In other words, the optimal values of L_r, C_r, and L_m should improve the feedforward switching frequency zone, based on PFM strategy with the gain inversion method, to reduce the saturation zones presented in Figures 2.3 and 2.6. Control stability constraints based on the gain inversion should be added to the optimization problem. The feedforward switching frequencies f_{0c} and f_{0d}, calculated using the optimal LLC parameters resulting from the optimization algorithm, are the solutions of Equations (2.5) and (2.20) in G2V and V2X modes, respectively. Therefore, the optimization strategy should not only minimize the DC-DC LLC converter sizing and cost by minimizing the LLC parameters L_r, C_r, and L_m but also generate an improved feedforward switching frequency zones in G2V and V2X modes according to the battery voltage and converter power variation.

To obtain the optimization target points, the objective function can be formulated as expressed in Equation (2.34):

$$F(X) = \alpha_1 X(1) + \alpha_2 X(2) + \alpha_3 X(3) + C_{G2V}(X) + C_{V2X}(X) \tag{2.34}$$

where α_1 and α_3 represent the costs euro/H of the resonant and magnetizing inductors L_r and L_m, respectively, and α_2 represent s the cost euro/F of the resonant capacitor C_r.

$C_{G2V}(X)$ and $C_{V2X}(X)$ are the equations that define the control stability in G2V and V2X modes, respectively. They are based on Equations (2.5) (for G2V mode) and (2.20) (for V2X mode) that allow us to obtain the feedforward switching frequencies for the whole operating zone. They can be expressed, in Equations (2.35) and (2.36), respectively, as follows:

$$C_{G2V}(X) = a(X)\,(2\pi\,X(4))^6 + b(X)\,(2\pi\,X(4))^4 + c(X)\,(2\pi\,X(4))^2 + d \tag{2.35}$$

where a, b, c, and d are defined in Equations (2.6–2.9), respectively, in function of the LLC parameters $X(1)$ (or L_r), $X(2)$ (or C_r) and $X(3)$ (or L_m).

$$C_{V2X}(X) = A(X)\,(2\pi\,X(5))^4 + B(X)\,(2\pi\,X(5))^2 + 1 \tag{2.36}$$

where A and B are defined in Equations (2.21) and (2.22), respectively, in function of $X(1)$ and $X(2)$.

The optimization problem includes linear and non-linear constraints resulting from hardware conditions and control requirements. The constraints of the variation of L_r, C_r and L_m, related to the hardware design limitations, are expressed in Equations (2.37–2.39):

$$\frac{L_{r0}}{10} \leq X(1) \leq L_{r0} \tag{2.37}$$

$$\frac{C_{r0}}{10} \leq X(2) \leq C_{r0} \tag{2.38}$$

$$\frac{L_{m0}}{10} \leq X(3) \leq L_{m0} \tag{2.39}$$

To guarantee ZVS property, the switching frequency, in each of G2V and V2X modes, should respect the following constraints formulated in Equations (2.40) and (2.41), respectively:

$$f_{min} \leq X(4) \leq f_{max} \tag{2.40}$$

$$f_{min} \leq X(5) \leq f_{max} \tag{2.41}$$

where f_{min} and f_{max} are the minimum and maximum authorized switching frequencies, respectively.

There are also some constraints that should be defined, to obtain more accurate feedforward switching frequencies, i.e., solutions of the control stability equations, as follows in Equations (2.42) and (2.43):

$$a(X)\,(2\pi\,X(4))^6 + b(X)\,(2\pi\,X(4))^4 + c(X)\,(2\pi\,X(4))^2 + d \geq 0 \tag{2.42}$$

$$A(X)\,(2\pi\,X(5))^4 + B(X)\,(2\pi\,X(5))^2 + 1 \geq 0 \tag{2.43}$$

As a result of this optimization algorithm, the global minimum vector X_{ij} (Equation (2.33)) for each operating point (battery voltage $V_{bat}(i)$ and converter power $P(j)$) can be obtained. To obtain the optimal values of the DC-DC LLC converter parameters for the whole operating zone, the mean value of the global minimums of each LLC parameter is calculated as follows:

$$L_{r1} = \frac{\sum_{i=1}^{p}\sum_{j=1}^{q} X(1)_{ij}}{p \times q} \tag{2.44}$$

$$C_{r1} = \frac{\sum_{i=1}^{p}\sum_{j=1}^{q} X(2)_{ij}}{p \times q} \tag{2.45}$$

$$L_{m1} = \frac{\sum_{i=1}^{p}\sum_{j=1}^{q} X(3)_{ij}}{p \times q} \tag{2.46}$$

L_{r1}, C_{r1}, and L_{m1} are the mean values of global minimums of L_r, C_r, and L_m, respectively. Based on the mean values L_{r1}, C_{r1} and L_{m1}, the feedforward switching frequencies f_{0c} and f_{0d} can be obtained using Equations (2.15) and (2.24) for the whole operating zone (battery voltage and converter power variation). The optimization algorithm can be summarized using the flow chart presented in Figure 2.28.

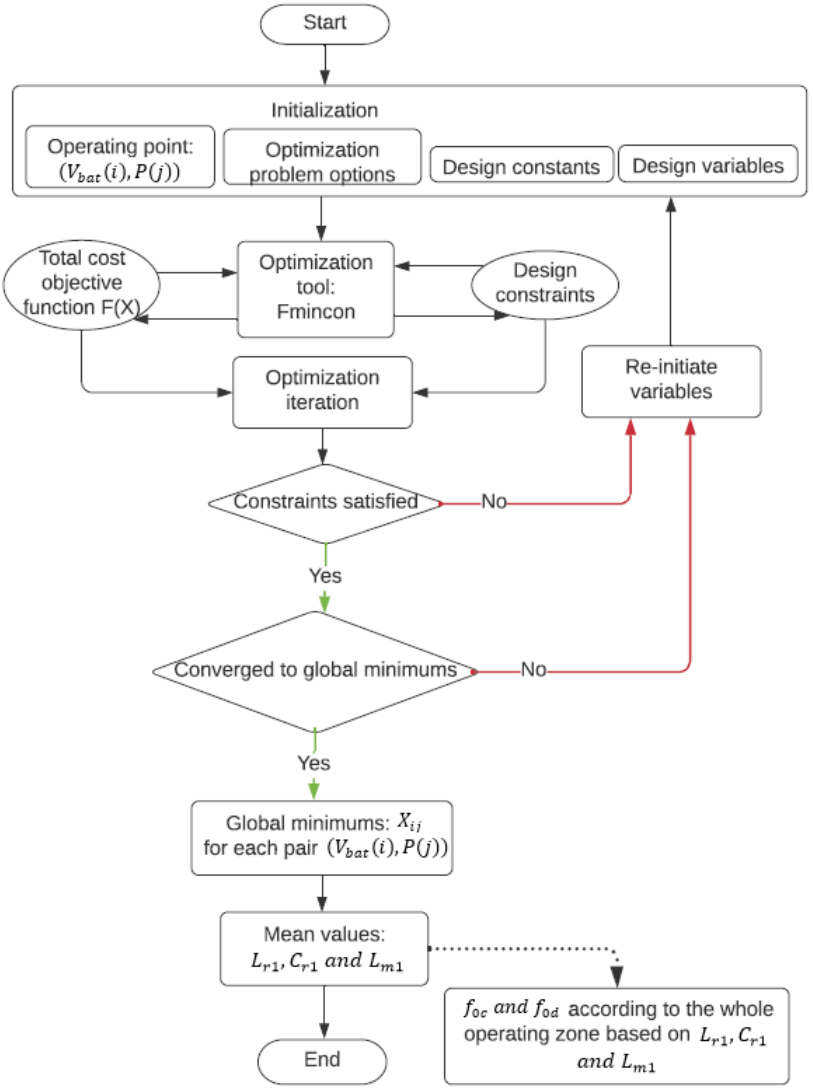

Figure 2.28 – Optimization flow chart.

2.3.3 Simulations and Results

The optimization problem is solved using MATLAB optimization solver fmincon with an Intel Core i7 CPU @ 2.11GH. The DC-DC LLC converter and the control system are implemented in MATLAB/SIMULINK. It should be noted that the simulation parameters are those of a real model of DC-DC LLC converter used in electric vehicle charger. The simulations have been completed using Fixed Step Discrete solver (Sample time = 7.14286 $\times 10^{-8} s$). The parameter settings are shown in Table 2.3.

V_{min}	240 V	V_{max}	430 V
P_{min}	1 kW	P_{max}	11 kW
C_{r0}	200 ηF	L_{r0}	20 μH
L_{m0}	120 μH	n	1.6
f_{max}	200 kHz	f_{min}	60 kHz
C_f	100 μF	C_{mosfet}	0.75 ηF

Table 2.3 – Settings table.

Based on the optimization algorithm, each of L_r, C_r, and L_m has a global minimum for each operating point (each pair (V_{bat},P)). Figures 2.29–2.31 show the global minimums of L_r, C_r, and L_m, respectively, according to the battery voltage and power variation.

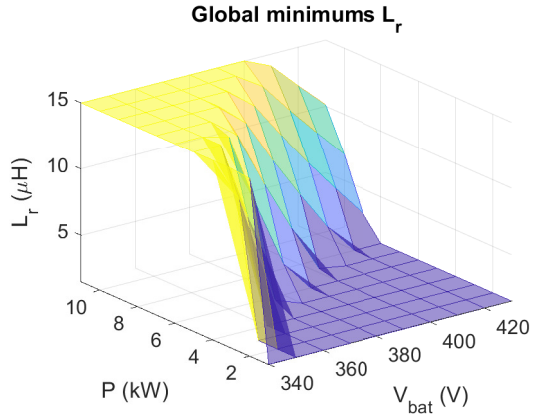

Figure 2.29 – Global minimums of L_r according to battery voltage and power variation.

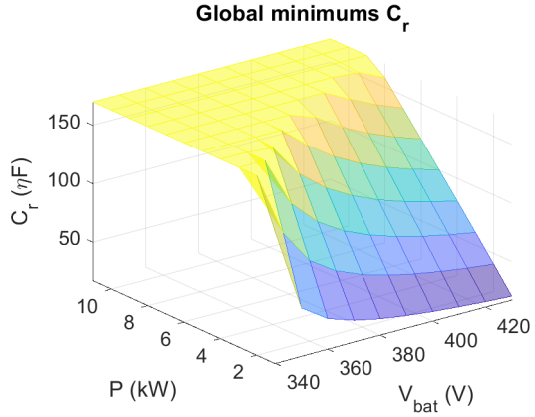

Figure 2.30 – Global minimums of C_r according to battery voltage and power variation.

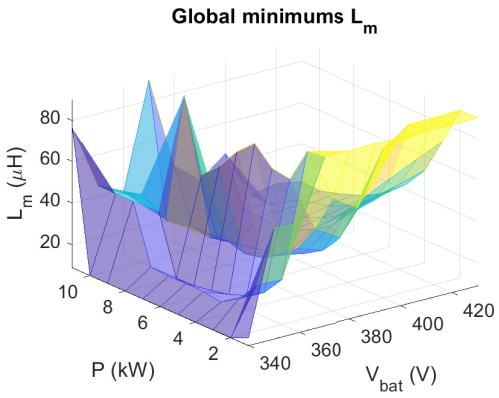

Figure 2.31 – Global minimums of L_m according to battery voltage and power variation.

The mean value of the global minimums for each variable, based on Equations (2.44–2.46), can be obtained as follows:

$$L_{r1} = 6.668\,\mu\text{H}, C_{r1} = 76.62\,\eta F, L_{m1} = 35\,\mu\text{H}$$

It is confirmed that L_r decreased by 67% (from L_{r0} to L_{r1}), C_r decreased by 62% (from C_{r0} to C_{r1}) and L_m decreased by 71% (from L_{m0} to L_{m1}). Therefore, the cost and sizing of the EV charger decreased significantly.

With the mean values L_{r1}, C_{r1} and L_{m1}, the feedforward switching frequencies f_{0c} and f_{0d} in G2V and V2X modes are calculated using Equations (2.15) and (2.24) according to the whole operating zone. f_{0c} and f_{0d} are presented in Figures 2.32 and 2.33, respectively, based on the optimized mean values L_{r1}, C_{r1}, and L_{m1}.

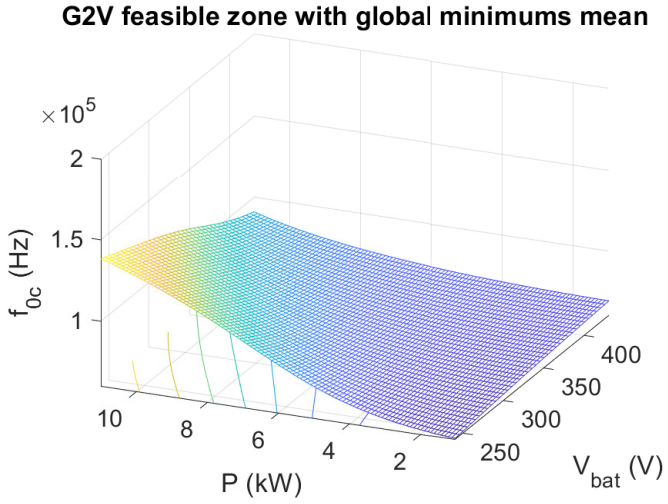

Figure 2.32 – Feedforward frequency in G2V mode based on the optimized values.

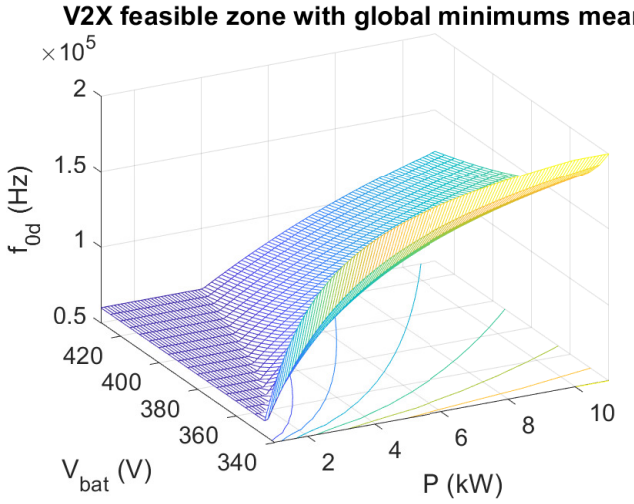

Figure 2.33 – Feedforward frequency in V2X mode based on the optimized values.

It is clearly seen that, in Figure 2.32, f_{0c} is completely within the feasible zone according to the battery voltage and power variation when using the optimized values L_{r1}, C_{r1}, and L_{m1}, unlike in Figure 2.3 where there is a small saturation zone when using the initial values L_{r0}, C_{r0}, and L_{m0}. f_{0c} in Figure 2.32 increases with the increase in the converter power for each battery voltage. On the other side, an important reduction in the saturation zone of f_{0d} is achieved when using the optimized values as presented in Figure 2.33. There is a small saturation zone at f_{min}, while in Figure 2.6 there is an important saturation zone at f_{max}. Moreover, it is clearly seen that f_{0d} is directly proportional to the converter power for each battery voltage, whereas in Figure 2.6 it is inversely proportional.

A comparative study of the DC-DC LLC converter efficiency between initial values (L_{r0}, C_{r0}, and L_{m0}) and optimized values (L_{r1}, C_{r1}, and L_{m1}) is completed according to the power variation for some battery voltages.

It should be noted that the AC-DC converter of the EV charger is used to regulate the grid current, and consequently the DC bus current at the input of the DC-DC converter. The DC bus voltage is regulated by the DC-DC LLC converter to follow the setpoint (450 V). The modulation strategy, i.e., PFM strategy, is implemented based on the small signal modelling of the DC-DC LLC converter to regulate the DC bus voltage by varying the switching frequency. The battery voltage is imposed by the Battery Management System (BMS). In G2V mode, the input power of the DC-DC LLC converter is the product of the DC bus voltage and the DC bus current. The output power is the product of the battery voltage and the battery current. For each operating point, the efficiency is obtained by dividing the average value of the output power at the battery side by the average value of the input power at the DC bus side. Although in the V2X mode, the efficiency is calculated by dividing the average value of the output power at the DC bus side by the average value of the input power at the battery side.

Figures 2.34 and 2.35 show an efficiency comparison in G2V mode with $V_{bat} = 350$ V

and V_{bat} = 390 V, respectively.

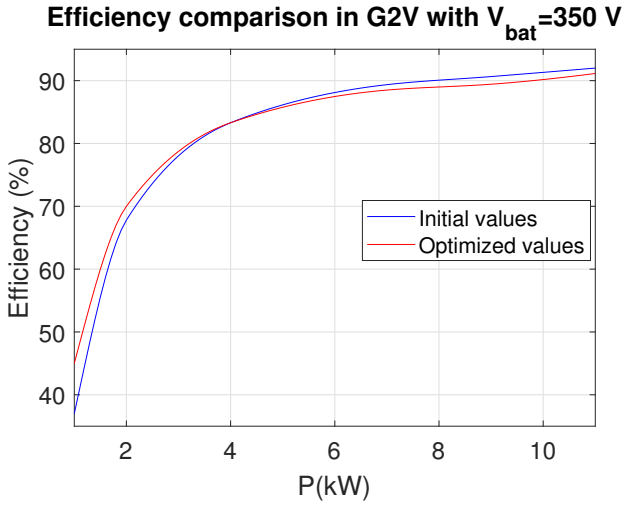

Figure 2.34 – Efficiency comparison in G2V mode with V_{bat} = 350 V.

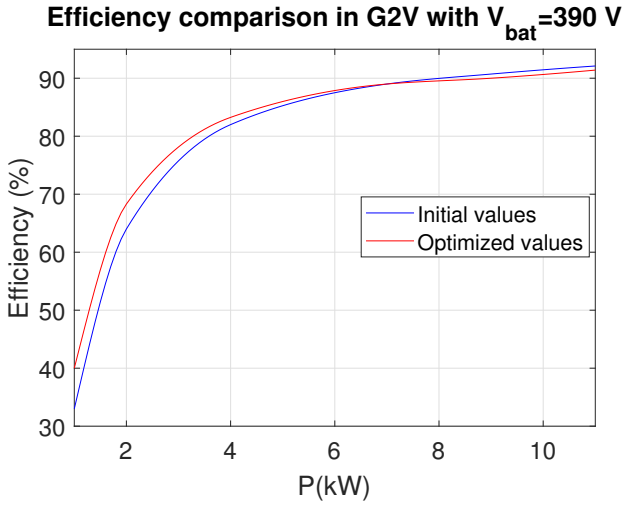

Figure 2.35 – Efficiency comparison in G2V mode with V_{bat} = 390 V.

It is confirmed that, at low powers, there is an important efficiency improvement when using the optimized values. At high powers, when P exceeds 5000 W in Figure 2.34 (with V_{bat} = 350 V) and 8000 W in Figure 2.35 (with V_{bat} = 390 V), the efficiency resulting from initial values is higher than that obtained from optimized values. Actually, looking back at Figure 2.32, it becomes clear that f_{0c} resulting from optimized values increases in parallel with the converter power for each battery voltage. At low powers, it presents values lower than f_{0c} resulting from initial values (Figure 2.3), whereas at high powers, it presents higher values for some battery voltage. Thus, although it is the case of optimized values, the switching frequency at high powers, with V_{bat} = 350 V and V_{bat} = 390 V, is higher than that in the case of initial values, giving higher switching losses and less efficiency as presented in Figures 2.34 and 2.35.

Figures 2.36 and 2.37 illustrate an efficiency comparison in V2X mode.

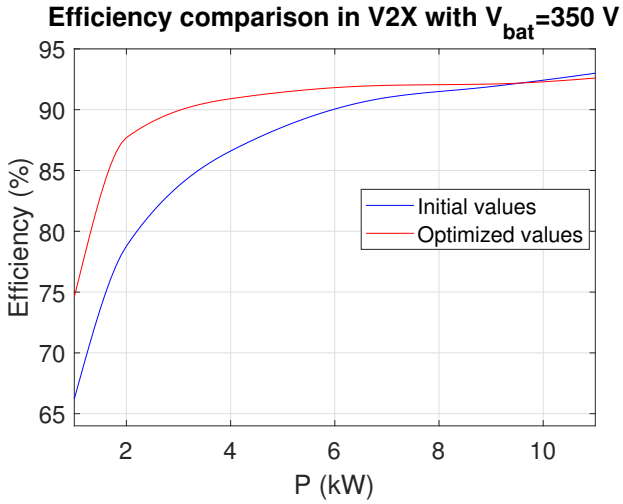

Figure 2.36 – Efficiency comparison in V2X mode with $V_{bat} = 350$ V.

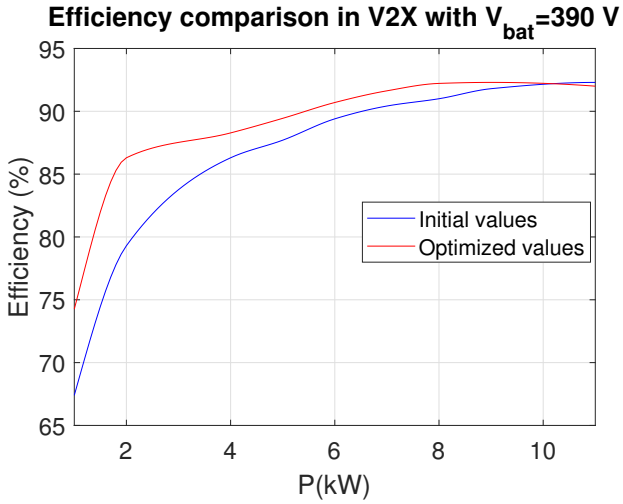

Figure 2.37 – Efficiency comparison in V2X mode with $V_{bat} = 390$ V.

According to these figures, it is confirmed that, at low powers, there is an important efficiency improvement when using the optimized values. For P = 2000 W, the efficiency is 87.7% (with $V_{bat} = 350$ V in Figure 2.36) and 86.3% (with $V_{bat} = 390$ V in Figure 2.37), which is much better than the case of initial values where it is 78.78% (with $V_{bat} = 350$ V) and 79.3% (with $V_{bat} = 390$ V). When P is between 4000 and 8000 W, the efficiency resulting from optimized values is always higher than that resulting from initial values. It remains higher until P exceeds 9500 W for $V_{bat} = 350$ V (Figure 2.36) and 10,500 W for $V_{bat} = 390$ V (Figure 2.37), where it becomes a bit lower. It should be noted that f_{0d} obtained using optimized values (Figure 2.33) increases with the increase in converter power, whereas it decreases when using initial values (Figure 2.6). Thus, when P exceeds 9500 W with $V_{bat} = 350$ V (Figure 2.36) and 10,500 W with $V_{bat} = 390$ V (Figure 2.37), the efficiency obtained from optimized values becomes lower than that obtained from initial values. This is due to the fact that the switching frequency becomes higher when using optimized values, giving higher switching losses in this operating zone.

2.4 Conclusion

The DC-DC LLC resonant converter is widely used for high power applications such as EV charger, which require a high efficiency. Existing control solutions in the literature for this type of converter are mostly related to battery voltage or current control in G2V mode over narrow volatge and power ranges. In this chapter, the effect of several control strategies on the DC-DC LLC converter are designed in V2X mode and implemented according to an averaged small signal model based on FHA. DC bus voltage control, based on the Gain Inversion (GI) method, is highlighted in section 2.2. The drawbacks of PFM strategy are presented. Then, fixed switching frequency strategies, such as PWM and PSM, are proposed to avoid PFM strategy limitations (saturation zone, light load efficiency problem). The benefits and drawbacks of each strategy are studied. It can be concluded that PSM strategy is a suitable strategy to solve PFM strategy drawbacks in the saturation zone, avoid PWM limitations related to FHA constraints, and improve the DC-DC LLC converter efficiency. PSM strategy is an efficient way to improve the charger performance in V2X mode without adding any components in the structure of the DC-DC converter.

From another perspective, a solution in terms of the hardware optimization is proposed in this chapter. The proposed optimization strategies of the DC-DC LLC converter in the literature are mostly intended in one operation mode, i.e. G2V mode, based on narrow voltage and power ranges. An optimized design of the bidirectional DC-DC LLC resonant converter for an EV charger application is proposed in section 2.3. The main goal is to reduce the charger cost and increase the soft-switching range for a wide variation of the battery voltage and power in both G2V and V2X modes. Small-signal modeling of the DC-DC LLC converter with FHA is applied. PFM with GI, presented in section 2.2, is adopted to regulate the DC bus voltage by varying the switching frequency. Decision variables are chosen considering the DC-DC LLC resonant structure and control frequencies in both G2V and V2X modes. Linear and non-linear constraints are defined based on the hardware and control requirements. The control constraints, derived from the control strategy based on the GI method, are included in the optimization strategy. The charger cost is minimized and control frequency feasibility zones are improved. The optimization results show an important improvement in the charger efficiency in both G2V and V2X modes.

3

Robust Control Strategies Design of LLC Converter

3.1 Introduction

Usually, a representative dynamic model of the LLC resonant converter must be defined in order to design a control law.

PSM strategy is proposed in chapter 2 to get around the constraint of the PFM strategy in V2X mode, in order to improve the DC-DC LLC converter efficiency and control the operating points that the PFM strategy cannot reach in V2X mode [20]. Based on a small signal model with FHA, the PSM strategy was implemented in chapter 2 based on the Gain Inversion (GI) method in V2X mode. Small signal modelling allows to obtain a transfer function based on an averaged or linearized mode, which makes the control easy to be achieved. However, it does not take into consideration the non-linear and uncertain effect, including the DC-DC LLC converter structure, which affects the robustness of the applied control law with respect to the system perturbations and causes limited operating zone.

Large signal modelling [40, 42] has been proposed for the DC-DC LLC converter, based on the PFM strategy, to provide enough dynamic information when large signal transient disturbance occurs. However, this model is used with the PFM strategy that needs wide switching frequencies to cover the entire operating zone causing a LLC converter saturation and a reduced efficiency. For this reason, this model will be rewritten in this chapter combined with the PSM strategy that can avoid the PFM limitations. Furthermore, the proposed model based on PSM strategy allows us to design and apply non-linear robust controllers in order to ensure the control robustness against the disturbances.

Linear control laws, such as the GI and PI controller are popularly adopted with the PSM strategy. These controllers require the knoweldge of the DC-DC LLC model. However, in case of any unexpected disturbance, these control laws cause an oscillatory behavior and an important tracking error, which results in a current oscillation in the transformer as well as an overheating. This provides a weak control performance where the DC-DC converter is implemented with the AC-DC converter in the EV charger. Therefore, non-linear control laws are proposed in this chapter in order to ensure the control robustness against the disturbances with unkown boundaries.
Furthermore, to the best of our knowledge, the stability of the DC-DC LLC converter dynamics where the PSM approach was applied, that has not been adequately examined due to the LLC model's complexity, is given in this chapter based on the proposed model.

The new challenge of this chapter, in comparison to prior works, is to provide robust control strategies, such as Model Free Control (MFC) and Adaptive Super Twisting Control (ASTC), in order to guarantee the robustness against unexpected disturbances (DC current disturbance at the side of DC bus due to AC grid disturbance) and uncertainties (measurement error and parameters' variation) with unknown boundaries in the DC-DC LLC converter system. Based on this work, our papers [31] and [32], and patents [29] and [28] have been produced.

On the one hand, the main contribution of the proposed MFC law, based on our paper [31] and patent [29], can be summarized as follows:

- DC bus voltage control as well as robustness guarantee against different disturbances without prior knowledge of the DC-DC LLC converter mathematical model.
- PSM strategy based on MFC implementation for all operating points in V2X mode in order to improve the control performance and the efficiency.
- Comparative study between the MFC and the classic control laws with respect to the DC bus current disturbance and DC bus voltage request variation.

On the other hand, the new challenge related to the ASTC strategy, based on our papers [32] and [30] and patent [28], is divided into four key points:

- Design of an improved model of the DC-DC LLC converter, based on the PSM strategy in V2X mode, in order to get enough information of the LLC dynamics (partially known). The aim of this model is to design the sliding variable by knowing the system's relative degree with respect to the control, and help in the stability proof of the internal LLC converter dynamics.
- Application of the ASTC law to ensure the DC bus request tracking as well as the control robustness in the face of the unexpected disturbances in the DC-DC LLC converter.
- Development of a formal stability proof of the internal LLC converter dynamics, using the small signal perturbation theory, in order to provide necessary requirements for the closed-loop ASTC stability.

- Comparison between the PSM strategy combined with ASTC, MFC and conventional control laws such as PI, GI and Super Twisting Control (STC), in terms of control performance and efficiency.

3.2 Model Free Control combined with PSM strategy

3.2.1 Proposed MFC strategy design

The Model Free Control (MFC) concept has been proposed by Fliess & Join [111] to "robustify" a priori any "unknown" or "poorly known" dynamical system for which are considered uncertainties of the model parameter(s) and unexpected disturbances. It consists of building an ultra-local model of the controlled process from the measurements of the input and output signals without prior knowledge of the mathematical model. The advantage of the MFC is not only to guarantee DC bus voltage request tracking but also to provide robustness with respect to the system disturbances. The principle of the PSM strategy consists in introducing a phase shift between the MOSFETs' control signals where the duty cycle is set to 0.5 and the switching frequency is fixed at 200 kHz for all MOSFETs. The equivalent circuit of the DC-DC LLC converter in V2X mode is presented in Figure 3.1.

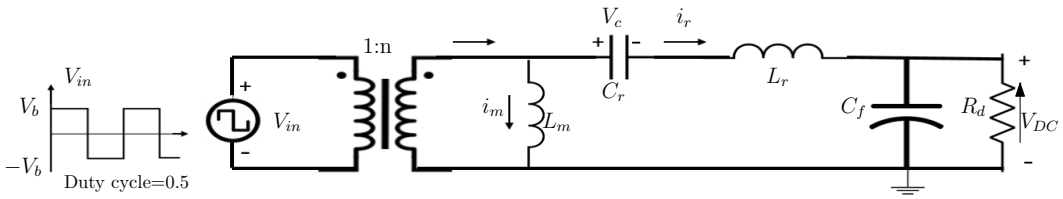

Figure 3.1 – LLC equivalent circuit in V2X mode

Based on Figure 3.1, the square voltage V_{in} represents the input voltage in V2X mode which depends on the battery voltage V_b and the controlled phase shift angle θ. Its fundamental component is expressed in Equation (3.1), which is based on the Asynchronous Clamped Mode (ACM) [17].

$$V_{if} = \frac{n\,V_b}{\sqrt{2}\pi}\sqrt{[10 + 6\,cos(\theta\pi)]} \tag{3.1}$$

The non-linear dynamic equations, based on the LLC equivalent circuit in Figure 3.1, can be defined as in Equations (3.2), (3.3) and (3.4):

$$\frac{di_r}{dt} = \frac{1}{L_r}V_{in} - \frac{1}{L_r}V_c - \frac{1}{L_r}sign(i_r)V_{DC} \tag{3.2}$$

$$\frac{dV_c}{dt} = \frac{1}{C_r}i_r \tag{3.3}$$

$$C_f \frac{dV_{DC}}{dt} = |i_r| - \frac{1}{R_d} V_{DC} \tag{3.4}$$

The system's input-output behavior is governed by a finite-dimensional ordinary differential equation (3.5), which is not always linear, within its operating range:

$$E(y, \dot{y}, ..., y^{(a)}, u, \dot{u}, ..., u^{(c)}) = 0 \tag{3.5}$$

where u is the control input, y is the system output, a is the system order and $c \leq a$. This complex non-linear system can be replaced by the following ultra–local model during very short time interval (3.6) [111]:

$$y^{(\nu)}(t) = F + \alpha u(t) \tag{3.6}$$

where $y^{(\nu)}$ is the derivative of order ν of y, and ν is the relative degree of the system. F contains all the structural information depends on the other variables of the system (including disturbances and non-linearity). α is a constant parameter (with non-physical sens), where the practitioner selects it so that u and $y^{(\nu)}$ have the same magnitude [112]. As a result, it should be obvious that the numerical value of α, which is determined through trial and error, is not a priori precisely determined. Furthermore, it should be emphasized that working with engineers who have a thorough understanding of system behavior is how industrial plant's control has traditionally been managed. The parameter F is constantly updated and encompasses both the poorly known parts of the model and the disturbances, with no need to distinguish between them. Real-time estimation of the numerical value of F [112] allows to update the control every moment.

The MFC is giving as in Equation (3.7) [111]:

$$u(t) = \frac{1}{\alpha} \left[y^{*(\nu)}(t) - \hat{F} + R(e(t)) \right] \tag{3.7}$$

where y^* is the reference and $e(t)$ is the tracking error. R is a classical PI regulator i.e. $R(e(t)) = K_p e(t) + K_I \int e(t)dt$. $\hat{F}$ is the instantaneous estimated value for the coefficient $F(t)$ of the ultra-local model, and it can be expressed, based on Equation (3.6), as in Equation (3.8):

$$\hat{F} = \left[y^{(\nu)} \right]_e - \alpha u(t - h) \tag{3.8}$$

where $\left[y^{(\nu)} \right]_e$ is the ν order estimated derivative of y.

The LLC resonant converter is a non-linear system as a result of many parameters: non-linear dynamic relation between AC (input of the LLC resonant circuit) and DC (DC bus or battery voltage) variables due to MOSFETS' switching operating, inductors' currents, series capacitor voltage, and square voltage across the transformer containing switching frequency harmonics.

For the DC-DC LLC converter, y is the measured DC bus voltage, y^* is the DC bus voltage request and u is the controlled phase shift θ. Then, the complex non-linear LLC

converter system can be written, by taking $\nu = 1$ in Equation (3.6), as in Equation (3.9):

$$\dot{V}_{DC} = F + \alpha\theta(t) \tag{3.9}$$

$\dot{V}_{DC}$ is the first order derivative of V_{DC}. Thus, the instantaneous estimated value for the coefficient $F(t)$ can be obtained, from Equation (3.9), as in Equation (3.10):

$$\hat{F} = [\dot{V}_{DC}]_e - \alpha\theta(t-h) \tag{3.10}$$

where $\hat{F}$ is the instantaneous estimated value of F and $[\dot{V}_{DC}]_e$ is the first order estimated derivative of V_{DC}. $[\dot{V}_{DC}]_e$ can be obtained by using the Euler derivative approximated at first order (h is the step size) (3.11):

$$[\dot{V}_{DC}]_e = \frac{V_{DC}(t) - V_{DC}(t-h)}{h} \tag{3.11}$$

Based on Equation (3.7), the controlled phase shift derived by the MFC strategy can be defined as in Equation (3.12):

$$\theta(t) = \frac{1}{\alpha}\left(\dot{V}^*_{DC} - \hat{F} + K_p e(t) + K_I \int e(t)dt\right) \tag{3.12}$$

with $e(t) = V^*_{DC} - V_{DC}$.
The MFC law is divided into two parts as presented in Equation (3.13):

$$\theta(t) = \underbrace{\frac{-\hat{F}}{\alpha}}_{\text{Robustness insured}} + \underbrace{\frac{1}{\alpha}\left(\dot{V}^*_{DC} + K_p e(t) + K_I \int e(t)dt\right)}_{\text{Closed loop tracking}} \tag{3.13}$$

The first part aims to cancel the effect of the non-linearity and the disturbances, and the second one aims to track the setpoint in the closed loop.
From Equation (3.12), by replacing $\hat{F}$ and $[\dot{V}_{DC}]_e$ by their expressions in Equations (3.10) and (3.11) respectively, the MFC law can be obtained as in Equation (3.14):

$$\theta(t) = \frac{1}{\alpha}\Big[\frac{V^*_{DC}(t) - V^*_{DC}(t-h)}{h} - \frac{V_{DC}(t) - V_{DC}(t-h)}{h} + \alpha\theta(t-h) + K_p e(t) + K_I \int e(t)dt\Big] \tag{3.14}$$

The control block with the MFC strategy is presented in Figure 3.2.

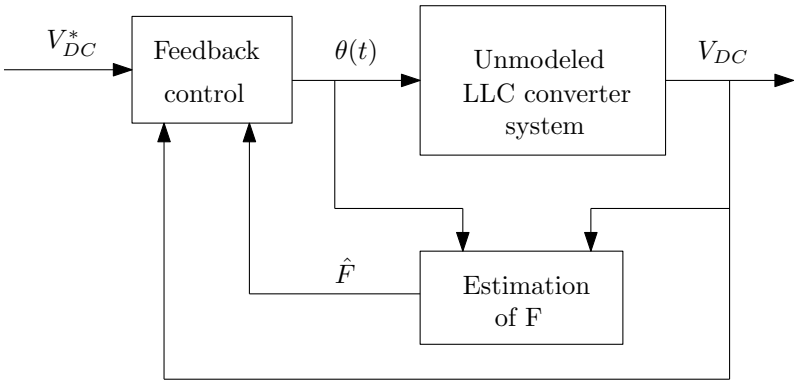

Figure 3.2 – MFC strategy block

Thus, by applying the PSM strategy to the DC-DC LLC converter, the controlled phase shift derived from the MFC strategy can be only obtained based on the DC bus voltage measurement and the DC bus voltage request. The proposed control strategy based on the MFC leads to achieve the DC bus voltage request tracking and provide the robustness with respect to the system disturbances.

3.2.2 Results and simulation

System and simulation configuration

Table 3.1 displays the parameter settings.

$C_f(\mu F)$	75	$K_p(PI)$	0.005
$C_r(\eta F)$	80	$K_i(PI)$	0.0001
$L_r(\mu H)$	30	$K_p(GI)$	0.005
$L_m(\mu H)$	120	$K_i(GI)$	0.0001
n	1.6	$K_p(MFC)$	0.005
$\epsilon(V)$	10	$K_i(MFC)$	0.0001
$T_s(\eta s)$	70	$\alpha(MFC)$	30

Table 3.1 – Model and control system parameters

It should be noted that the maximal authorized overshoot percent and tracking error are 10% and 10 V respectively. The PI gains are tuned by the trial and error process in order to obtain the high performance. Same PI gains are used for all controllers in order to do an efficient comparative study. The parameter α of the MFC is chosen by trial and error in order to respect that the phase shift θ and $\dot{V_{DC}}$ have the same magnitude based on Equation (3.9), and get the high performance.
In this section, a comparative study among the control based on the Gain Inversion (GI) [20], the PI control and the MFC proposed in this chapter, each applied to the PSM strategy is presented. The results show the advantage of the MFC in improving the control performance and the DC-DC LLC converter efficiency.

For the following simulation results, the switching frequency of the DC-DC LLC converter is fixed at 200 kHz for P=2000 W and V_b=420 V. The efficiency is computed by dividing the average value of the DC bus side output power by the average value of the battery side input power. The DC bus request is 450 V and the maximum acceptable voltage tracking error is ϵ (10 V).

Comparison with respect to the DC bus current disturbance

The disturbance is defined as the output of a controlled current source as a sinusoidal signal with magnitude 2 A and frequency 100 Hz, added to the DC current which flows in the equivalent resistor R_d (Figure 3.1) at 0.04 s. Figure 3.3 shows a comparison between the DC bus voltage responses for the various strategies. The controlled phase shift angles are presented in Figure 3.4. It is clearly seen that the proposed MFC strategy is robust unlike the other strategies (GI and PI) with respect to the presented disturbance. Figure 3.5 presents a comparison table between the DC bus voltage responses of the various strategies in terms of closed-loop control performance and efficiency.

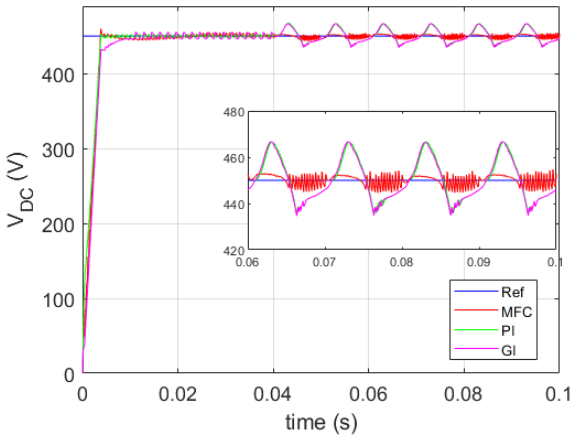

Figure 3.3 – DC bus voltage responses with the current disturbance

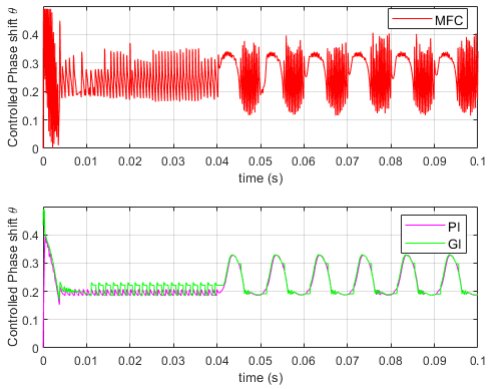

Figure 3.4 – Phase shift response comparison with the current disturbance

V_b=420 V, P=2000 W	GI	PI	MFC
Maximal DC bus voltage tracking error (V)	18	17	5
Settling time (s)	0.01	0.004	0.004
Rising time (s)	0.0038	0.0032	0.0033
Efficiency (%)	75	74	77

Figure 3.5 – Comparison table

At 0.04 s, when the disturbance is added, there is an important DC bus voltage tracking error with GI and PI where it reaches 18 V with GI and 17 V with PI. On the other hand, the DC bus voltage is controlled with the MFC strategy with maximal voltage tracking error of 5 V. This result is due to the advantage of estimating the parameter F in the MFC, which allows to robustify the control, whereas the other control strategies (GI and PI) directly depend on the LLC system variation and require the knoweldge of the disturbance type, which makes them less robust. In addition, the MFC provides settling and rising times which are very close to those in the case of PI and much better than those in the case of GI. The efficiency is improved with the MFC compared to that with the other strategies. Thus, it is confirmed that the proposed MFC strategy leads to achieve the DC bus voltage regulation and provide the control robustness against the unexpected disturbance. Unlike the other control strategies (GI and PI), the MFC is implemented without prior knowledge of the DC-DC LLC converter mathematical model.

Comparison with respect to the trajectory tracking

In this section, the proposed MFC strategy is compared to the existing control (GI and PI) with respect to a varying DC bus voltage trajectory to be tracked. The disturbance is presented as a sinusoidal signal, with magnitude 40 V and frequency 100 Hz, added to the DC bus request at 0.03 s.

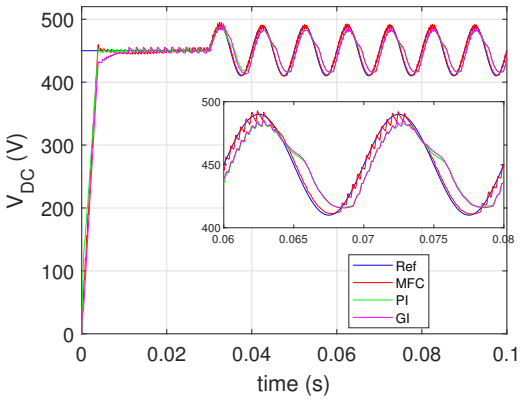

Figure 3.6 – DC bus voltage responses with varying trajectory to be tracked

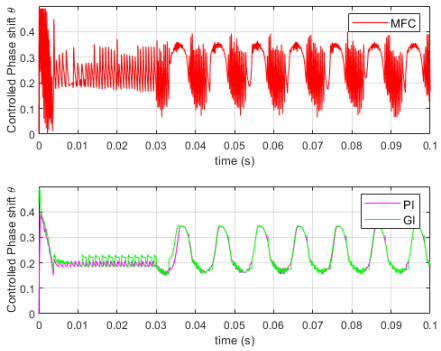

Figure 3.7 – Phase shift response comparison with varying trajectory to be tracked

When the disturbance is added, the DC bus voltage follows the setpoint with an acceptable tracking error in the proposed MFC strategy, whereas there is an important tracking error in GI and PI controllers as presented in Figure 3.6. The controlled phase shift angles are shown in Figure 3.7. The MFC strategy ensures the trajectory tracking due to the advantage of estimating the parameter F in the MFC control law, which allows to robustify the control with respect to the varying DC bus trajectory to be tracked, whereas the existing control strategies directly depend on the DC bus request variation which makes them less robust.

3.3 Adaptive Super Twisting Control combined with PSM strategy

3.3.1 Improved LLC model based PSM

In the literature, an improved model of the DC-DC LLC converter based on the PFM strategy has been designed. However, the application of different control laws for such a model provides a switching frequency saturation for a wide operating zone in V2X mode. This PFM limitation is avoided by applying our proposed PSM strategy based on a small signal model, as described in chapter 2. The existing control laws applied to the PSM are based on the small signal model which is not enough to describe the DC-DC LLC converter dynamics. Moreover, they are based on the PI controller which requires the knoweldge of the LLC model and disturbances making them less robust. From here appears the importance of a non-linear robust control, such as the ASTC, which can be implemented without the knoweldge of the unexpected disturbances (current and voltage disturbance, parameter's variation). An improved model of the DC-DC LLC converter based on the PSM strategy is investigated in this section in order to get enough information of the LLC dynamics (partially known). The aim of this model is to design the sliding variable by knowing the system's relative degree with respect to the control, as well as help later (in Section 3.3.3) to provide a stability proof of the internal LLC converter dynamics.

In V2X mode, Figure 3.1 shows the LLC equivalent circuit. The non-linear dynamic equations of the DC-DC LLC converter are defined in Equations (3.2), (3.3), and (3.4). The resonant tank's AC variables can be divided into sine and cosine components by using the sinusoidal approximation. This decomposition leads to a high-order dynamic model with two states for each AC variable. The following expression (3.15) presents the resonant circuit's input voltage in V2X mode:

$$V_{in}(t) = V_{if}\sin(w_s t) \tag{3.15}$$

with $w_s = 2\pi f$ where f is the switching frequency. V_{if} is the RMS value of the fundamental component of the resonant tank's input defined in Equation (3.1) and is a function of the phase shift θ. In Equations (3.16) and (3.17), the approximation of the series resonant current and its derivative is given:

$$i_r(t) = i_{rs}(t)\sin(w_s t) - i_{rc}(t)\cos(w_s t) \tag{3.16}$$

$$\frac{di_r}{dt} = (\frac{di_{rs}}{dt} + w_s i_{rc})\sin(w_s t) - (\frac{di_{rc}}{dt} - w_s i_{rs})\cos(w_s t) \tag{3.17}$$

Likewise, V_c and $\frac{dV_c}{dt}$ can be divided into sine and cosine components, as shown in Equations (3.18) and (3.19):

$$V_c(t) = V_{cs}(t)\sin(w_s t) - V_{cc}(t)\cos(w_s t) \tag{3.18}$$

$$\frac{dV_c}{dt} = (\frac{dV_{cs}}{dt} + w_s V_{cc})\sin(w_s t) - (\frac{dV_{cc}}{dt} - w_s V_{cs})\cos(w_s t) \tag{3.19}$$

It's worth noting that non-linear terms like $sign(i_r)$ and $|i_r|$ appear in the dynamic Equations (3.2), (3.3), and (3.4). These terms are approximated by their sine and cosine components using the Extending Describing Function (EDF) [113, 40, 41, 42]. As shown in Equations (3.20) and (3.21), they can be presented as:

$$sign(i_r) = \frac{4}{\pi}\frac{i_{rs}}{i_p}\sin(w_s t) - \frac{4}{\pi}\frac{i_{rc}}{i_p}\cos(w_s t) \tag{3.20}$$

$$|i_r| = \frac{2}{\pi}i_p \tag{3.21}$$

where i_p is defined as in Equation (3.22):

$$i_p = \sqrt{{i_{rs}}^2 + {i_{rc}}^2} \tag{3.22}$$

Using the sinusoidal approximation of each variable as given in Equations (3.15), (3.16), (3.17), (3.18), (3.19), (3.20) and (3.21) in the LLC dynamic Equations (3.2), (3.3) and

(3.4), and splitting the sine and cosine terms, the following Equations (3.23), (3.24), (3.25), (3.26) and (3.27), can be obtained:

$$\frac{di_{rs}}{dt} = -w_s i_{rc} - \frac{V_{cs}}{L_r} - \frac{4\, i_{rs}\, V_{DC}}{\pi\, L_r\, i_p} + \frac{n\, V_b}{\sqrt{2}\pi}\sqrt{[10 + 6cos(\theta\pi)]} \tag{3.23}$$

$$\frac{di_{rc}}{dt} = w_s i_{rs} - \frac{V_{cc}}{L_r} - \frac{4\, i_{rc}\, V_{DC}}{\pi\, L_r\, i_p} \tag{3.24}$$

$$\frac{dV_{cs}}{dt} = -w_s V_{cc} + \frac{i_{rs}}{C_r} \tag{3.25}$$

$$\frac{dV_{cc}}{dt} = w_s V_{cs} + \frac{i_{rc}}{C_r} \tag{3.26}$$

$$\frac{dV_{DC}}{dt} = \frac{2\, i_p}{\pi\, C_f} - \frac{V_{DC}}{R_d\, C_f} \tag{3.27}$$

These equations present an improved model of the DC-DC LLC converter which describes the LLC dynamics and provides enough information about the resonant tank, the DC bus and the switching network. This model provides the necessary information of the LLC dynamics (partially known) to design the sliding variable, and to get the system's relative degree with respect to the control (i.e. the DC bus voltage dynamic in function of the phase shift). It also provides the necessary equations to be used in the stability proof of the internal LLC converter dynamics in Section 3.3.3.

3.3.2 Proposed ASTC strategy design

The sliding mode control is well know in the family of robust control laws with respect to system disturbances. For a linear induction motor, the sliding mode twisting technique with adaptive control gains was implemented in [114]. The ASTC principle has been investigated in [115, 116]. The ASTC has been developed for situations when the bounds of disturbances and uncertainty are unknown. The suggested control rule combines the Super Twisting Control (STC) with dynamically adaptive control gains. The fundamental aspect of the adaptation method is that the control gains are not overestimated. The ASTC major characteristic is that it does not only ensure DC bus voltage reference tracking but also provides robustness against system disturbances. The PSM method works by establishing a phase shift between the MOSFET control signals with a duty cycle of 0.5 and a switching frequency of 200 kHz for all MOSFETs. The new challenge is to obtain the controlled phase shift using the ASTC law in order to improve control performance.

It is obviously seen, from Equation (3.23), that the controlled phase shift has an effect on the i_{rs} dynamic. The following change of variable in Equation (3.28) is used to simplify

the design of the ASTC law:

$$u = \sqrt{[10 + 6cos(\theta\pi)]} \tag{3.28}$$

The output of the ASTC law is u. The control's aim is to ensure the DC bus voltage control. Equation (3.27) shows the first order derivative of V_{DC}, which can be expressed as in (3.29):

$$\dot{V}_{DC} = \frac{dV_{DC}}{dt} = a\, i_p - b\, V_{DC} \tag{3.29}$$

where a ($a = \frac{2}{\pi C_f}$) and b ($b = \frac{1}{R_d C_f}$) are constant. The second order derivative of V_{DC} can then be written as in (3.30):

$$\ddot{V}_{DC} = \frac{d^2V_{DC}}{dt^2} = a\frac{di_p}{dt} - b\dot{V}_{DC} \tag{3.30}$$

Based on Equation (3.22), the derivative of i_p can be expressed in Equation (3.31):

$$\frac{di_p}{dt} = \frac{2\frac{di_{rs}}{dt}i_{rs} + 2\frac{di_{rc}}{dt}i_{rc}}{2i_p} \tag{3.31}$$

In Equations (3.23) and (3.24), $\frac{di_{rs}}{dt}$ and $\frac{di_{rc}}{dt}$ are defined respectively. Since u appears in Equation (3.23) (by applying Equation (3.28)), it can be observed that u indirectly appears in the derivative of i_p in Equation (3.31). As a result of Equations (3.23), (3.24), (3.27) and (3.31), $\ddot{V}_{DC}$ in Equation (3.30) can be rewritten as in (3.32):

$$\ddot{V}_{DC} = A(x,t) + B(x,t)u \tag{3.32}$$

where $x = \begin{bmatrix} i_{rs} & i_{rc} & V_{cs} & V_{cc} & V_{DC} \end{bmatrix}$ is the vector of the state variables defined in the five Equations (3.23), (3.24), (3.25), (3.26) and (3.27) of the DC-DC LLC converter model. $A(x,t)$ and $B(x,t)$ are defined as follows in Equations (3.33) and (3.34):

$$A(x,t) = \frac{a\, i_{rs}}{i_p}\left(-w_s i_{rc} - \frac{V_{cs}}{L_r} - \frac{4\, i_{rs}\, V_{DC}}{\pi\, L_r\, i_p}\right) + \frac{a\, i_{rc}}{i_p}\left(w_s i_{rs} - \frac{V_{cc}}{L_r} - \frac{4\, i_{rc}\, V_{DC}}{\pi\, L_r\, i_p}\right) - a\, b\, i_p + b^2\, V_{DC} \tag{3.33}$$

$$B(x,t) = \frac{a\, i_{rs}}{i_p}\frac{n\, V_b}{\sqrt{2}\pi} \tag{3.34}$$

$A(x,t)$ and $B(x,t)$ are functions of the state variables x. They depend on the internal dynamics, which are considered bounded, and they can be presented as bounded disturbances/uncertainties with unknown boundaries.

The relative degree of the sliding variable with respect to the control u should be equal to one in order to apply the ASTC concept. The sliding variable can then be chosen, based on (3.32), as follows (3.35):

$$\sigma = e + k\,\dot{e} \tag{3.35}$$

where $e = V_{DC} - V_{DC}^*$ is the tracking error, V_{DC}^* is a constant DC bus voltage request, and k is a constant that aims to adjust the convergence speed of the DC bus voltage tracking error e when σ is equal to zero (in the sliding surface). Thus, from Equations (3.29), (3.32) and (3.35), the derivative of σ can be expressed as in Equation (3.36):

$$\begin{aligned}\dot{\sigma} &= \ddot{V}_{DC} + \dot{V}_{DC} \\ &= A(x,t) + B(x,t)u + a\,i_p - b\,V_{DC} + a\,\Delta i_p - b\,\Delta V_{DC} + \Delta a\,i_p - \Delta b\,V_{DC} \\ &= A_n(x,t) + B(x,t)u\end{aligned} \tag{3.36}$$

where $\Delta\dot{V}_{DC} = a\,\Delta i_p - b\,\Delta V_{DC} + \Delta a\,i_p - \Delta b\,V_{DC}$ can be considered as an unexpected disturbance, and $A_n(x,t) = A(x,t) + a\,i_p - b\,V_{DC} + a\,\Delta i_p - b\,\Delta V_{DC} + \Delta a\,i_p - \Delta b\,V_{DC}$. $A_n(x,t)$ can include the voltage and current disturbances (like ΔV_{DC} and Δi_p) and uncertainties like parameters' variation (like Δa and Δb).
The ASTC law is defined in Equations (3.37), (3.38) and (3.39) [115]:

$$u = -\alpha|\sigma|^{0.5} sign(\sigma) - \int \beta sign(\sigma) dt \tag{3.37}$$

$$\dot{\alpha} = \begin{cases} w_1 sign(|\sigma| - \mu) & if\ \alpha > \alpha_m \\ \eta & if\ \alpha \leq \alpha_m \end{cases} \tag{3.38}$$

$$\beta = 2\epsilon\alpha \tag{3.39}$$

The first term of u in Equation (3.37) is to ensure the convergence to the sliding surface in the transient state, while the integral term is the responsible of maintaining the tracking error inside the sliding surface in the steady state in the presence of the disturbances. α and β are the control's gains. In the case of a disturbance or uncertainty such as a voltage or current variation included in the term A_n of Equation (3.36), the gain α will adapt to this variation via the adaptive gain law in Equation (3.38) in order to reject the effect of the disturbance (as it will be presented later in the section of simulation results). The parameters ϵ, η, μ, w_1 and α_m are constants. As detailed in [115], the concept of the ASTC is to dynamically increase the control's gains $\alpha(t)$ and $\beta(t)$ until the sliding mode establishes, then the gains will start to reduce. As soon as the sliding variable or its derivative begins to stray from the equilibrium point, this gain must be increased. In order to prevent overestimating the control gains, a detector that recognizes the beginning of a degradation of the sliding mode must be built and included in the ASTC law. The design of this detector is suggested by introducing the domain $|\sigma| \leq \mu$. Thus, the gains $\alpha(t)$ and $\beta(t)$ begin dynamically decreasing once this domain is reached until the system trajectories depart from the domain. Then the gains begin dynamically rising, forcing the trajectories to return to the domain in a finite time. The parameter w_1 (respectively $-w_1$) represents the speed of the $\alpha(t)$ increase (respectively decrease) in the time. α_m is a small positive parameter defined noting that $\alpha(0) > \alpha_m$. When $\alpha(t)$ becomes less or

equal to α_m, its value starts rising immediately (with a variation speed of η) in the sense that $\alpha = \alpha_m + \eta t$ to conserve a high performance and avoid the control saturation.
The controlled phase shift for the PSM approach can be derived from Equation (3.28) using the ASTC u in (3.37) as follows (3.40):

$$\theta = \frac{1}{\pi} \arccos\left(\frac{u^2 - 10}{6}\right) \tag{3.40}$$

The control block of the PSM approach combined with the ASTC is presented in Figure 3.8.

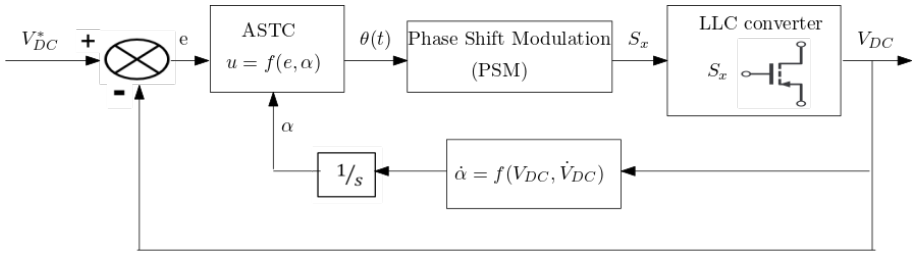

Figure 3.8 – PSM combined with ASTC strategy block

As a result, based on the DC bus voltage request and the DC bus voltage measurement, the controlled phases shift, in Equation (3.40), is derived from the ASTC law. The phase shift angle is used to generate the MOSFETs' control signals (S_x, where x goes from 1 to 8) for the DC-DC LLC converter in order to apply the PSM approach in V2X mode for the entire operating zone.

3.3.3 Internal dynamics stability proof

Considering the non-linear system in Equation (3.41) which describes the control-output dynamics:

$$\dot{\sigma} = A_n(x,t) + B(x,t)u \tag{3.41}$$

$A_n(x,t)$ and $B(x,t)$ can be presented as disturbances and uncertainties related to LLC dynamics with unknown boundaries (these terms, especially $A_n(x,t)$, are functions of the DC bus voltage V_{DC} and current i_p variations). For this kind of systems, it has been proved in [115] that the sliding variable σ and its derivative converge to zero even if the presence of disturbances with unknown boundaries by means of the ASTC. To do so, it is assumed that the internal dynamics of the system are stable. $A_n(x,t)$ and $B(x,t)$ are functions of the LLC state variables defined in the vector x. The stability of the internal dynamics of the LLC model is then crucial in order to guarantee the stability of the ASTC law. In this section, the main contribution consists of providing a stability proof of the internal dynamics of the DC-DC LLC converter to validate theoretically the improved LLC model performance as well as the advantages of the applied ASTC.
The sliding variable σ, defined in Equation (3.35), depends on the DC bus voltage and

its derivative presented in Equation (3.29). By means of the ASTC, σ and $\dot{\sigma}$ are derived to zero. Thus, it is confirmed that in Stead State (SS): $\dot{V}_{DC}$ converges to zero and V_{DC} converges to V^*_{DC}. Based on Equation (3.29), it is clearly seen that i_p converges to i^*_p (when V_{DC} converges to V^*_{DC}), where i^*_p can be defined as follows (3.42):

$$i^*_p = \frac{b\,V^*_{DC}}{a} \tag{3.42}$$

In addition, based on Equation (3.23), it may be easily observed that the ASTC input u in (3.28), which stabilizes V_{DC}, $\dot{V}_{DC}$ and i_p, acts on the i_{rs} dynamic. Besides the effect of the control u, the i_{rs} dynamic include the effect of the variables i_{rc}, V_{cs} and V_{cc}. As a result, the internal dynamics of the DC-DC LLC converter can be defined by Equations (3.24), (3.25) and (3.26).

The variable $x_z = \begin{bmatrix} i_{rc} & V_{cs} & V_{cc} \end{bmatrix}^\top$ is defined as the state variables' vector of the LLC internal dynamics. First of all, it is necessary to obtain $x^*_z = \begin{bmatrix} i^*_{rc} & V^*_{cs} & V^*_{cc} \end{bmatrix}^\top$, the steady state equilibrium point of x_z. It can be achieved by taking the derivatives defined in Equations (3.24), (3.25) and (3.26) to zero. Based on Equation (3.42), the ratio of V^*_{DC}/i^*_p is constant and equal to a/b. Furthermore, the variables i_{rs} and i_{rc} are related by (3.22). Then, i^*_{rs} can be expressed as follows (see Appendix A):

$$i^*_{rs} = \sqrt{(i^*_p)^2 - (i^*_{rc})^2} \tag{3.43}$$

By setting to zero Equations (3.24), (3.25) and (3.26), and applying Equations (3.42) and (3.43), the following equations can be obtained:

$$0 = w_s\sqrt{(i^*_p)^2 - (i^*_{rc})^2} - \frac{V^*_{cc}}{L_r} - \frac{4\,i^*_{rc}\,a}{\pi\,L_r\,b} \tag{3.44}$$

$$0 = -w_s V^*_{cc} + \frac{\sqrt{(i^*_p)^2 - (i^*_{rc})^2}}{C_r} \tag{3.45}$$

$$0 = w_s V^*_{cs} + \frac{i^*_{rc}}{C_r} \tag{3.46}$$

The roots of the non-linear system presented in (3.44), (3.45) and (3.46) represent the equilibrium point x^*_z of the DC-DC LLC converter model. By perturbing the internal dynamics around the equilibrium point, the following expressions can be defined as in Equations (3.47) and (3.48):

$$i_{rs} = i^*_{rs} + \Delta i_{rs} \qquad i_{rc} = i^*_{rc} + \Delta i_{rc} \tag{3.47}$$

$$V_{cs} = V^*_{cs} + \Delta V_{cs} \qquad V_{cc} = V^*_{cc} + \Delta V_{cc} \tag{3.48}$$

Thus, the stability proof of x_z is twofold. On one hand, it is important to validate the stability of the LLC dynamics for the operating point at steady state (i.e for the equilibrium point $V_{DC} = V_{DC}^*$ and $i_p = i_p^*$).
Based on Equation (3.22) and using Equation (3.47), the following Equation can be obtained (3.49):

$$(i_{rs}^* + \Delta i_{rs})^2 + (i_{rc}^* + \Delta i_{rc})^2 = i_p^{*2} \tag{3.49}$$

To make linearization of (3.49) using the small signal assumption, the following relation (3.50) is defined:

$$\Delta i_{rs} = -\Delta i_{rc} \frac{i_{rc}^*}{i_{rs}^*} \tag{3.50}$$

Where i_{rs}^* is always positive (see Appendix A). By applying Equations (3.47), (3.48), (3.50) and (3.42) to the dynamics of x_z presented in Equations (3.24), (3.25) and (3.26), the following system can be obtained:

$$\frac{d(\Delta i_{rc})}{dt} = (-w_s \frac{i_{rc}^*}{i_{rs}^*} - \frac{4\,a}{\pi\, L_r\, b})\Delta i_{rc} - \frac{1}{L_r}\Delta V_{cc} \tag{3.51}$$

$$\frac{d(\Delta V_{cs})}{dt} = -w_s \Delta V_{cc} - \frac{i_{rc}^*}{C_r\, i_{rs}^*}\Delta i_{rc} \tag{3.52}$$

$$\frac{d(\Delta V_{cc})}{dt} = w_s \Delta V_{cs} + \frac{1}{C_r}\Delta i_{rc} \tag{3.53}$$

The variable Z is defined as in (3.54):

$$Z = \begin{bmatrix} \Delta i_{rc} \\ \Delta V_{cs} \\ \Delta V_{cc} \end{bmatrix} \tag{3.54}$$

It is confirmed, based on Equations (3.51), (3.52), (3.53) and (3.54), that the internal dynamics can be presented with the following state space model (3.55):

$$\dot{Z} = D\, Z \tag{3.55}$$

where the matrix D is defined as in (3.56):

$$D = \begin{pmatrix} (-w_s \frac{i_{rc}^*}{i_{rs}^*} - \frac{4\,a}{\pi\, L_r\, b}) & 0 & -\frac{1}{L_r} \\ -\frac{i_{rc}^*}{C_r\, i_{rs}^*} & 0 & -w_s \\ \frac{1}{C_r} & w_s & 0 \end{pmatrix} \tag{3.56}$$

It should be noted that the constant b depends on R_d i.e. a function of the power P which varies between 1 and 11 kW for the EV charger application. The three eigenvalues of D have a negative real part for the entire operating zone, i.e. for the wide power variation.

For a numerical application, the DC bus voltage request $V_{DC}^{*} = 450\,V$ which gives $i_p^{*} = 8.6128\,A$ with $P = 2\,kW$. Based on Equations (3.44), (3.45) and (3.46), $i_{rc}^{*} = 1.794\,A$, $V_{cs}^{*} = -8.398\,V$, $V_{cc}^{*} = 39.432\,V$ and $i_{rs}^{*} = 8.423\,A$. As a result, the eigenvalues of D (3.56) are: $\lambda_1 = -4.6189 \times 10^6$, $\lambda_2 = -4.1816 \times 10^4 + 1.2583 \times 10^6 j$ and $\lambda_3 = -4.1816 \times 10^4 - 1.2583 \times 10^6 j$. Thus, it is confirmed that the internal dynamics of the DC-DC LLC converter are asymptotically stable for the steady state equilibrium point that corresponds to the DC bus voltage request V_{DC}^{*}.

On the other hand, the next step is to validate the stability of the LLC dynamics around the steady state equilibrium point where an unexpected disturbance in the LLC operating point occurs. By perturbing the DC bus voltage around the request with a small signal disturbance, the following Equations (3.57) can be obtained:

$$V_{DC} = V_{DC}^{*} + \Delta V_{DC} \qquad i_p = i_p^{*} + \Delta i_p \tag{3.57}$$

Based on (3.22) and using (3.47) and (3.57), the following equation can be derived (3.58):

$$(i_{rs}^{*} + \Delta i_{rs})^2 + (i_{rc}^{*} + \Delta i_{rc})^2 = (i_p^{*} + \Delta i_p)^2 \tag{3.58}$$

To make linearization of Equation (3.58) using the small signal assumption, the following relation (3.59) is defined as:

$$\Delta i_{rs} = -\Delta i_{rc}\,\frac{i_{rc}^{*}}{i_{rs}^{*}} + \Delta i_p\,\frac{i_p^{*}}{i_{rs}^{*}} \tag{3.59}$$

By applying Equations (3.47), (3.48), and (3.59) to the dynamics of x_z presented in Equations (3.24), (3.25) and (3.26), the following system can be obtained:

$$\frac{d(\Delta i_{rc})}{dt} = (-w_s\,\frac{i_{rc}^{*}}{i_{rs}^{*}} - \frac{4\,a}{\pi\,L_r\,b})\Delta i_{rc} - \frac{1}{L_r}\Delta V_{cc} + w_s\,\frac{i_p^{*}}{i_{rs}^{*}}\Delta i_p \tag{3.60}$$

$$\frac{d(\Delta V_{cs})}{dt} = -w_s \Delta V_{cc} - \frac{i_{rc}^{*}}{C_r\,i_{rs}^{*}}\Delta i_{rc} + \frac{i_p^{*}}{C_r\,i_{rs}^{*}}\Delta i_p \tag{3.61}$$

$$\frac{d(\Delta V_{cc})}{dt} = w_s \Delta V_{cs} + \frac{1}{C_r}\Delta i_{rc} \tag{3.62}$$

The variable Δi_p can be seen as an input for the internal LLC dynamics. It is confirmed, based on Equations (3.60), (3.61), (3.62) and (3.54), that the internal dynamics, in the presence of the disturbance, can be presented as the following state space model (3.63):

$$\dot{Z} = D\,Z + E\,\Delta i_p \tag{3.63}$$

where the matrix D is defined in Equation (3.56) and the matrix E is given as in (3.64):

$$E = \begin{bmatrix} w_s \frac{i_p^*}{i_{rs}^*} \\ \frac{i_p^*}{C_s i_{rs}^*} \\ 0 \end{bmatrix} \tag{3.64}$$

Thus, it is confirmed that, although in the presence of the disturbance, the LLC internal dynamics are still asymptotically stable around the DC bus voltage request. ■
As a result, it has been validated that the LLC model including the internal dynamics is locally stable around the equilibrium point even in the presence of a small signal disturbance. As mentioned before, this stability proof is necessary in order to apply the non-linear ASTC and to validate its stability with respect to the DC-DC LLC converter model represented by Equation (3.41).

3.3.4 Results and simulation

System and simulation configuration

The parameter settings are shown in Table 3.2.

Symbol	Quantity	Value
k	Sliding variable constant	0.5
ϵ	ASTC constant	0.0825
η	ASTC constant	0.0001
μ	ASTC constant	1.5
w_1	ASTC constant	0.00006
α_m	ASTC constant	0.0026

Table 3.2 – Configuration table

The ASTC parameters have been chosen, taking into consideration the physical characteristics of the DC-DC LLC converter, in order to obtain a good performance from both the static and dynamic points of view. It should be noted that the maximal authorized overshoot percent and DC bus voltage tracking error are 10% and 10 V respectively. The gains are tuned by the trial and error process in order to obtain a good performance.

This section compares control strategies based on PI, STC, GI method [20], MFC and ASTC, which are all applied to the PSM approach. The results reveal that the ASTC has a benefit in terms of ensuring the control robustness against disturbances, as well as improving control performances and LLC converter efficiency. For P=2000 W and V_b=420 V, the following results are obtained. It is worth nothing that the DC-DC LLC converter's switching frequency is fixed at 200 kHz. The average output power at DC bus side is divided by the average input power at battery side to get the efficiency. The DC bus voltage request is 450 V, with a maximum authorized voltage tracking error of 10 V.

Comparison with respect to the DC bus current disturbance

The disturbance is represented by a sinusoidal signal with a magnitude of 2 A and a frequency of 100 Hz that is added to the DC current, flowing through the equivalent resistor R_d (Figure 3.1), at 0.04 s. Figure 3.9 shows a comparison of the DC bus voltage responses for the various controllers. The phase shift angles are shown in Figure 3.10. The adaptive control gain α of the ASTC is shown in Figure 3.11. Figure 3.12 shows the series inductor current i_r for the different strategies.

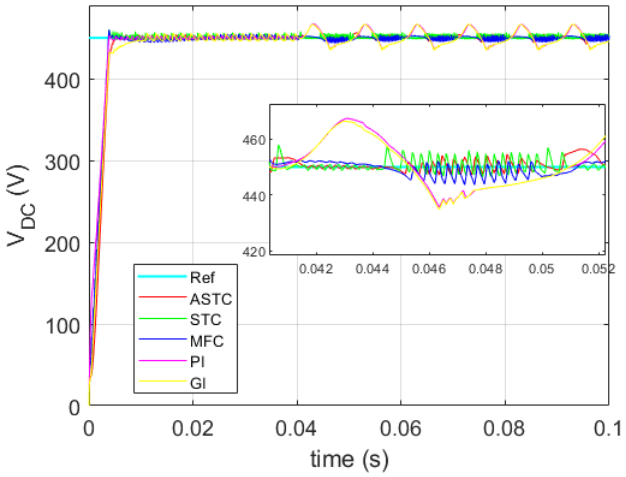

Figure 3.9 – DC bus voltage response comparison with the current disturbance

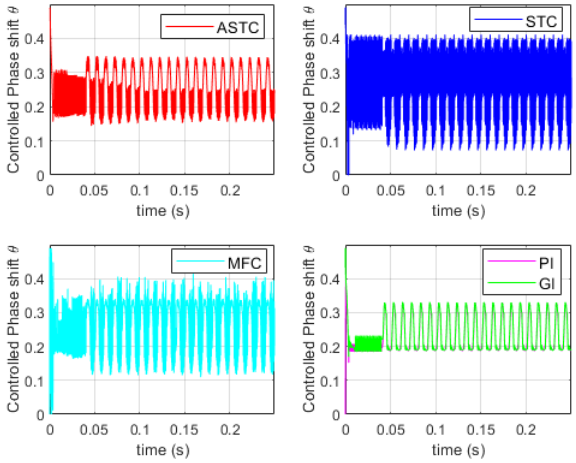

Figure 3.10 – Controlled phase shift angles with the current disturbance

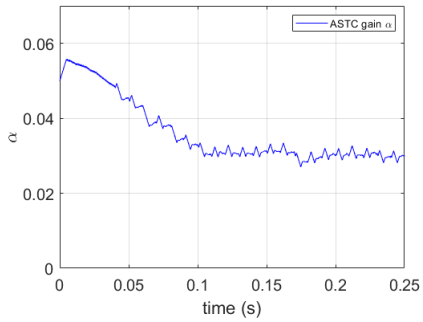

Figure 3.11 – ASTC gain with the current disturbance

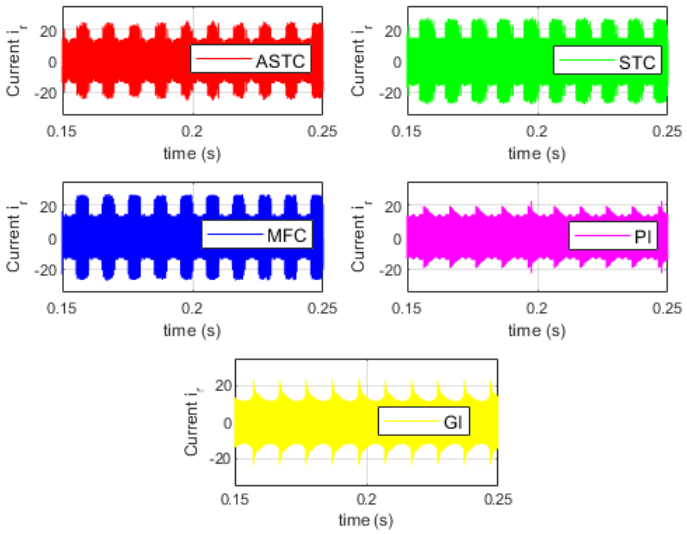

Figure 3.12 – Series resonant current with the current disturbance

In comparison to the GI and PI controllers, the proposed ASTC, like STC and MFC, is clearly robust with respect to the presented disturbance. The GI and PI are linear controllers that depend immediatly on the LLC model, which make them less robust. As presented in Figure 3.9, when the current disturbance is injected at 0.04 s, there is an important DC bus voltage tracking error with GI (reaching 18 V) and PI (reaching 17 V). On the other hand, the DC bus voltage is controlled in case of MFC, STC and ASTC, with a maximum tracking error of 5 V.

The controlled phase shift with STC produces the highest frequency oscillation in the presence of the current disturbance, as seen in Figure 3.10, due to the chattering phenomenon of the sliding mode. Moreover, it is clearly seen that the MFC presents higher frequency oscillation than the ASTC. In fact, as presented in Equations (3.37) and (3.38), the adaptive control gain α of the ASTC, shown in Figure 3.11, adapt in order to reject the effect of the disturbance. The chattering in ASTC is reduced, and the controlled phase shift has a significantly lower frequency oscillation than that in STC and MFC which have constant gains, resulting in reducing the switching losses. It should be noted that both MFC and STC have constant control gains but the chattering caused by the sign function

of the STC leads to have higher control's frequency oscillation than the MFC.
Based on Figure 3.12, even if PI and GI has the lowest maximal RMS value of the resonant current i_r, but they present an important DC bus voltage tracking error. On the other hand, it is clearly seen that the ASTC provides lower maximal RMS current (peak value of 22.2 A) than both MFC (peak value of 26.4 A) and STC (peak value of 26.5 A) resulting from the chattering reducing and the adaptive ASTC gain in the presence of the current disturbance. This advantage of the ASTC leads to reduce the conduction losses in the DC-DC LLC converter.
A comparison table is shown in Figure 3.13 that compares the DC bus voltage responses of the various controllers in terms of the control performance and efficiency.

V_b=420 V, P=2000 W	GI	PI	MFC	STC	ASTC
Maximal DC bus voltage tracking error (V)	18	17	5	6	5
Settling time (s)	0.01	0.004	0.004	0.0039	0.0045
Rising time (s)	0.0038	0.0032	0.0033	0.00285	0.0029
Overshoot percent (%)	0	0.6	0	2.2	1.3
Efficiency (%)	75	74	77	69.5	79
Control's energy consumption index J	0.0107	0.0142	0.0187	0.0253	0.0173

Figure 3.13 – Comparison table in the presence of the current disturbance

The index J can be considered as an energy consumption index of the control system. It is defined as $J = \sum_{k=1}^{m} \theta^2(k)$ (m corresponds to the final time). It contains the energy of the controlled phase shift angle.
It has been verified that the controller energy consumption with ASTC (J=0.0173) is lower than that with MFC (J=0.0187) and STC (J=0.0253). This result is coherent with Figure 3.10, where ASTC has less switching losses than MFC and STC, resulting in an improved efficiency as shown in the table of Figure 3.13. The ASTC law is based on a sliding mode algorithm. However, the chattering is reduced, which is achieved by adding an adaptive control gain law to cancel the overestimation of the gains and guarantee the robustness versus the disturbances. Furthermore, as shown in the compariosn table, the ASTC gives settling and rising times that are extremely near to those with PI, STC, and MFC and better than those with GI.
As a result, it has been confirmed that the proposed PSM strategy combined with the ASTC ensures the DC bus voltage control robustness against unexpected disturbances in the DC-DC LLC converter with better performance than other controllers.

Comparison with respect to the trajectory tracking

The disturbance is represented by a sinusoidal signal with an amplitude of 40 V and a frequency of 100 Hz that is injected to the DC bus voltage request at 0.03 s.

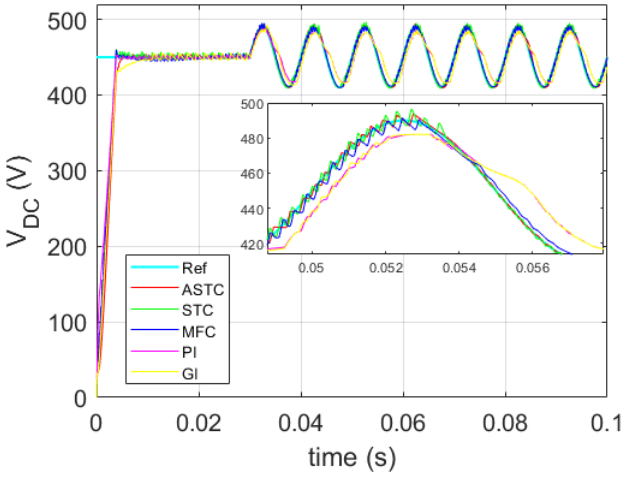

Figure 3.14 – DC bus voltage response comparison with varying trajectory to be tracked

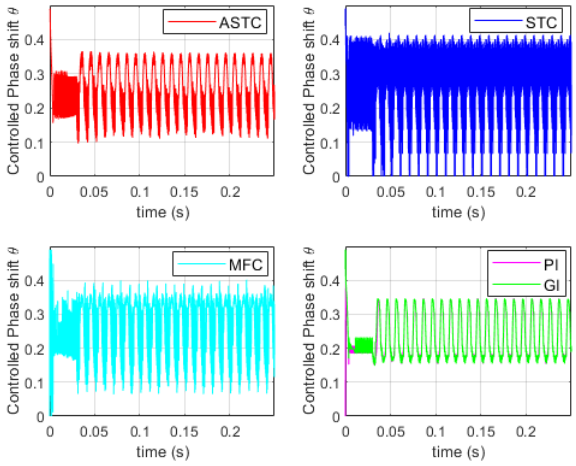

Figure 3.15 – Controlled phase shift angles with varying trajectory to be tracked

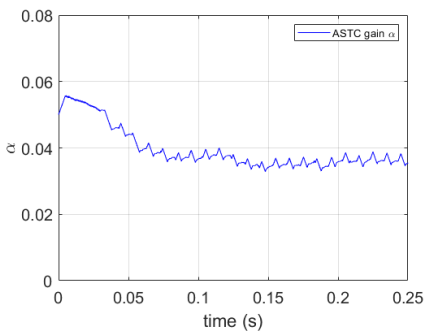

Figure 3.16 – ASTC gain with varying trajectory to be tracked

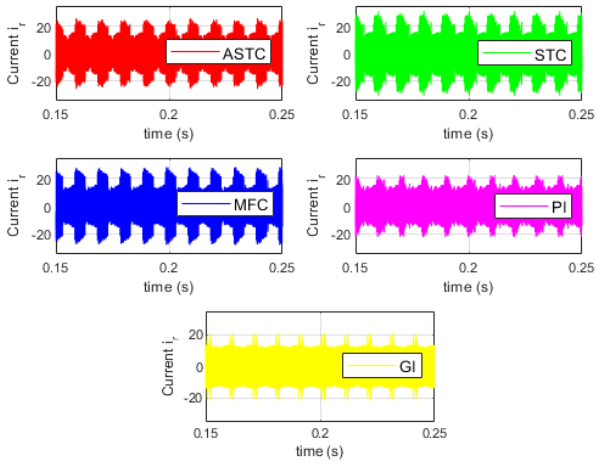

Figure 3.17 – Series resonant current with varying trajectory to be tracked

The proposed ASTC, like STC and MFC, can guarantee the DC bus voltage request tracking, as shown in Figure 3.14. The GI and PI techniques have a significant tracking error because they are directly affected by parameter variation, which makes them less robust. Furthermore, due to the advantage of adjusting the control gain, ASTC provides a controlled phase shift angle with a lower oscillation frequency than STC and MFC as presented in Figure 3.15. The ASTC gain is shown in Figure 3.16 which decreases with respect to the DC bus request variation in order to reduce the controlled phase shift angle oscillation and switching losses. In Figure 3.17, it is confirmed that the ASTC provides lower RMS series resonant current (peak value reaches 26 A) than MFC (peak value of 28 A) and STC (peak value of 31.5 A). A comparison table between the different controllers is presented in Figure 3.18 which reveals the superiority of the ASTC.

V_b=420 V, P=2000 W	GI	PI	MFC	STC	ASTC
Maximal DC bus voltage tracking error (V)	20	20	5	6	6
Settling time (s)	0.01	0.0034	0.0044	0.0037	0.0047
Rising time (s)	0.0036	0.0036	0.0034	0.0034	0.0037
Overshoot percent (%)	0	0.6	2.2	1.1	0
Efficiency (%)	68.1	68.5	75	59	79
Control's energy consumption index J	0.0149	0.0145	0.0187	0.0214	0.0181

Figure 3.18 – Comparison table with varying trajectory to be tracked

3.4 Conclusion

In this chapter, robust control techniques for the bidirectional LLC converter in V2X mode have been proposed to improve control performances. Across the whole operating zone, the Phase Shift Modulation (PSM) approach is applied.

Firstly, a control strategy based on the MFC is highlighted. The proposed MFC provides a robust control law against disturbances without prior knowledge of the DC-DC LLC converter model. A comparative study between the PSM strategy based on the classical control laws and that based on the MFC is presented.

On the other hand, an improved model of the DC-DC LLC converter based on the PSM strategy has been designed in order to get enough information about the DC-DC LLC converter dynamics (partially known), as well as provide the base of a stability proof of the internal LLC dynamics. The non-linear ASTC has been proposed to provide the DC bus voltage control and ensure the robustness in the event of disturbances. A theoretical study of the DC-DC LLC converter model and the PSM approach combined with the ASTC has been developed. The stability of the DC-DC LLC converter dynamics has been analytically proven. Simulation results have been presented to verify the proposed ASTC strategy under several disturbances which demonstrate a great agreement with the theoretical analysis. A comparison of the ASTC, MFC and conventional control laws (such as STC, PI and GI), is conducted in terms of the control performance and efficiency, which proves the superiority of the ASTC.

The results show that the PSM strategy combined with MFC and ASTC has advantages in terms of improving the control performance and LLC converter efficiency, as well as ensuring control robustness in case of LLC converter disturbances.

4

Bidirectional Electric Vehicle Charger Control

4.1 Introduction

The OnBoard EV charger is installed inside the vehicle and provides power conversion and voltage/current control. The design of battery chargers, and particularly for OnBoard chargers, depends on the following criteria: high efficiency; small size and weight, which is related to the optimization of charger power converters (as studied in chapter 2) to ensure high power density and to improve the performance of EV; reversibility, i.e. operating in both charging and discharging modes, with a high performance; low harmonics distortion; and control robustness, as presented by the proposed non-linear control law in chapter 3.

The bidirectional EV charger is connected from one side to the High Voltage (HV) battery of the EV, and from the other side to an alternating electric grid. It has the potential to improve power grid stability while also relying heavily on renewable energy sources [8].

In order to implement the AC-DC conversion function with galvanic isolation, it is common to use a charging device comprising a first AC-DC converter, which comprises a Power Factor Correction (PFC) circuit in order to limit the input current harmonics, and a second DC-DC converter, which provides the DC bus voltage regulation and the isolation function for the safety of use. An input filter is conventionally integrated at the input of the OnBoard charging device, upstream of the PFC circuit with respect to the three-phase electrical grid. Figure 4.1 shows an equivalent scheme for a bidirectional battery charger. The G2V and V2G modes are provided via bidirectional AC-DC and DC-DC converters.

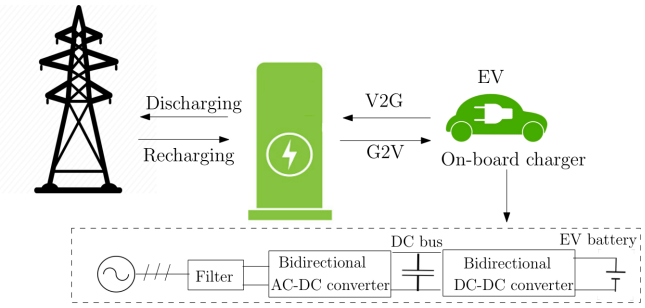

Figure 4.1 – Bidirectional EV charger topology

In the literature, different charger topologies have been presented, such as an EV charger with a three-port parallel resonant topology [103], three-phase two-level Voltage Source Inverter (VSI) [104], bidirectional single-phase AC-DC battery charger with an Eight-Switch Inverter (ESI) [102].
Compared to the literature, a bidirectional EV charger including an AC-DC Vienna topology connected to two DC-DC LLC converters is studied in this chapter.
Regarding the studied charger topology, it is critical to regulate the DC bus voltage when the battery voltage is enforced by the Battery Management System (BMS) with a wide variation range (from 240 to 440 V), and a wide power variation (0-11 kW for the single-phase charger and 0-22 KW for the three-phase charger).

The role of the AC-DC converter is to improve the grid's quality, reduce the current harmonics and maintain a regulated grid current with a high power factor. Although there is a variety of AC-DC converter topologies, the Vienna rectifier topology [117] is popular for active three-phase power factor conversion because of its continuous conduction mode operation, intrinsic three level switching, and decreased voltage stress on the power components.
The isolated bidirectional DC-DC LLC resonant converter [20, 21, 15], studied in chapters 2 and 3, is considered to ensure the battery charging/discharging due to its wide ZVS range [70] and high power density with a high switching frequency [68, 69].

In chapter 2, the PFM strategy is applied to the DC-DC LLC converter alone. However, the switching frequency zone is limited in order to achieve ZVS causing a DC-DC LLC converter saturation in both G2V and V2G modes. This frequency feasibility constraint creates a cost-cutting challenge in the EV charger's software and hardware. In chapters 2 and 3, the PSM strategy, combined with linear and non-linear control laws respectively, is also applied to the DC-DC LLC converter alone in order to avoid the PFM drawbacks in V2G mode.
The new challenge of this chapter is to provide a control strategy of the bidirectional EV charger including the AC-DC converter as a PFC, and the DC-DC LLC converter studied in chapters 2 and 3. The AC-DC converter is used to ensure the DC bus voltage control when the DC-DC LLC converter is saturated in G2V mode. In V2G mode, this solution

is not relevant because it requires a variable DC bus voltage request out of the feasible zone. Thus, the PSM strategy, presented in chapter 2, is applied to the DC-DC LLC converter that is implemented beside the PFC in the EV charger. In both G2V and V2G modes, the AC-DC converter is the responsible to ensure the grid currents control. Based on this chapter, our paper [33] and patent [27] have been produced. The contributions can be summarized as follows:

- Guarantee of the DC bus voltage control for the whole operating zone of the bidirectional EV charger in both G2V and V2G modes
- Improvement of the grid current control performance ensured by the AC-DC converter
- Improvement of the bidirectional EV charger efficiency in both G2V and V2G modes

In G2V mode, two solutions are proposed to ensure the DC bus voltage control and avoid the PFM strategy drawbacks:

- Implementation of the PFM strategy with a variable DC bus voltage request
- Design and implementation of a backstepping control strategy by the help of the AC-DC converter

In V2G mode, the main idea consists of:

- Implementation of the PSM strategy with a fixed switching frequency, studied in chapter 2, in order to improve the control performance and efficiency and cover all the operating points

Outside of the saturation zone of the DC-DC converter, the PFM strategy with a fixed DC bus voltage request is implemented in both G2V and V2G modes.

4.2 Problem statement

4.2.1 EV charger synoptic description

In this thesis, the synoptic outline of EV charger's hardware and software is presented in Figure 4.2.

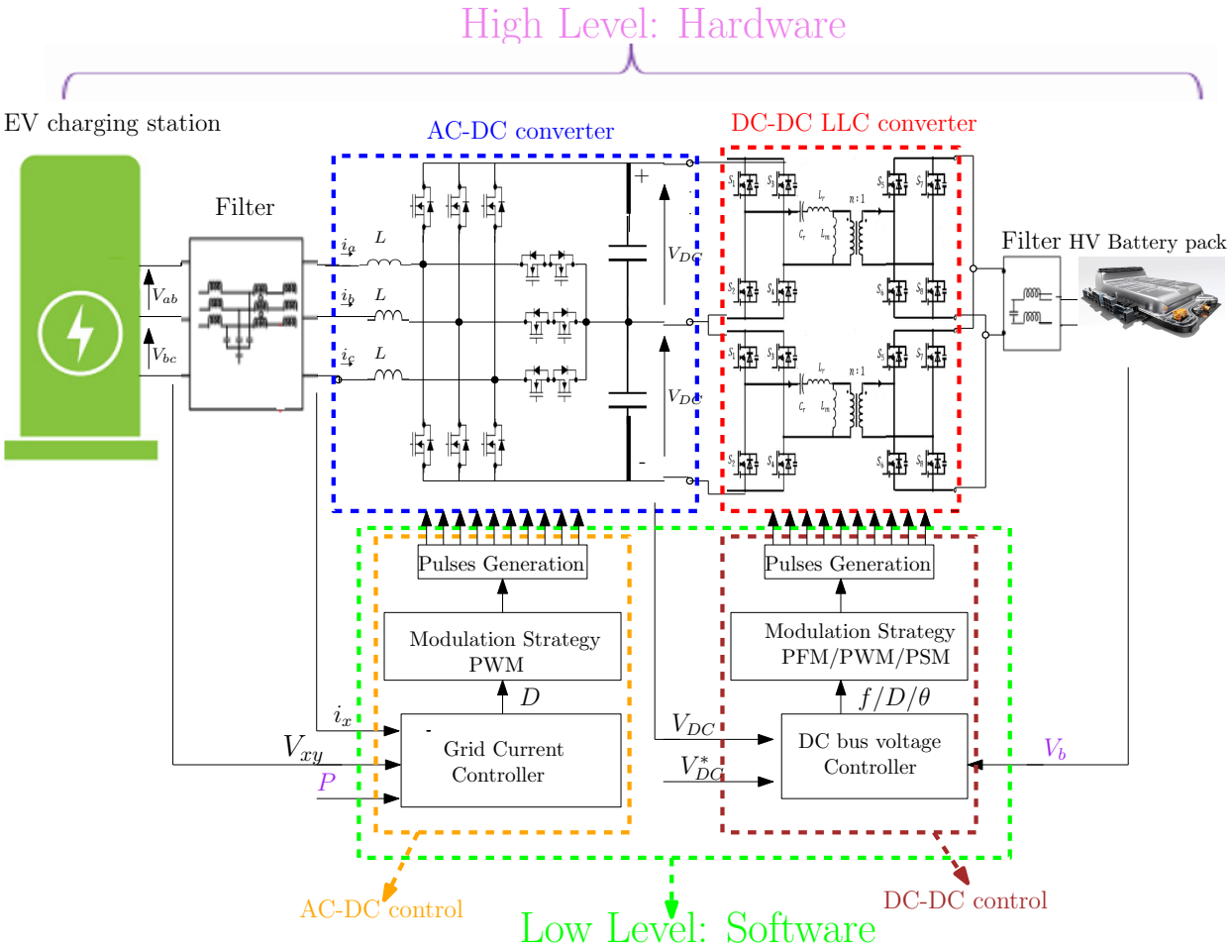

Figure 4.2 – Synoptic outline of EV charger's hardware and software

The EV charger is a link between the EV charging station, which provide the three-phase power supply from the grid, and the HV battery pack. There are two levels in the EV charger system: High level or Hardware and low level or Software.

On the one hand, the hardware of the studied EV charger is composed from: an input filter connected to the grid, an AC-DC converter connected to two DC-DC LLC converters, an output filter connected to the HV battery pack.

On the other hand, the role of the software is to provide the control strategies of AC-DC and DC-DC converters based on the output measurements from the Hardware (Phase to phase voltage V_{xy}, phase current i_x, DC bus voltage V_{DC} and battery voltage V_b) and the power request P. Each control strategy can be divided into three steps. Firstly, the control laws should be defined in order to ensure the stability of the grid current via the AC-DC converter and of the DC bus voltage via the DC-DC converter. Then, a modulation strategy should be implemented. The output of the controller is the input of the modulation strategy block. It can be a duty cycle, a switching frequency or a phase shift in the case of PWM, PFM or PSM respectively. Finally, the pulses are generated based on the defined modulation strategy in order to derive the MOSSFETs' gates.

4.2.2 AC-DC converter study

For the PFC circuit, a three-phase three-switch three-level rectifier is widely used for high power applications and commonly known as the three-phase Vienna rectifier. The choice of this topology is in fact particularly advantageous from the point of view of power factor correction performance.
The three phase AC-DC VIENNA rectifier, boost type bidirectional power flow, is shown in Figure 4.3.

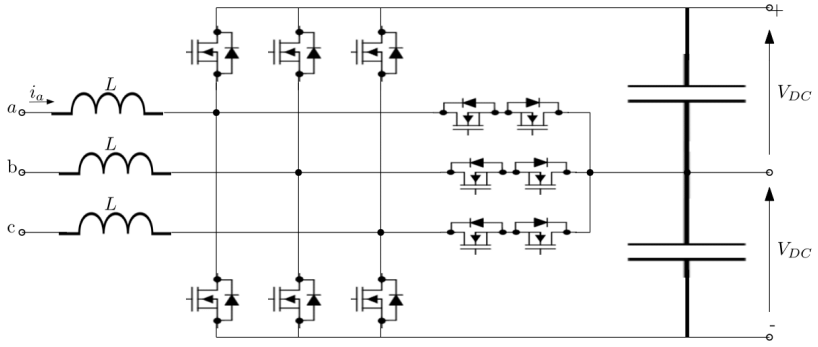

Figure 4.3 – Bidirectional Vienna AC-DC topology

Due to the three-level property, this architecture has a lower semiconductor voltage stress, minimal EMI, low switching losses, and requires a low input inductance.
The input inductors are identical and have the same value L. The neutral point of three-phase line voltage is connected to the DC bus capacitors. The DC bus voltage is V_{DC}. The DC-midpoint voltage is balanced by isolated DC-DC converters. Each phase leg consists of two MOSFETs which guaranties the bidirectional operating of the AC-DC converter. Each power bridge arm consists of two reverse series switches that allow two-way current flow.
The PFC circuit is managed by an integrated controller, which analyzes and regulates the current waveform with respect to the voltage in real time. It deduces the shape errors by comparison with the rectified voltage and it regulates them by controlling the power quantity thanks to high-frequency switching and energy storage in an inductor. Its role is more precisely to obtain a current that is not phase-shifted and as sinusoidal as possible at the input of the charger power supply. The PFC circuit being a three-phase Vienna rectifier comprising three switching arms each suitable for being connected to one of the respective phases of the three-phase grid via a series inductance coil and each comprising a series connection of a high switch capable of being driven when the grid current is positive and of a low switch capable of being driven when the grid current is negative, each arm being driven using PWM control signals whose the duty cycle is determined as a function of setpoint current values at the input of the converter.

Each DC bus capacitor is connected to a bidirectional DC-DC LLC resonant converter. Note that the DC bus voltage V_{DC} is controlled independently by the DC-DC LLC converter.

4.2.3 DC-DC converter study

The bidirectional DC-DC LLC converter is studied in chapters 2 and 3. The converter structure, shown in Figure 4.4, is detailed in section 2.2 of chapter 2. As a reminder, the aim of chapters 2 and 3 is to control the DC bus voltage V_{DC} of the DC-DC LLC connverter alone across the variation of the battery voltage V_b and the converter power P.

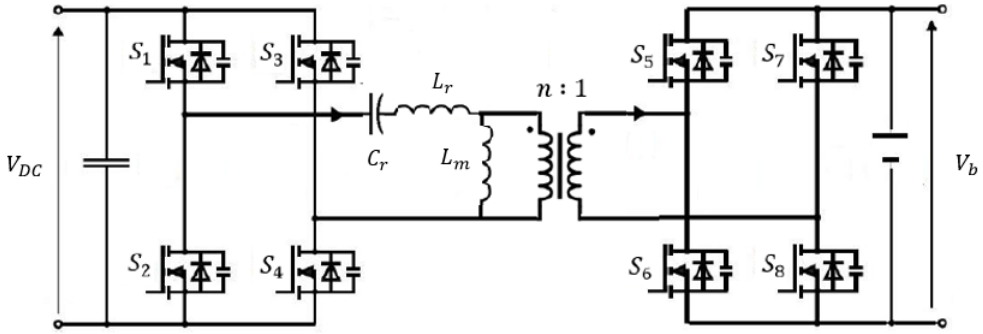

Figure 4.4 – DC-DC LLC converter

In chapter 2, the PFM strategy applied for the DC-DC LLC converter is discussed. It consists of varying the switching frequency of MOSFET control signals with a fixed duty cycle of 0.5.

The large variation in the operating zone, i.e. battery voltage and power variation, implies a large variation in the DC-DC converter gain to ensure the DC bus voltage control around the setpoint. This gain can therefore differ from an operating point to another.

The PFM strategy has been designed based on a Gain Inversion (GI) method, in section 2.2 of chapter 2, in both G2V and V2G modes in order to ensure the DC bus voltage control to a certain setpoint (450 V).

The GI method allows one to define an expression feedforward f_0 of the switching frequency that depends on the resonant circuit parameters, the power request, the DC bus voltage, and the battery voltage. The feedforward switching frequencies f_{0c} and f_{0d} are obtained based on Equations (2.15) and (2.24) in G2V and V2G modes respectively. The control blocks of the PFM strategy based GI are shown in Figures 2.4 and 2.7 respectively. In order to respect the ZVS condition, the control switching frequency should vary between 60 kHz and 200 kHz to ensure the ZVS condition. In Figures 4.5 and 4.6, the feedforward switching frequencies, obtained from the GI method, are presented in G2V and V2G modes respectively according to battery voltage and power variation.

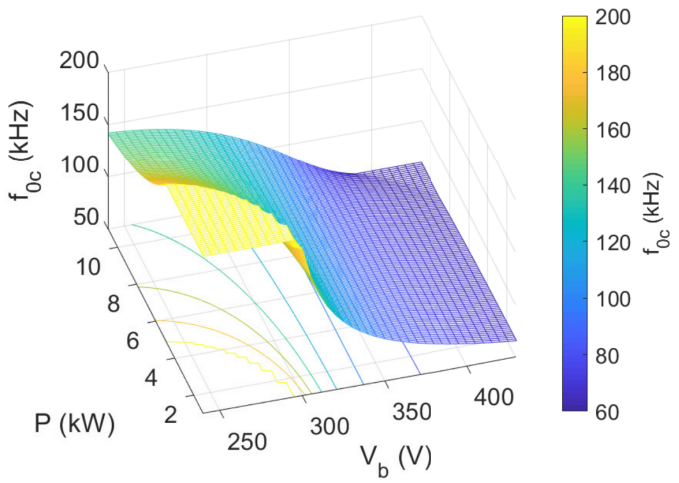

Figure 4.5 – Feedforward frequency in G2V mode according to the battery voltage and power variation

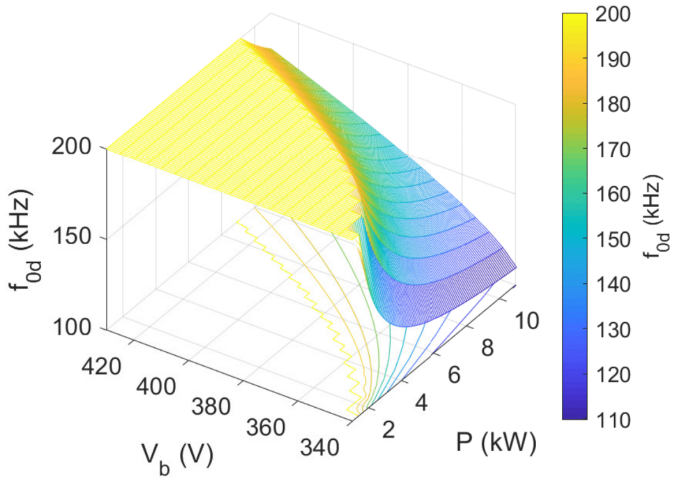

Figure 4.6 – Feedforward frequency in V2G mode according to the battery voltage and power variation

As discussed in chapter 2, the yellow zone, in Figures 4.5 and 4.6, represents an operating zone where the control frequency is saturated at 200 kHz (maximal authorized switching frequency). In G2V mode, there is a small frequency saturation zone when operating in the zone of low battery voltage and low power. In V2G mode, there is an important frequency saturation zone (much higher than that in G2V mode).
The saturation zones affect the ZVS property for the DC-DC LLC converter, resulting in a low EV charger conversion efficiency and a significant DC bus voltage tracking error with the PFM strategy.
In order to avoid the PFM strategy limitations and ensure the control robusness, the PSM strategy based on the GI method and non-linear robust controllers (such as MFC and ASTC) is applied for the DC-DC LLC converter in chapters 2 and 3 respectively.

On the other hand, when the DC-DC LLC converter is implemented in the EV charger, a control strategy for the entire charger including the AC-DC converter should be designed and applied in order to provide good control performance and charger efficiency.
Furthermore, due to the fact that with the EV charger topology presented in this chapter, each DC bus capacitor at the output of the AC-DC converter is connected to a DC-DC LLC converter. Thus, the DC bus voltage should be controlled in order to ensure the AC-DC control strategy performance. From here, the DC-DC LLC converter saturation zones, resulting from the PFM strategy in G2V and V2G modes, affect the grid current control and reduce its performance.
As a result, in the two operating modes G2V and V2G, some operating points depending on battery voltage and power request, are not reachable with the PFM strategy. The control frequency range of the DC-DC LLC converter is not sufficient to reach all operating points of the EV charger.

Consequently, there is the need to find a solution to ensure the DC bus voltage control of the bidirectional charger even when the DC-DC LLC converter is saturated. To do so, a method for the bidirectional charger control comprising bidirectional AC-DC converter and DC-DC converter control strategies is proposed in this chapter in order to ensure DC bus voltage and grid current control in both G2V and V2G modes.

4.3 Bidirectional AC-DC converter control

The control strategy of the PFC Vienna rectifier is an essential part of the EV charger control. The adopted assumption, in order to design the AC-DC converter control, supposes that the voltage at the terminals of each capacitor at the output of the converter is controlled by the DC-DC converter independently, and therefore assumed to be constant and equal to 450 V.
The AC-DC control has “two levels” of complexity. A first level consists in defining the necessary duty cycles for the control of sinusoidal currents based on a specified control law. A second level defines the application of the duty cycle with a proper Pulse Width Modulation (PWM) technique. The AC-DC control strategy with these two levels is detailed in [118].
In this chapter, the aim is to implement the DC-DC LLC converter, studied in chapters 2 and 3, beside the AC-DC converter in order to apply a global control strategy for the entire EV charger. The work will focus, in the next sections, in the comparison of the control performance and efficiency between the DC-DC LLC converter implemented in the EV charger and the DC-DC LLC converter alone.

Concerning the AC-DC converter control, [118] started from a defined averaged model of the PFC Vienna converter. Then, the strategy consists of obtaining the necessary duty cycles for the control of the grid currents at the input of the charger. The switches of each

arm are controlled according to a regulation of the currents at the input of the AC-DC converter generating phase-to-phase target voltages that are to be produced according to setpoint currents.
For confidentiality, the equations of the AC-DC control, that provide the necessary duty cycle based on a grid currents' control, could not be mentionned. They can be found in [118]. The AC-DC control strategy, which can be applied in both G2V and V2G modes, can be illustrated in Figure 4.7 [118].

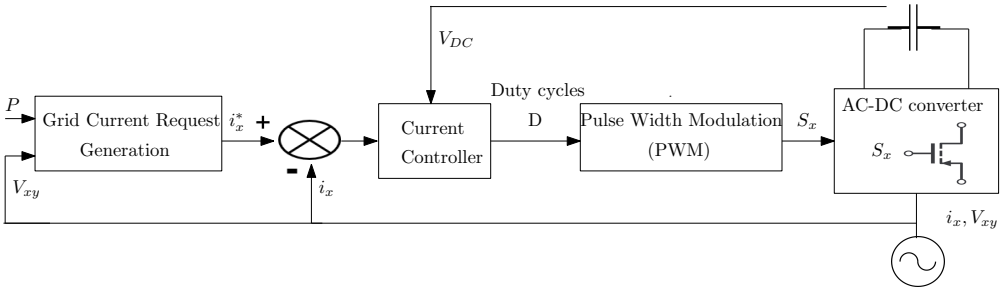

Figure 4.7 – AC-DC converter control strategy

where i_x^* is a phase current setpoint, i_x is a phase current measurement and V_{xy} is a phase-to-phase voltage measurement (x, y present two different phases). The current requests for the AC-DC control strategy are generated based on the phase-to-phase voltage measurements V_{xy} and the charger power request P. The necessary duty cycles D for the control of the sinusoidal grid currents can be obtained from the output of the current regulator as detailed in [118]. The controlled duty cycles are used to generate the MOSFET control signals with a PWM strategy.
In this strategy, it is assumed that the voltage of the DC bus at the output of the PFC AC-DC converter stage is constant, since the LLC DC-DC converter controls it. In the case of an operating point from the saturation zones (Figures 4.5 and 4.6) in both G2V and V2G modes, the switching frequency of the LLC DC-DC converter is saturated causing an important DC bus voltage tracking error which affects the grid current control by the AC-DC converter. Thus, it is crucial to guarantee the DC bus voltage control in order to improve the EV charger control performance for the whole operating zone.

4.4 DC bus voltage control in G2V mode

The new challenge in this section is to provide a hybrid control strategy for the EV charger to regulate the DC bus voltage when the DC-DC LLC converter is saturated in G2V mode (operating point is in the saturation zone i.e. yellow zone in Figure 4.5). Two solutions are proposed in order to avoid the PFM strategy drawbacks with fixed DC bus voltage request.

4.4.1 PFM strategy with variable DC bus voltage request

The large variation in the operating point, i.e. battery voltage and power variation, implies a large variation in the DC-DC LLC converter gain. As presented in Equation 2.15, the switching frequency of the DC-DC LLC converter depends on the LLC parameters, the DC bus voltage and the battery voltage. As the LLC parameters and the battery voltage are constants. Thus, the control strategy proposed in this section consists of varying the DC bus voltage request in order to guarantee the DC bus voltage stability in the saturation zone (the yellow zone in Figure 4.5). The variable DC bus voltage request will ensure the control frequency to be in the feasible zone, unlike the PFM strategy with a fixed DC bus voltage request (450 V). Based on Equation 2.15, it is clearly seen that the feedforward switching frequency f_{0c} is proportional to the DC bus voltage. Knowing that in the G2V saturation zone (the yellow zone in Figure 4.5), f_{0c} is saturated at 200 kHz. Thus, the DC bus voltage request should be decreased less than 450 V in order to enforce f_{0c} to decrease and be in the feasible zone (60-200 kHz). As a result, the DC bus voltage request is changed based on a specified cartography presented in Figure 4.8, which gives the DC bus voltage request in function of the battery voltage.

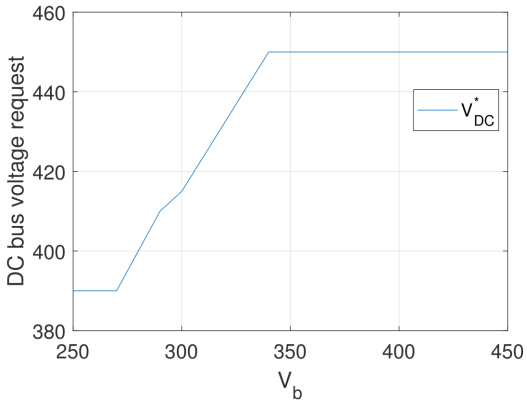

Figure 4.8 – DC bus voltage request in function of the battery voltage

The proposed control strategy is presented in Figure 4.9 in order to obtain the controlled switching frequency f.

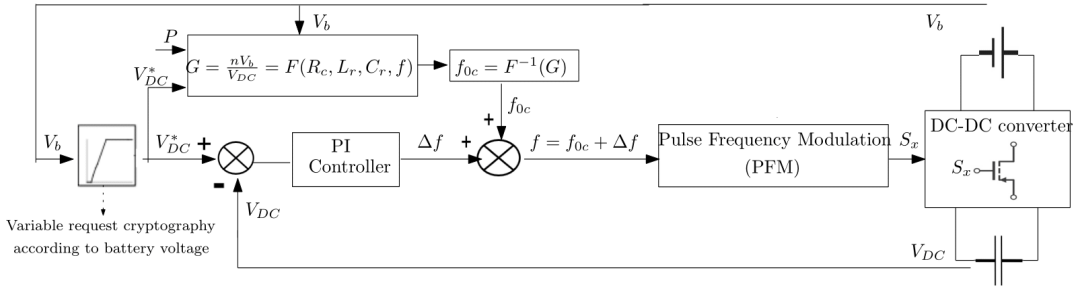

Figure 4.9 – PFM strategy with variable request in G2V mode

This control strategy is based on the GI method presented in chapter 2 for the DC-DC LLC converter in G2V mode (Figure 2.4) but with a variable DC bus voltage request defined in Figure 4.8.
If the operating point is in the saturation zone of G2V mode, the DC bus voltage is regulated using the DC-DC control law with variable DC bus voltage request. Elsewhere, the PFM strategy with constant DC bus voltage request, presented in chapter 2, is still applied. It should be noted that the grid current is always regulated using the the AC-DC control strategy presented in Figure 4.7.

4.4.2 Backstepping control via AC-DC converter

Another solution is provided in this section to ensure the DC bus voltage control when the DC-DC converter is saturated. The key point of the proposed control strategy in this section consists of regulating the DC bus voltage by the help of the AC-DC converter. It should be noted that, in this case, the DC-DC LLC converter is saturated. The proposed control strategy is presented in Figure 4.10.

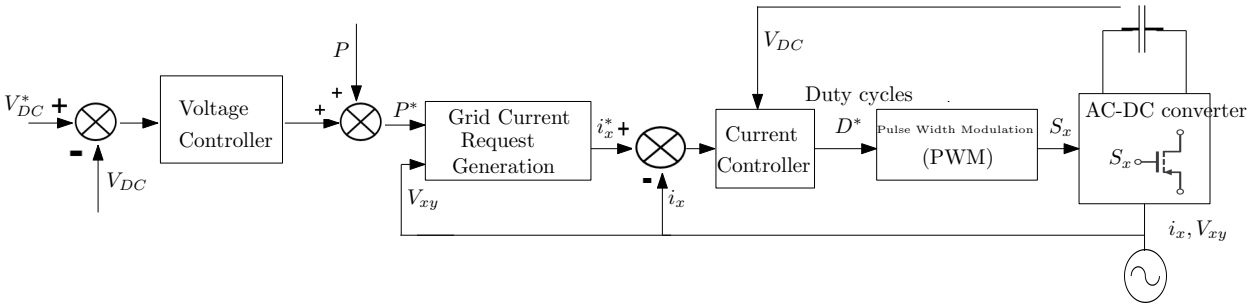

Figure 4.10 – Backstepping AC-DC control strategy in G2V mode

The proposed strategy consists of adding the output of the DC bus voltage controller to the power request in order to provide the corrected power. A new current setpoint i_x^* is generated. The necessary duty cycles D^* to regulate the grid currents can be obtained as presented in section 4.3 based on [118]. Then, the DC bus voltage is controlled via this backstepping duty cycle control. It should be noted that the grid current request variation causes a generation of a corrected power higher than the maximal power request in order to ensure the DC bus voltage control. To avoid this problem, the DC bus voltage request is changed based on the specified cartography presented in Figure 4.8, which gives the DC bus voltage request in function of the battery voltage.

As a result, if the operating point is in the saturation zone of G2V mode, the DC bus voltage and the grid current are controlled using the control strategy proposed in Figure 4.10 with variable DC bus voltage request (Figure 4.8). Elsewhere, the DC bus voltage is controlled using the PFM strategy with fixed DC bus request, and the grid current is controlled using the AC-DC control strategy in Figure 4.7.

4.5 DC bus voltage control in V2G mode

As shown in Figure 4.6, the saturation zone in V2G mode is much important than that in G2V mode (Figure 4.5) when using the PFM strategy.
In chapter 2, modulation strategis, such as PWM and PSM, are implemented for the DC-DC LLC converter alone to ensure the DC bus voltage control and avoid the PFM strategy limitations. The new challenge in this section is to provide a control strategy for the EV charger (including the AC-DC converter) to regulate the DC bus voltage when the DC-DC LLC converter is saturated in V2G mode (operating point is in the saturation zone i.e. yellow zone in Figure 4.6).

4.5.1 PSM strategy

First of all, it should be noted that the DC bus voltage request variation is constrained by the AC phase voltage. The DC bus voltage can vary between a minimal and maximal authorized values and can't exceed this interval in order to ensure the design requirements (thermal constraints). Knowing that in the V2G saturation zone (the yellow zone in Figure 4.6), the feedforward switching frequency f_{0d} is saturated at 200 kHz. Therefore, the DC bus voltage request, like G2V mode, should be decreased less than 450 V in order to enforce f_{0d} to decrease and be in the feasible zone (60-200 kHz). However, as presented in Equation 2.24, f_{0d} is inversly proportional, unlike f_{0c} in G2V mode, to the DC bus voltage. In order to decrease f_{0d} to be in the feasible zone, an important variation of the DC bus voltage request that is larger than the maximal authorized value is required. Thus, it is confirmed that, in V2G mode, the PFM strategy with a variable DC bus voltage request can not be applied to ensure the DC bus voltage control.
In addition, the control strategy by the help of the AC-DC converter, as in G2V mode, can not also be applied because it also requires a larger variation of the DC bus voltage request, in order to keep the corrected power less than the power request, which is not applicable in the case of V2G mode.

In chapter 2, a fixed switching frequency strategy, such as PSM, has been designed for the DC-DC LLC converter alone in order to avoid the PFM strategy limitation in V2G mode. The control law has been implemented based on the GI method.
It has been confirmed, based on chapter 2, that the PSM strategy can be applied, throughout the whole operating zone, to improve the DC-DC LLC converter efficiency and to control the unreachable operating points with the PFM strategy in V2G mode.

In this section, the PSM strategy that has been designed in chapter 2, based on the GI method, is applied for the DC-DC LLC converter to ensure the DC bus voltage control as presented in Figure 4.11.

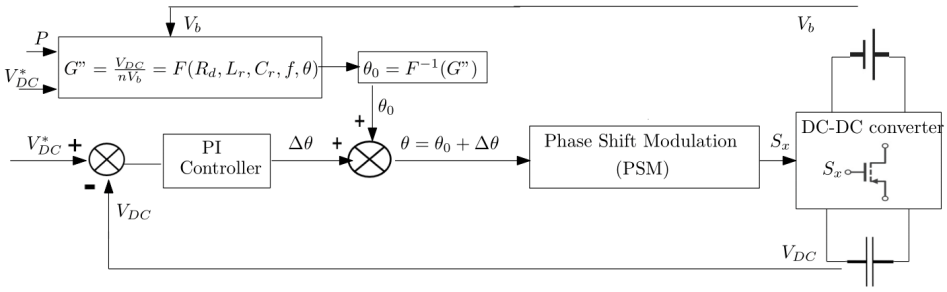

Figure 4.11 – PSM strategy in V2G mode

Compared to chapter 2, the new challenge in this chapter is to implement the control strategy for the entire EV charger including the AC-DC converter. Beside the PSM strategy applied to the DC-DC LLC converter, the grid current is controlled using the AC-DC control strategy in Figure 4.7.
In order to ensure the DC bus voltage control for the whole operating zone in V2G mode, a hybrid control strategy of the EV charger is proposed. In the saturation zone, the PSM strategy is applied to the DC-DC LLC converter. Outside of the saturation zone, the PFM strategy can be used.

4.6 Simulation results

4.6.1 System and simulation configuration

MATLAB/SIMULINK is used to implement the bidirectional EV charger including the AC-DC Vienna converter and DC-DC LLC converter, as well as the control strategy (Discrete solver with fixed step of T_s). Table 4.1 displays the parameter settings. The simulation parameters correspond to a real-world model of the bidirectional EV charger.

$C_f(\mu F)$	75	$L(\mu H)$	60
$C_r(\eta F)$	80	$f_{max}(kHz)$	200
$L_r(\mu H)$	30	$f_{min}(kHz)$	60
$L_m(\mu H)$	120	n	1.6
$\epsilon(V)$	10	T_s	70 ηs

Table 4.1 – AC-DC and DC-DC converters' configuration

The synoptic description of the EV charger model and control system's, which is implemented in Simulink, is presented in Figures 4.12 and 4.13 respectively.

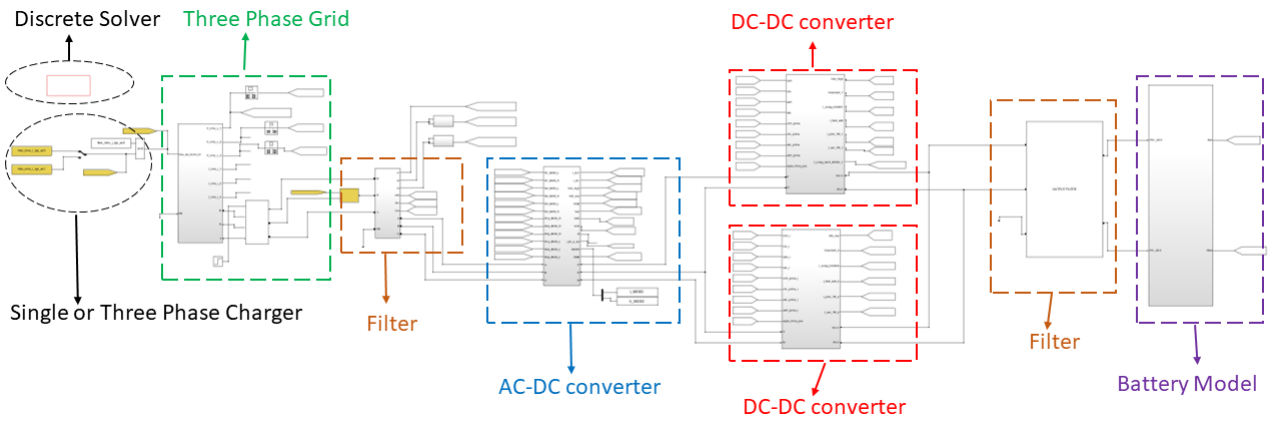

Figure 4.12 – EV charger model synoptic description in Simulink

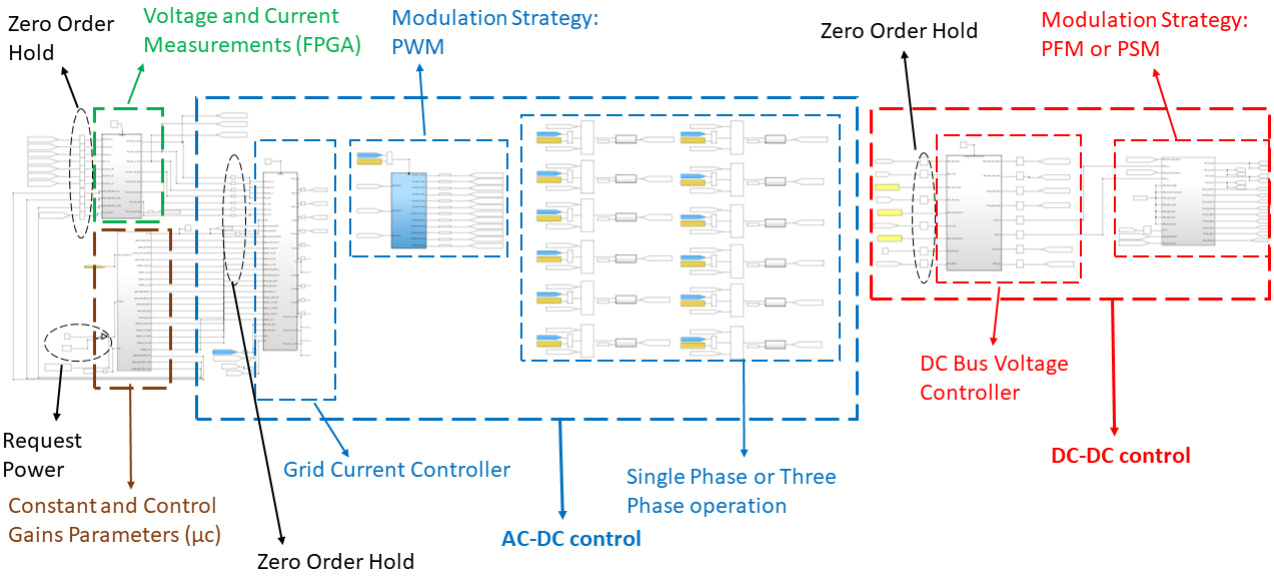

Figure 4.13 – EV charger control synoptic description in Simulink

It worth mentioning that the simulation takes into account the system with the input/output filters (and line impedance) as presented in Figure 4.2. Moreover, it is clearly seen, as illustrated in Figure 4.13, that the voltage and current measurements based on the real EV charger model are used for the control system implementation. Zero-Order Hold (ZOH) blocks are used for signals discretization. The block of measurements operates with the FPGA frequency used in the real EV charger test bench (order of MHz). The control gains and constant parameters are in the same block to be used after by the micro-controller card (μc).

Compared to the DC-DC converter alone, the following results show the advantage of the EV charger control by regulating the DC bus voltage and the grid current with some operating points chosen from the saturation zones in G2V and V2G modes and others chosen outside of the saturation zones.

In G2V mode, the efficiency is computed by dividing the average value of the power from the battery side by the average value of the power from the grid side. In V2G mode, the efficiency is computed by dividing the average value of the power from the grid side by the average value of the battery power. The maximum acceptable voltage tracking error ϵ is 10 V.

4.6.2 G2V mode

The three phase voltages with a peak of 325 V are shown in Figure 4.14 in G2V mode.

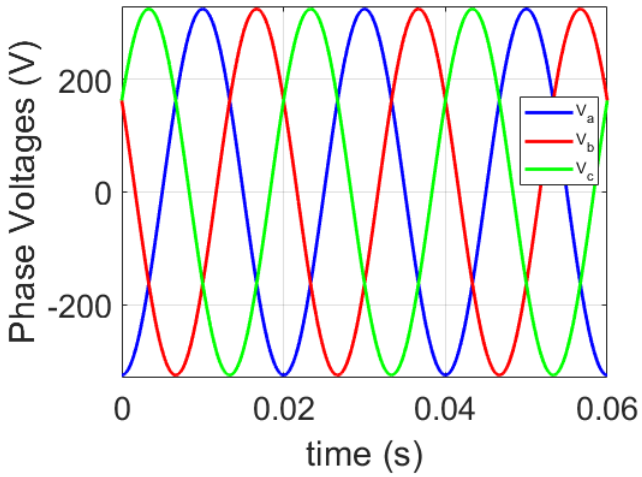

Figure 4.14 – Three phase voltages in G2V mode

Operating point: V_b=290 V and P=2000 W

It should be noted that this operating point is in the saturation zone of the DC-DC converter illustrated in Figure 4.5 where the DC bus voltage control can not be achieved with the PFM strategy with a fixed DC bus voltage request (450 V) applied to the DC-DC converter alone.

PFM with variable DC bus voltage request

The proposed PFM strategy with the variable DC bus request, or simply PFM vr (where vr corresponds to variable request), is applied for this operating point to the EV charger and compared to the PFM strategy with a fixed DC bus request (450 V) applied to the DC-DC converter alone. With the proposed strategy, the DC bus voltage request V^*_{DC} is then defined based on the cryptography in Figure 4.8, which gives 410 V for V_b=290 V. It is clearly seen, as shown in Figure 4.15, that the DC bus voltage converges to the setpoint with a settling time of 0.002 s. The maximal voltage tracking error with PFM vr is 5 V for V^*_{DC}=410 V, which is much lower than that with the PFM applied to the DC-DC converter (15 V) for V^*_{DC}=450 V.

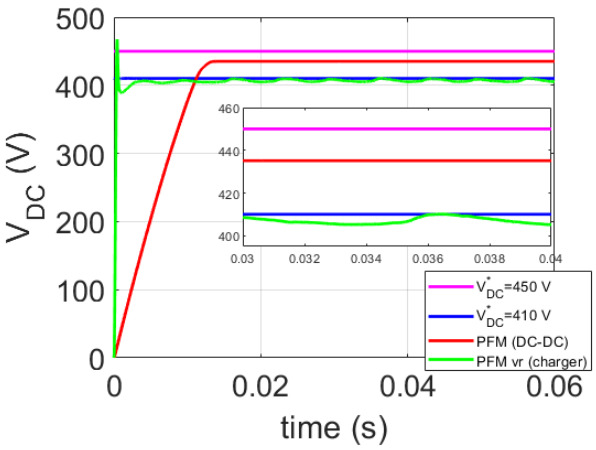

Figure 4.15 – DC bus voltage responses in G2V mode for V_b=290 V and P=2000 W

In Figure 4.16, it can be observed that the switching frequency f using PFM vr is inside the feasible zone with a feedforward frequency f_{0c} (PFM vr) of 124 kHz according to the new voltage request. In contrast, using the PFM strategy with the fixed request (450 V), it can be seen that f_{0c} (PFM) is 220 kHz, out of the feasible zone, providing a switching frequency saturated at 200 kHz and a loss of the DC bus voltage control.

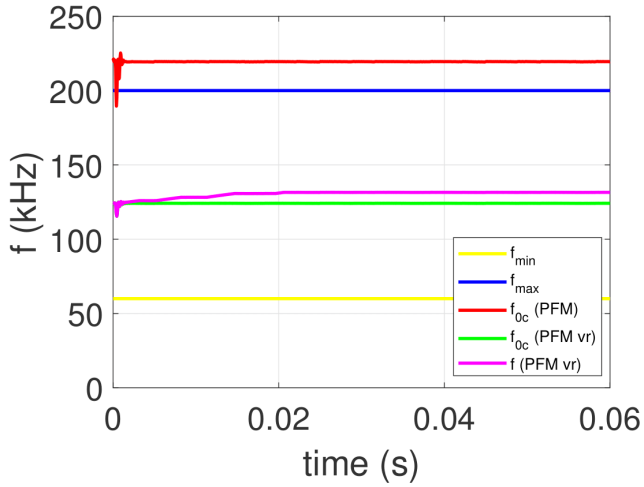

Figure 4.16 – Switching frequencies in G2V mode for V_b=290 V and P=2000 W

Figure 4.17 presents phase currents. The phase currents are regulated by the AC-DC converter with the proposed EV charger control, which follow the current setpoints with a maximal current tracking error of 1 A. The control strategy based on PFM vr presents an improved efficiency of 75%, whereas that based on the PFM strategy of the DC-DC converter presents an efficiency of 69% with an important DC bus voltage tracking error.

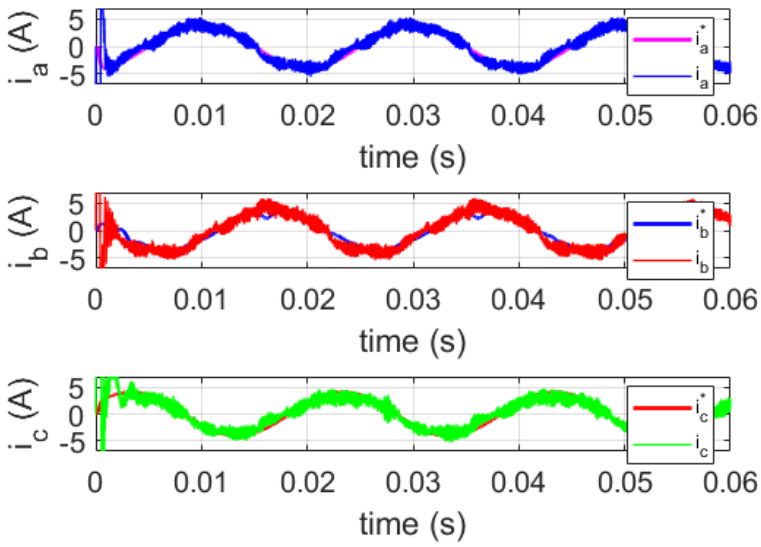

Figure 4.17 – Phase currents with PFM vr in G2V mode for V_b=290 V and P=2000 W

Backstepping control by the help of the AC-DC converter (or AC-DC control)

With this proposed strategy, the AC-DC converter is the responsible to ensure DC bus voltage as well as grid current control. The DC bus voltage controller is added to the power request in order to generate the grid current request for the grid current controller. The DC bus voltage request $V_{DC}^{\star}$ is always defined based on the cryptography in Figure 4.8, which gives 410 V for V_b=290 V. The DC bus voltage response with the AC-DC control is illustrated in Figure 4.18 and compared to that with the PFM strategy in case of the DC-DC converter. The corrected power (P_{corr}) resulting from the sum of the power request (P_{req}) and the DC bus voltage controller output is shown in Figure 4.19. The phase currents, converging to setpoints, and phase current errors are shown in Figures 4.20 and 4.21 respectively.

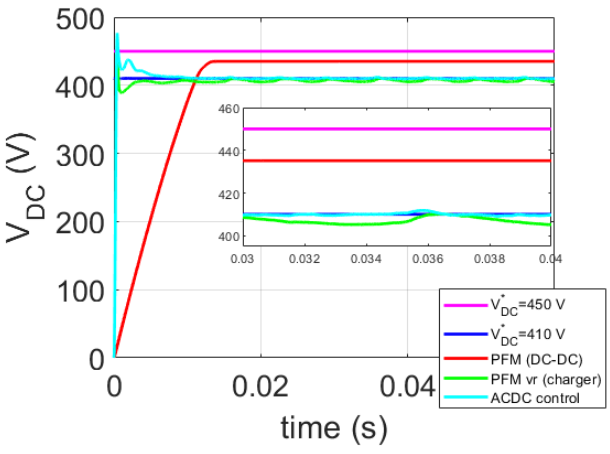

Figure 4.18 – DC bus voltage with the AC-DC backstepping control in G2V mode for V_b=290 V and P=2000 W

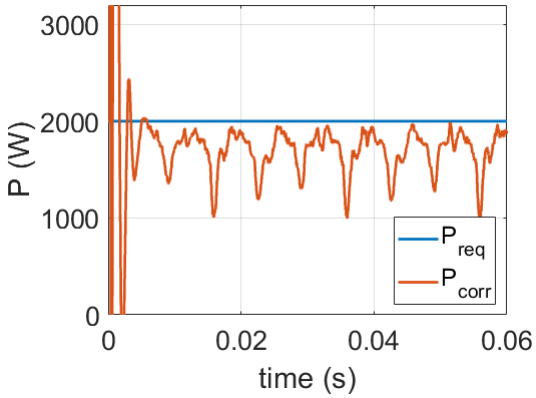

Figure 4.19 – Corrected power with the AC-DC backstepping control in G2V mode for V_b=290 V and P=2000 W

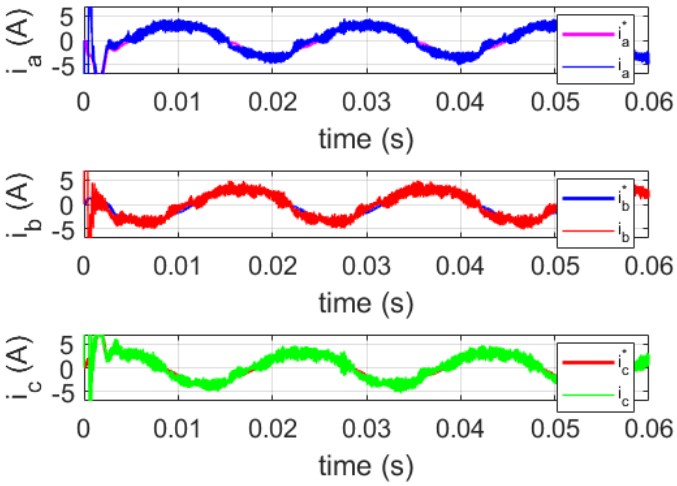

Figure 4.20 – Phase currents with the the AC-DC backstepping control in G2V mode for V_b=290 V and P=2000 W

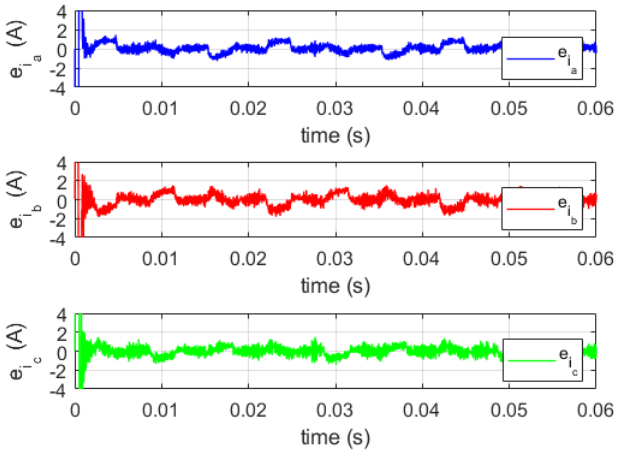

Figure 4.21 – Phase current errors with the the AC-DC backstepping control in G2V mode for V_b=290 V and P=2000 W

The AC-DC control can improve the DC bus voltage control performance. However, it presents an efficiency of 47% due to the decrease in the power that can reach 1000 W resulting from the addition of the control action. On the other hand, even if the PFM strategy applied to the DC-DC converter presents a higher efficiency of 69% but it suffers from an important DC bus voltage tracking error.

Comparison

In this paragraph, a comparative study between the control strategies applied to the EV charger, such as PFM vr and the AC-DC control, and the PFM strategy applied to the DC-DC converter is summarized in the table of Figure 4.22.

G2V V_b=290 V, P=2000 W	$\lvert e_{V_{DC}-max} \rvert$ (V)	Overshoot (%)	t_s(s)	$\lvert e_{i_a-max} \rvert$ (A)	Efficiency (%)
PFM (DC-DC)	15	/	/	/	69
PFM vr (charger)	5	13	0.002	1	75
AC-DC control (charger)	2	15	0.002	1	50

Figure 4.22 – Comparison table in G2V mode for V_b=290 V and P=2000 W

Operating point: V_b=420 V and P=10000 W

It should be noted that this operating point is outside of the saturation zone of the DC-DC converter illustrated in Figure 4.5 where the DC bus voltage control can be achieved with the PFM with fixed DC bus voltage request (450 V).
It is clearly seen, as shown in Figure 4.23, that the DC bus voltage converges to the setpoint with a settling time of 0.01 s. The maximal voltage tracking error is 5 V for V_{DC}^{*}=450 V. The switching frequency, phase currents, and phase current errors are shown in Figures 4.24, 4.25 and 4.26 respectively.

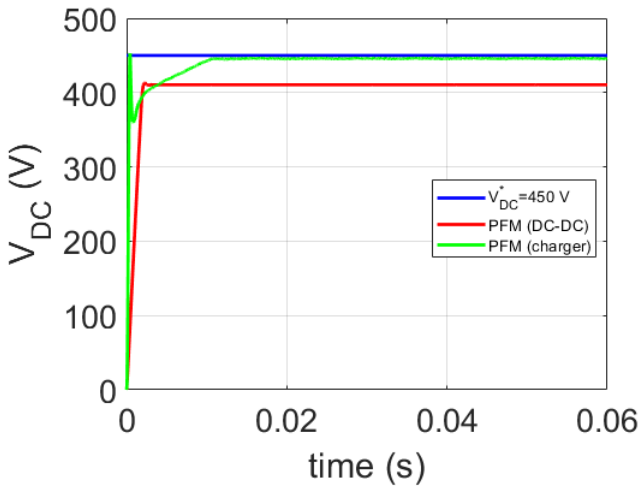

Figure 4.23 – DC bus voltage responses in G2V mode for V_b=420 V and P=10000 W

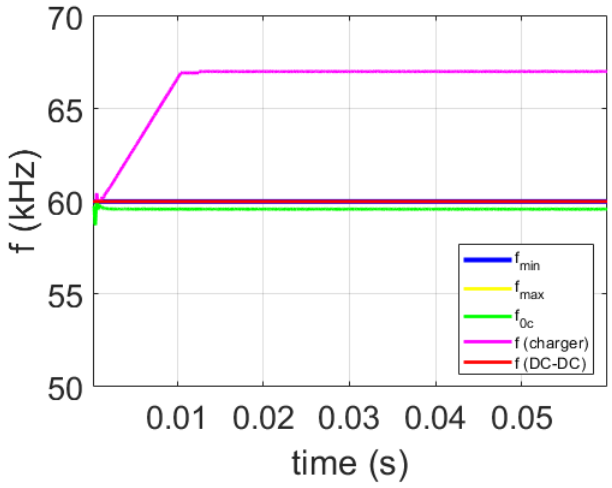

Figure 4.24 – Switching frequencies in G2V mode for V_b=420 V and P=10000 W

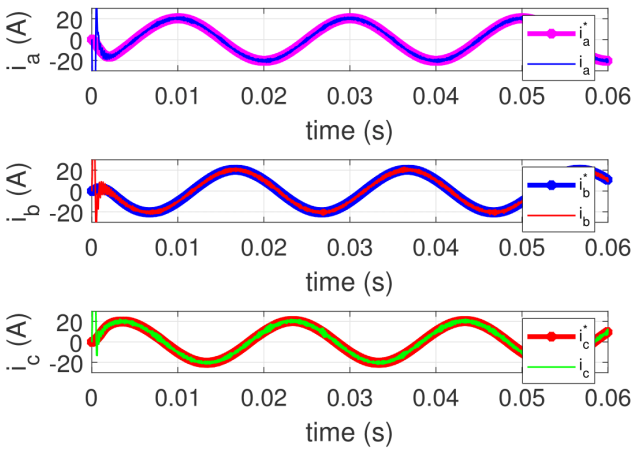

Figure 4.25 – Phase currents with PFM in G2V mode for V_b=420 V and P=10000 W

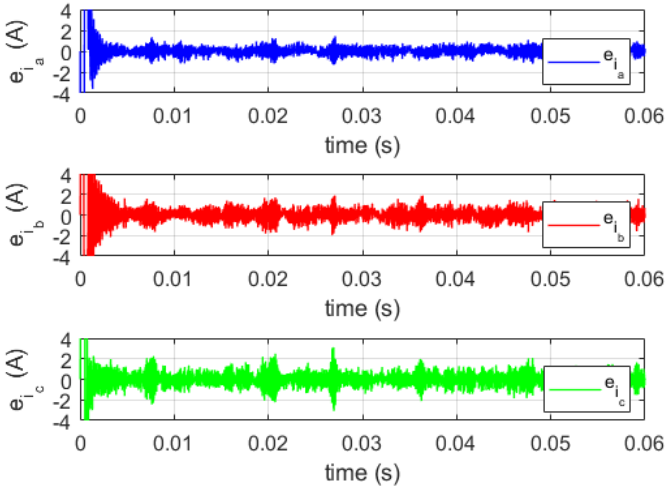

Figure 4.26 – Phase current errors with PFM in G2V mode for V_b=420 V and P=10000 W

Based on Figure 4.24, it can be observed that the switching frequency f, with the EV charger control, increases from f_{0c} (60 kHz) to be inside the feasible zone, whereas in case of the DC-DC converter f is saturated at 60 kHz. A comparison table is shown in Figure 4.27.

G2V V_b=420 V, P=10000 W	$\lvert e_{V_{DC}-max} \rvert$ (V)	Overshoot (%)	t_s(s)	$\lvert e_{i_a-max} \rvert$ (A)	Efficiency (%)
PFM (DC-DC)	40	/	/	/	84
PFM (charger)	5	0	0.01	1	81

Figure 4.27 – Comparison table in G2V mode for V_b=420 V and P=10000 W

The EV charger control presents an efficiency of 81% with a good control performance in terms of the DC bus voltage and grid cuurent control. In contrast, the DC-DC converter which presents an important voltage tracking error even with a higher efficiency.

4.6.3 V2G mode

The three phase voltages with a peak of 325 V are shown in Figure 4.28 in V2G mode.

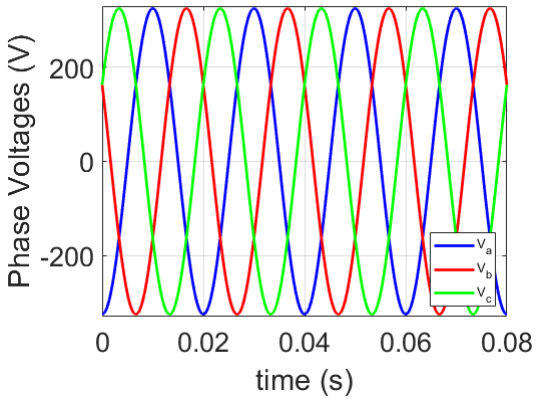

Figure 4.28 – Three phase voltages in V2G mode

It should be noted that the power request of the EV charger is delivered to the AC-DC converter. The AC-DC converter is connected to two DC-DC converters. Each DC-DC converter is responsible to transfer half of the charger power. The maximal charger power related to this topology is 22000 W (in three-phase system) which explains that the DC-DC converter power can reach a maximum of 11000 W.

Operating point: V_b=430 V and P=4000 W

This operating point is in the saturation zone of the DC-DC converter illustrated in Figure 4.6 (P=2000 W for each DC-DC LLC converter).

PSM

The PSM strategy is applied to the DC-DC LLC converter alone in chapter 2. In this chapter, the proposed EV charger control strategy consists of implementing the PSM strategy for the DC-DC LLC converter in order to ensure the DC bus voltage control when the DC-DC is saturated in V2G mode. The AC-DC converter is used to ensure the grid current control.

For the following simulation results, the switching frequency of the DC-DC LLC converter is fixed at 200 kHz. The DC bus request (V^*_{DC}) is fixed at 450 V.

Figure 4.29 shows the DC bus voltage response with the proposed EV charger control, based on the PSM strategy, converging to the setpoint, with a settling time of 0.01 s and a maximal voltage tracking error of 5 V.

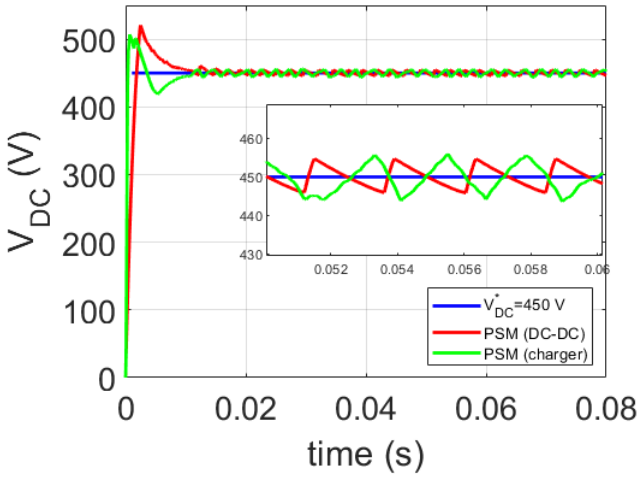

Figure 4.29 – DC bus voltage responses with PSM in V2G mode for V_b=430 V and P=4000 W

Figure 4.30 presents the controlled phase shift angles with the PSM strategy in case of the DC-DC converter and the EV charger. In Figures 4.31 and 4.32, phase currents and phase current errors are shown. The phase cuurents converge to the current setpoints with maximal current tracking error of 3 A, with the proposed EV charger control.

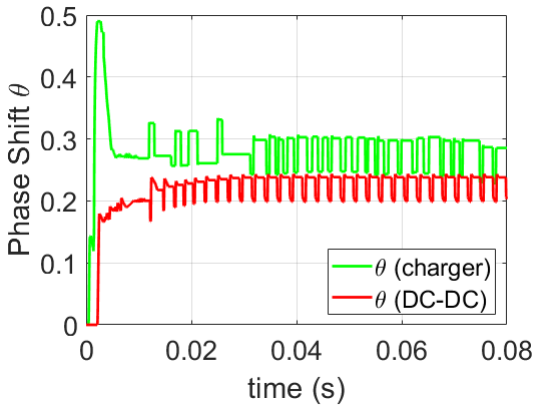

Figure 4.30 – Phase shift angles with PSM in V2G mode for V_b=430 V and P=4000 W

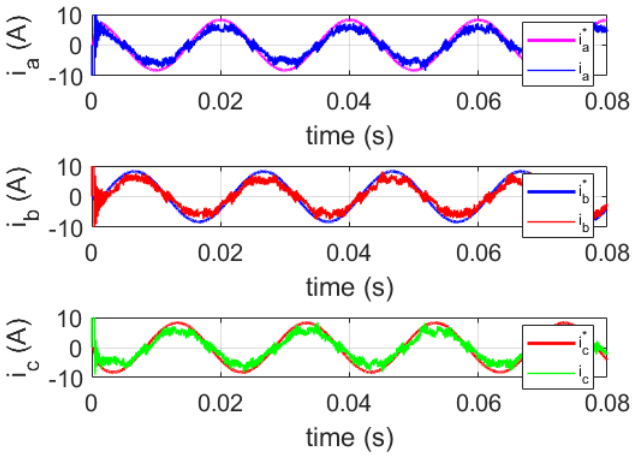

Figure 4.31 – Phase currents with PSM in V2G mode for V_b=430 V and P=4000 W

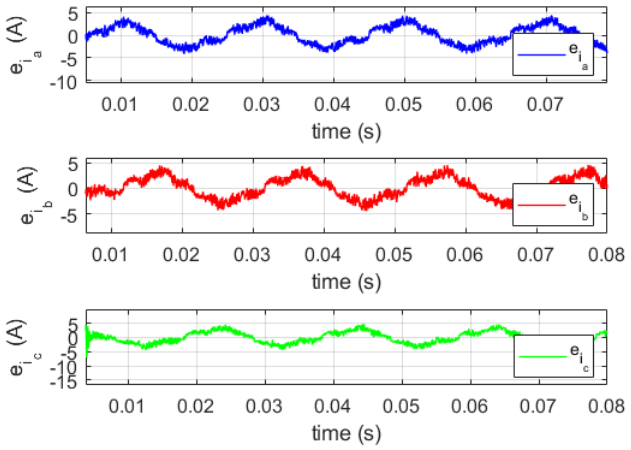

Figure 4.32 – Phase current errors with PSM in V2G mode for V_b=430 V and P=4000 W

Furthermore, the efficiency of the EV charger with the proposed control strategy based on the PSM strategy is 84,2 % which is much better than that with the PSM strategy of the DC-DC converter (76 %).
A table that summarizes the comparison is shown in Figure 4.33.

V2G V_b=430 V, P=4000 W	$\lvert e_{V_{DC}-max} \rvert$ (V)	Overshoot (%)	t_s(s)	$\lvert e_{i_a-max} \rvert$ (A)	Efficiency (%)
PSM (DC-DC)	5	15.5	0.014	/	76
PSM (charger)	5	12.6	0.01	3	84.2

Figure 4.33 – Comparison table in V2G mode for V_b=430 V and P=4000 W

Operating point: V_b=380 V and P=20000 W

This operating point is outside of the saturation zone of the DC-DC converter illustrated in Figure 4.6 where the DC bus voltage control can be achieved with the PFM

strategy.

It is clearly seen, as shown in Figure 4.34, that in both cases, the DC bus voltage converges to the setpoint. The EV charger control presents a higher voltage tracking error (7 V) but it is still acceptable ($\leq \epsilon$).

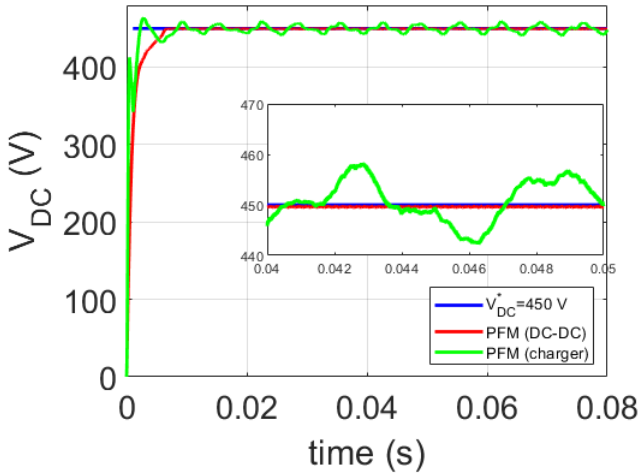

Figure 4.34 – DC bus voltage responses in V2G mode for V_b=380 V and P=20000 W

The switching frequency, phase currents and phase current errors are shown in Figures 4.35, 4.36 and 4.37 respectively. It can be observed that the switching frequency f is inside the feasible zone, in both cases, with a feedforward frequency f_{0d} of 152 kHz. The EV charger with this control strategy presents an efficiency of 97,5% higher than that of the DC-DC converter (91,5 %).

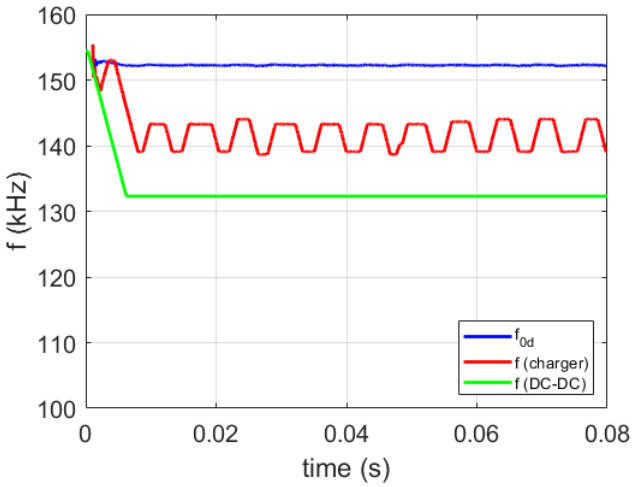

Figure 4.35 – Switching frequencies with PFM in V2G mode for V_b=380 V and P=20000 W

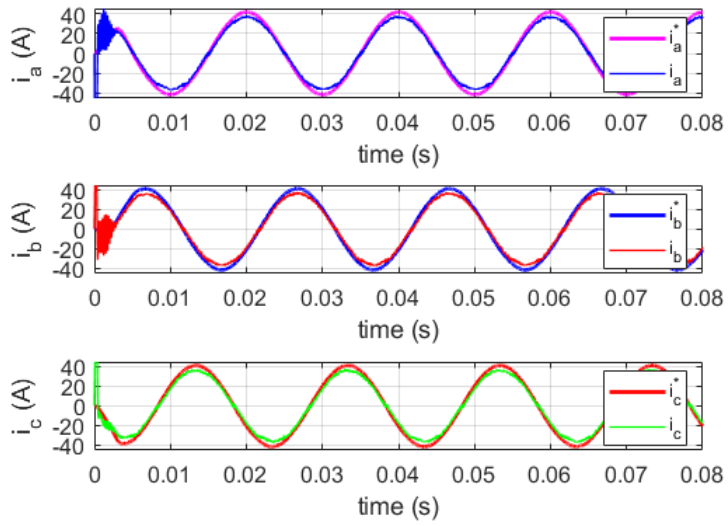

Figure 4.36 – Phase currents with PFM in V2G mode for V_b=380 V and P=20000 W

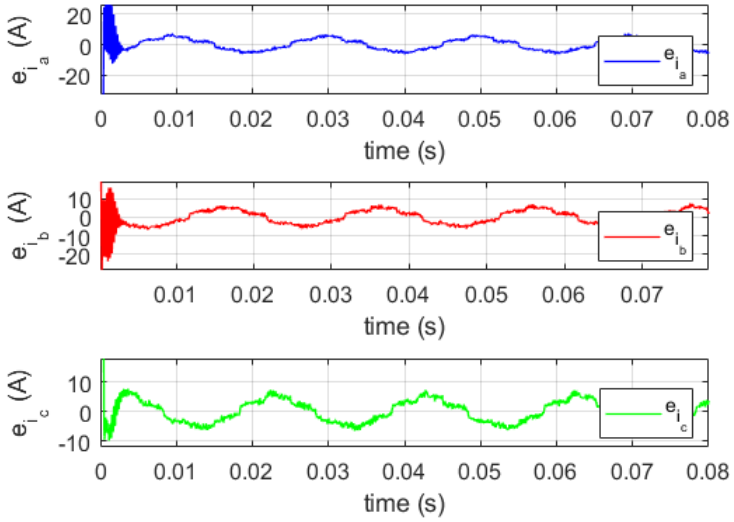

Figure 4.37 – Phase current errors with PFM in V2G mode for V_b=380 V and P=20000 W

As a summary, a comparison table is shown in Figure 4.38.

V2G V_b=380 V, P=20000 W	$\lvert e_{V_{DC}-max} \rvert$ (V)	Overshoot (%)	t_s(s)	$\lvert e_{i_a-max} \rvert$ (A)	Efficiency (%)
PFM (DC-DC)	0.5	0	0.007	/	91.5
PFM (charger)	7	2	0.008	5	97.5

Figure 4.38 – Comparison table in V2G mode for V_b=380 V and P=20000 W

4.7 Conclusion

The OnBoard EV charger is one of the most interesting elements for EV manufacturers. The bidirectional charger should be able to transfer power in both G2V and V2G modes with a high performance and efficiency. In this chapter, the bidirectional charger structure is of an AC-DC converter based on Vienna topology connected to two DC-DC LLC converters. The DC-DC LLC converter is studied in chapters 2 and 3. The AC-DC converter is used to ensure the grid current control via a PWM strategy. Usually, the role of the DC-DC LLC converter is to ensure the DC bus voltage stability via a PFM strategy. However, when PFM is adopted for a wide operating zone in both G2V and V2G modes, the DC-DC LLC converter is saturated causing an important DC bus voltage tracking error and low efficiency.

The new challenge of this chapter is to provide a bidirectional charger control, comprising bidirectional AC-DC converter and DC-DC converter control strategies, that aims to guarantee the DC bus voltage control and improve the grid current control performance when the DC-DC converter is saturated. The main contribution is to cover the whole operating zone of the bidirectional EV charger.

The method comprises a step to determine the operating zone of the bidirectional DC-DC converter, chosen from a saturated zone and an unsaturated zone, according to the operation mode of the charger (G2V or V2G), and to the battery voltage and power request.

In G2V mode, two solutions are discovered and implemented. On the one hand, the PFM strategy, based on the GI method presented in chapter 2, with variable DC bus request is implemented for the DC-DC LLC converter when the operating point is in the saturation zone. On the other hand, a backstepping control strategy by the help of the AC-DC converter is proposed to overcome the DC-DC converter limitation. The output of the DC bus voltage controller is added to the power request in order to provide a power correction.

In V2G mode, the PSM strategy with a fixed switching frequency, presented in chapter 2, is implemented for the DC-DC LLC converter in order to overcome the PFM strategy limitation when the DC-DC LLC converter is saturated.

Outside of the saturation zones, the PFM strategy with a fixed DC bus voltage request is implemented in both G2V and V2G modes.

In both G2V and V2G modes, the currents grid are controlled by the AC-DC converter.

Compared to the DC-DC LLC converter alone, the results show the effectiveness of the proposed hybrid control strategy of the EV chargerin both G2V and V2G modes. The advantages include the guarantee of the DC bus voltage control for the whole operating zone as well as the improvement of the grid currents' control performance and of the bidirectional EV charger efficiency.

5

Bidirectional DAB Charger Control

5.1 Introduction

There are different topologies of bidirectional DC-DC converters that can be used for high power applications such as bidirectional EV charger. This chapter mainly focuses on the Dual Active Bridge (DAB) converter. This topology has not been scheduled from the beginning of the thesis because the work focused on the EV charger including the LLC resonant converter studied in previous chapters. However, based on the industrial collaboration with Renault, the DAB charger is studied. The benefit for the manufacturer of using the DAB charger arises from the fact the DAB converter uses less passive components than other isolated converters like SRC, CLLC and LLC that use auxiliary inductors and capacitors. This makes the charger smaller in size, less expensive, less in space, and easier in control design with high power density and high efficiency.

Different modulation strategies, such as Single Phase Shift (SPS), Dual Phase Shift (DPS) or Trapezoidal Modulation (TZM) have been implemented to improve the feasibility zone of the DAB converter. The main concept of the adopted modulation strategies consists in varying either duty cycles or phase shift angles of the MOSFETs' signals with a fixed switching frequency.

In this chapter, a bidirectional single-phase charger with a maximal power of 7,4 kW and a battery voltage variation between 300 and 430 V in both G2V and V2G is studied. The objective is to develop a control strategy of the DAB charger in order to improve the control performance and the charger efficiency in both G2V and V2G modes. Each modulation startegy applied to the DAB converter has some advantages and drawbacks. The aim is to apply different modulation strategies, such as SPS and DPS, to the DAB converter in the EV charger application combined with a specific control algorithm.

The contributions can be summarized as follows:

- Design of a control strategy for the DAB charger in order to ensure the control of the AC grid current and DC bus voltage
- Implementation of different modulation strategies, such as SPS and DPS modulations, based on an averaged model of the DAB converter
- Comparative study of the modulation strategies in terms of the control performance and charger efficiency
- Covering the whole operating zone of the EV charger in both G2V and V2G modes

5.2 Literature study on control of DAB converters

The choice of the DAB topology as a DC-DC converter is justified in detail in [119]. It is inherently symmetric compared to resonant tank topologies and uses less passive components thereby potentially increasing the power density. It is normally operated at fixed switching frequency, which is an advantage compared to resonant topologies, which are mostly operated with varying switching frequency, thereby leading to avoid EMI filters. The DAB control is a topic much discussed in the literature because of its importance. Different control strategies have been proposed to guarantee the correct functioning of the DAB.

The following are common objectives outlined in all state of the art of DAB technologies: a relatively simple control method may accomplish a wide ZVS range, low peak inductor current and low Root Mean Square (RMS) current of the transformer leaking inductor. Many modulation techniques such as SPS, DPS, TZM and Extended Phase Shift (EPS) are applied for the DAB converter.

The control strategy proposed in [120] consists of regulating the output voltage through a PI controller by comparing it with a voltage reference. The output of the corrector will be compared with the average value of the measured current of the high frequency transformer and corrected afterwards with a classic PI corrector. The output of the corrector is used to calculate a phase shift which will be the input of the modulation block.

In [121], the efficiency of each type of modulation technique is simulated across various power levels. The three different modulation studied here are the common SPS, DPS and EPS. Furthermore, it proposes an integration of these techniques to achieve high overall gain of the converter. For different operating points, it monitors the inductor current to be least while meeting the conditions of ZVS for efficient performance of the power transfer.

A new approach in [122] focusing on the control of charging current and voltage is proposed as a primary objective rather than power flow control between primary and secondary sides of a DAB converter. In the charging mode, primary side H-bridge is switched using fixed frequency and fixed duty cycle of 50%, and the secondary H-bridge is switched as

a controlled rectifier to regulate the desired output. The actual battery charging current or voltage is compared to a given reference value and depending on the error, the duty cycle is incremented/decremented by a small value to reduce the error. In the discharging mode, the secondary side inverts battery voltage to a rectangular AC voltage at fixed frequency using duty cycle of 50%. On the primary side, switching pulses are generated to rectify this AC voltage to the required DC level. The actual voltage across load is compared with a given reference value and the duty cycle is incremented/decremented by a small value to reduce the error like the charging mode.

Given the shortcomings of the conventional SPS control at light and medium power levels, [123] further analysis the potential use of DPS and Triple-Phase-Shift (TPS). Although DPS and TPS can be the answer, they do introduce side effects such as larger switching-OFF current. This article systematically integrates SPS, DPS, and TPS to maximize the full-power ZVS range for both steady state and transient operations in EV chargers. Moreover, this article plots ZVS boundaries over the full power range and proposes a smooth transition method among all operation modes.

In order to improve the DAB converter efficiency, multi-phase modulations have been proposed. However, the control design becomes more complex. The paper [124] presents two-stage modulations based on the SPS modulation, keeping the simplicity of the design and implementation and improving the DAB converter efficiency.

In the paper [125], an unified boundary TZM control utilizing fixed duty cycle compensation and magnetizing current design for a DAB converter is proposed. The TZM can make the active bridge work with large duty cycles and result in lower peak inductor current and RMS value. Meanwhile, compared to the conventional SPS, DPS and EPS, non-active current is avoided. Besides, the ZVS of four power switches cannot be achieved since the transformer leakage current maintains zero when the power switches are turned OFF.

Thanks to the hybrid mode modulation method that was developed in [126], the DAB converter was able to operate in an extremely wide voltage range with enhanced overall efficiency and a quick transient response.

In [127], researchers achieved high performance using DPS control strategy to reduce by 50% current stress when the load power is low compared to that of SPS with wide range of input and output voltages.

To summarize, to the best of our knoweldge, most existing work in the literature focused on the design, implementation and comparison of different modulation strategies (SPS, DPS, EPS and TZM) for the DAB converter alone [124, 127] or as a part of an EV charger [119] in an open loop without a phase shift control law and with a narrow power range (0-3 kW). Besides, the existing work, which includes a closed loop phase shift control law, aimed to regulate the battery voltage or current [120, 123, 125, 126], without any power factor correction in case of an EV charger [123].

However, the main contribution of this chapter compared to what existing in the litera-

ture, is to design a closed loop control strategy, combined with the common modulation strategies SPS and DPS, for the DAB converter implemented in a single phase bidirectional EV charger. The new challenge is to regulate the DC bus voltage and ensure the grid current control by the phase shift control of the DAB converter. The output voltage, i.e. the battery voltage, varies between 300 and 430 V and the power varies between 0 and 7,4 kW. The aim consists of covering the entire operating zone of the charger in both G2V and V2G modes with the proposed DAB control strategy.

5.3 Problem statement

This chapter studies a DAB circuit which is a part of an OnBoard EV charger. The topology of the studied single phase charger is presented in Figure 5.1.

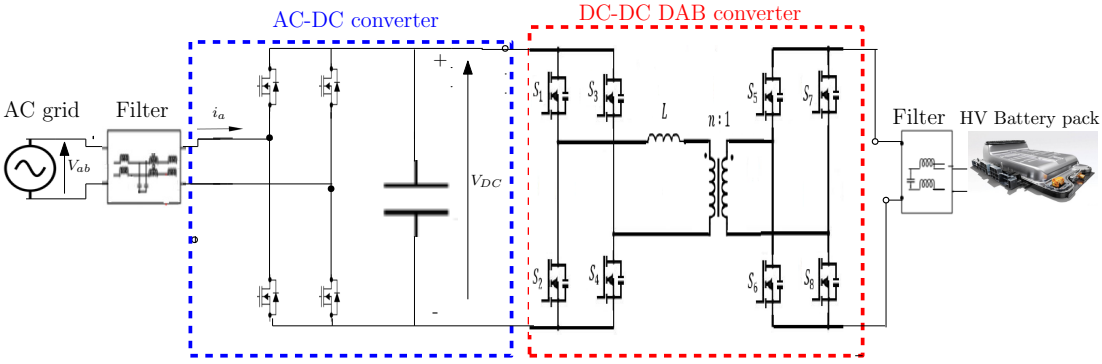

Figure 5.1 – Single phase EV charger using DAB converter

The main advantages of this topology compared to traditional topologies (PFC + isolated DC-DC converter) are:

- Two-stage structure of High Frequency (HF) conversion (compared to three stages for conventional topologies)
- Little capacitive storage on the DC bus and less passive components (less cost)
- Smaller input AC filter

Despite the simple design and implementation, the main drawback of the DAB topology is the limited voltage operation range with the phase shift control. As output or input voltages move away from the nominal operation, a large circulating energy arises between the bridges, conduction losses rise, and the soft-switching range is reduced, leading to a significant reduction in efficiency [128]. Therefore, the resonant topologies, such as the LLC topology studied in the last chapters 2, 3 and 4, are proposed to provide reduced peak currents, higher efficiency, and improved soft-switching range.
Actually, the DAB converter uses the energy that is stored in its inductor L (which, in some designs, may be the transformer's leakage inductance) to accomplish ZVS. Since the load current is the only factor affecting this energy, ZVS can be lost under a specific load depending on the value of L. In contrast, the DC-DC LLC converter achieves ZVS by

using the energy stored in the magnetizing inductance of its transformer. Therefore, once the magnetizing inductance is established to achieve ZVS at a certain output voltage, it is maintained for all loads [128].
Thus, a tradeoff, as presented in the comparison of DC-DC topologies in chapter 1, between control, design, efficiency requirements, and the cost should be taken into account in order to define the charger topology.

Based on Figure 5.1, the charger is divided into two essential parts: a rectifier and an isolated DAB converter. The purpose of the AC-DC converter is to rectify the grid voltage to obtain a rectified sine type voltage at the input of the next stage (DC-DC converter). The grid current is i_a and the grid voltage is V_{ab}. The DAB converter is the responsible to ensure the stability of the grid and the DC bus via the proposed control strategy.
An equivalent circuit for the DC-DC DAB converter is presented in Figure 5.2.

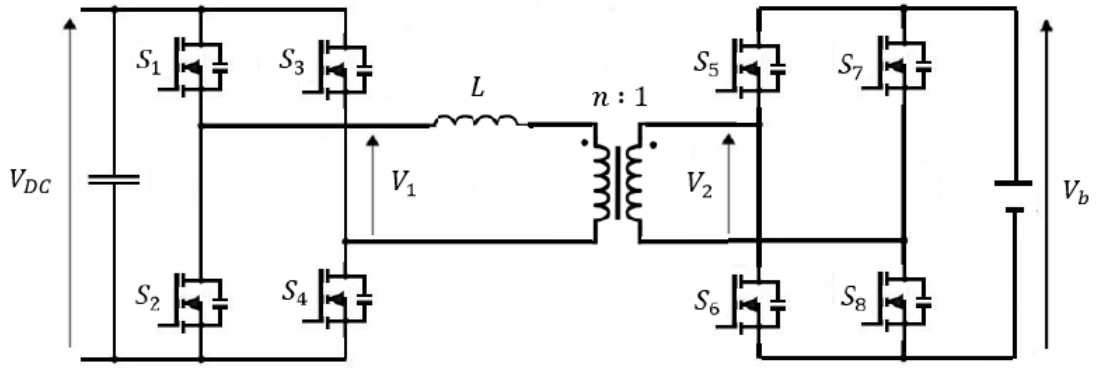

Figure 5.2 – DAB converter structure

According to Figure 5.2, the single-phase DAB converter is made up of two H-bridges coupled by a HF AC transformer with a turns ratio of n. V_{DC} is the DC bus voltage, while V_b is the battery voltage. The AC voltages at the primary and secondary sides of the transformer are V_1 and V_2 respectively. L is the DAB inductor which serves as the energy transfer element. The difference between the AC voltages of the input and output bridges, or V_1 and V_2 respectively, drives the current which flows in the inductor L.
The HF transformer can achieve the galvanic isolation which increases the protection and guarantees that charging regulations are met in high voltage applications like EV chargers. The full bridge on the left side in Figure 5.2 is connected to the High Voltage (HV) DC bus (Output of the previous stage (rectifier)) and the full bridge on the right side is connected to the battery.

5.4 Modulation strategies

The DAB converter, in contrast to many bidirectional isolated DC-DC converters with asymmetrical topologies, features two symmetrical full bridges that produce phase-

shifted square waves for the primary and secondary sides of the transformer. To control the power flow direction and magnitude, the associated phase shift modifies the voltage across the transformer leakage inductor, which serves as the energy transfer component. The principle of two different modulation strategies, such as SPS and DPS, is discussed in this section with their advantages and drawbacks.

5.4.1 Single Phase Shift (SPS) modulation

The popular modulation technique in the DAB converter is known as SPS modulation, where the phase shift angle between the primary side full bridge and the secondary side full bridge controls the power flow. The voltage or current can be stabilized and regulated by adjusting this phase shift angle. The main waveforms under SPS modulation are shown in Figure 5.3 in G2V for a boost mode [3] .

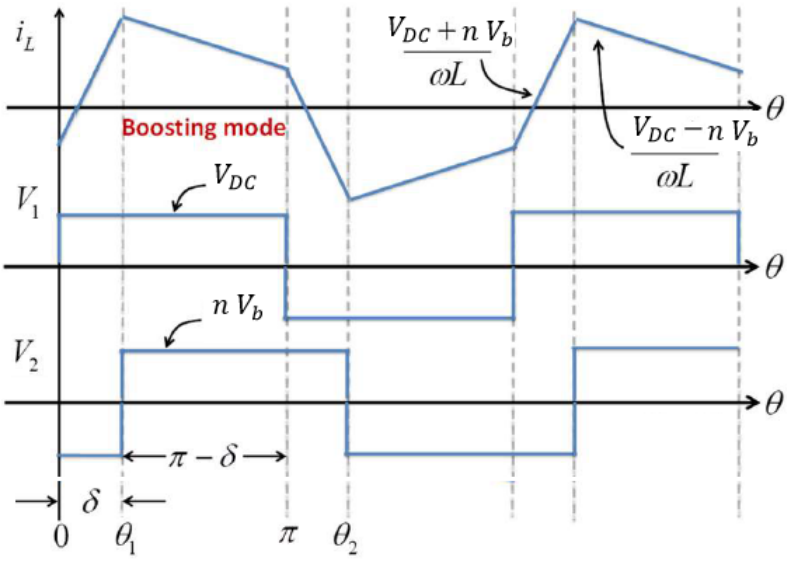

Figure 5.3 – SPS modulation waveforms in G2V mode (for a boost mode) [3]

Figure 5.3 represents the shape of the voltage waves at the primary (V_1) and secondary (V_2) of the transformer as well as the shape of the current (i_L) flowing in the inductor L in G2V mode for a boost mode (V_{DC} is lower than $n\,V_b$). Note that there are two voltage levels that either at the primary side or at the secondary side of the transformer.
For SPS modulation, the phase shift δ is adjusted between the voltages V_1 and V_2 in such a way that δ belongs to the interval $[0;\pi]$.
The expression of the mean value of the power flow (in G2V mode) in a half period is defined by Equation(5.1):

$$P = \frac{1}{\pi}\int_0^{\pi} V_{DC}\, i_L d\theta \tag{5.1}$$

For the SPS modulation, the power flux expression is defined by Equation(5.2) [129]:

$$P = V_{DC}\,\overline{i_L} = \frac{V_{DC}\,n\,V_b}{2\pi f_s L}\delta\left(1-\frac{\delta}{\pi}\right) \tag{5.2}$$

where V_{DC} and $n\,V_b$ are the maximum values of V_1 and V_2 respectively, L is the inductance, f_s is the switching frequency ($w = 2\pi f_s$) and $\overline{i_L}$ is the average value of the current i_L. The goal is to have an expression linking the phase shift and the mean value of the inductor current i_L in order to obtain the phase shift for the SPS modulation. By identification between Equations (5.1) and (5.2), this link can be obtain. Thus, by dividing Equation(5.2) by the value of the DC bus voltage V_{DC}, $\overline{i_L}$ can be obtained in G2V mode as in Equation(5.3):

$$\overline{i_L} = \frac{P}{V_{DC}} = \frac{n\,V_b}{2\pi f_s L}\delta(1 - \frac{\delta}{\pi}) \tag{5.3}$$

Consequently, based on Equation(5.3), the following Equation(5.4) which allows to obtain the phase shift δ can be defined:

$$\delta^2 - \pi\delta + \frac{2\pi^2 f_s L \overline{i_L}}{n\,V_b} = 0 \tag{5.4}$$

It should be noted that in V2G mode, the same principle can be applied. The only difference is that the voltage V_{DC} should be replaced by $n\,V_b$ and inversely in all equations. Like any modulation strategy, the SPS has advantages and disadvantages. Table 5.1 groups together the most important set of characteristics of the SPS modulation.

Advantages	Drawbacks
Simplest modulation (1 degree of freedom)	Important RMS current flowing the transformer [130]
Easy to implement control	Limited operating range with high switching losses
Less component stress	Efficiency dropping during voltage mismatch losing ZVS conditions [131]
High efficiency at high power levels	Operation at high efficiency only at narrow voltage range [131]

Table 5.1 – Advantages and drawbacks of SPS modulation

5.4.2 Dual Phase Shift (DPS) modulation

DPS modulation strategy used in DAB converters involves an addition of another phase shift called the inner phase shift. DPS with two degrees of freedom can help to extend the ZVS range. It controls two phase shift angles: the first is between arms in the identical full bridge side and the second is between primary and secondary full bridges. Figure 5.4 represents the main waveforms of the DPS modulation (in G2V mode for a boost mode).

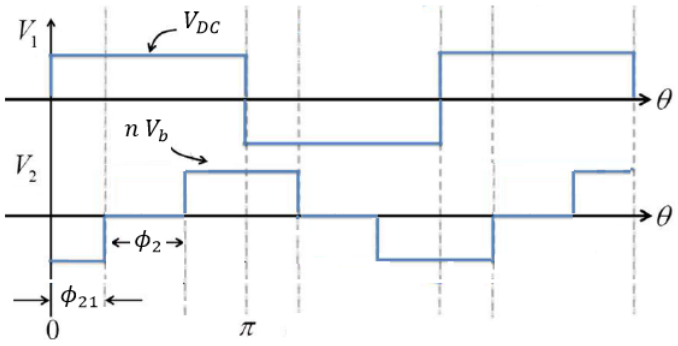

Figure 5.4 – DPS modulation waveforms in G2V mode (for a boost mode)

The angle ϕ_{21} represents the phase shift between the two full bridges primary and secondary, and ϕ_2 represents the phase shift between the two arms of the secondary full bridge.
It is clearly seen that the voltage at the primary side V_1 is with two levels, but that at the secondary side V_2 is with three levels.
The power flux expression for the DPS modulation is defined by Equation(5.5) [129]:

$$P = \frac{V_{DC}\, n\, V_b}{2\pi f_s L}\left(\phi_{21}\left(1 - \frac{\phi_{21}}{\pi}\right) - \frac{\phi_2^2}{2\pi}\right) \tag{5.5}$$

The gain of the DAB converter m, in G2V mode, is defined as follows:

$$m = \frac{n\, V_b}{V_{DC}} \tag{5.6}$$

where n is the transformer ratio.
It should be noted, as explained in [132], that the angles ϕ_2 and ϕ_{21} are related by Equation(5.7):

$$m\,(0.5 - \phi_{21} - \phi_2) = 0.5 - \phi_{21} \tag{5.7}$$

Like SPS, the mean value of the inductor current is a function of the phase shift angles as follows in Equation(5.8) [132]:

$$\overline{i_L} = \frac{V_{DC}}{2m f_s L}(1 - 2\phi_{21})\left(\phi_{21}(1 + m^2) + \frac{m-1}{2}\right) \tag{5.8}$$

Based on Equation(5.8), ϕ_{21} can be obtained by solving the following Equation(5.9):

$$a\,\phi_{21}^2 + b\,\phi_{21} + c = 0 \tag{5.9}$$

where a, b and c are defined in Equations (5.10), (5.11) and (5.12) respectively:

$$a = 2\,(1 + m^2) \tag{5.10}$$

$$b = -m^2 + m - 2 \tag{5.11}$$

$$c = \frac{1-m}{2} + \overline{i_L}\frac{2mf_sL}{V_{DC}} \tag{5.12}$$

Then, ϕ_2 can be calculated based on Equation(5.7).

Table 5.2 shows some characteristics of the DPS modulation.

Advantages	Drawbacks
2 degrees of freedom for control	Complex control
Lower RMS transformer current compared to SPS	No ability of ZVS for all switches at light load
Lower switching loss compared to SPS	

Table 5.2 – Advantages and drawbacks of DPS modulation

5.5 Proposed control strategy

In the literature, most of existing work studied the DAB converter modulation strategies in an open loop without a phase shift control law [119, 124, 127]. Even if there is a closed loop phase shift control law, this control aimed to regulate the battery voltage or current [120, 123, 125, 126], without any power factor correction in case of an EV charger [123].

The main contribution of this chapter, presented in this section, is to design a closed loop control strategy, combined with the common modulation strategies SPS and DPS, for the DAB converter implemented in the single phase bidirectional EV charger. The aim is to regulate the DC bus voltage and ensure the grid current control in both G2V and V2G modes.

The control algorithm is essential to handle the input of the modulation strategy. The output of this control algorithm is used to obtain the phase shift angle of the adopted modulation strategy.

Figure 5.5 represents the proposed control algorithm applied for the EV charger including the control of the DAB converter.

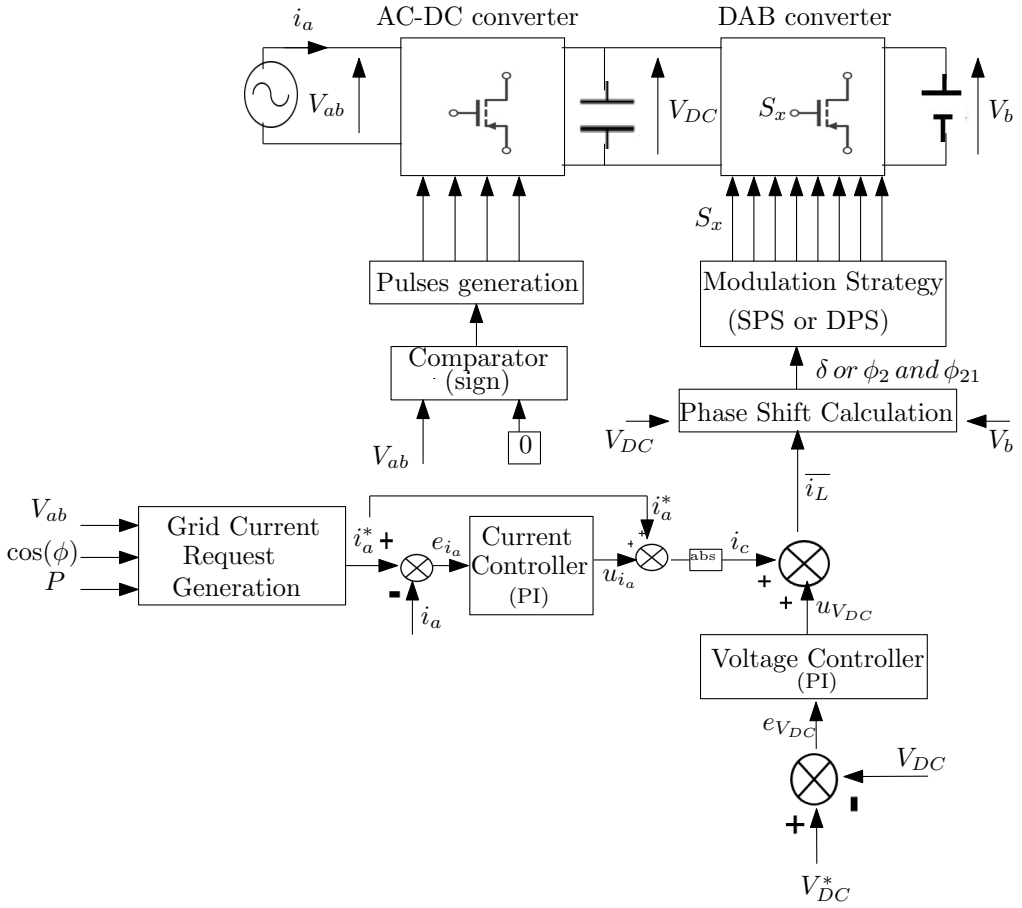

Figure 5.5 – Proposed control algorithm for the DAB charger

From the global view of Figure 5.5, it is clearly seen that there are two parts. The first that generates the pulses for the AC-DC converter and the second that effectively represents the responsible of the charger control by generating the DAB converter pulses. On the one hand, the operating principle of the AC-DC converter is made such as when the voltage V_{ab} passes through zero, the MOSFETs switch diagonally to maintain a positive voltage on the DC bus of the sine rectified type. To doing that, a comparator between V_{ab} and zero is made in order to obtain the sign of V_{ab} and generate the pulses for rectification. On the other hand, the DAB converter requires a control strategy which must guarantee the realization of the current setpoint while ensuring the charger stability. Figure 5.5 shows the general structure of the control strategy of the DAB converter. It is basically divided into three levels.

A first level of the grid current control that includes three steps:

- A step that calculates the current setpoint i_a^* according to the power request P, the power factor $\cos(\phi)$ and the grid voltage measurement V_{ab}, using the following Equation (5.13):

$$i_{a-RMS}^* = \frac{P}{V_{ab-RMS}\cos(\phi)} \tag{5.13}$$

where i_{a-RMS}^* and V_{ab-RMS} are the RMS values of the grid current and grid voltage

respectively. Then the current setpoint i_a^* can be defiend as Equation (5.14):

$$i_a^* = \sqrt{2}\, i_{a-RMS}^* \sin(\theta_{PLL}) \tag{5.14}$$

where the angle θ_{PLL} is obtained using the Phase Locked Loop (PLL) of the grid and corresponds to the grid frequency.

- A step that implements a PI controller in order to ensure the grid current stability and cancel the current tracking error $e_{i_a} = i_a^* - i_a$ as presented in Equation (5.15):

$$u_{i_a} = K_p\, e_{i_a} + K_i \int e_{i_a} dt \tag{5.15}$$

- A step that obtains the variable i_c from the absolute value of the addition of the PI controller output u_{i_a} in Equation (5.15) to the grid current setpoint i_a^* in Equation (5.14), as presented in Equation (5.16):

$$i_c = |u_{i_a} + i_a^*| \tag{5.16}$$

A second level that provides a DC bus voltage controller. The DC bus voltage request V_{DC}^* is defined as the rectified sine wave of the measured AC voltage V_{ab}. In other word, V_{DC}^* is the absolute value of V_{ab}. V_{DC}^* is defined as in Equation (5.17):

$$V_{DC}^* = \sqrt{2}\, V_{ab-RMS} \,|\sin(\theta_{PLL})| \tag{5.17}$$

Then, a PI controller is implemented to ensure the DC bus voltage stability and cancel the DC bus voltage tracking error $e_{V_{DC}} = V_{DC}^* - V_{DC}$ as presneted in Equation (5.18):

$$u_{V_{DC}} = K_p\, e_{V_{DC}} + K_i \int e_{V_{DC}} dt \tag{5.18}$$

It should be noted that the purpose of the DC bus voltage control loop is to dampen medium frequency oscillations of the converter. In fact, the grid inductor and the capacitors at the input of the DAB converter can generate an oscillation of medium frequency (between 1 and 4 kHz) which give a DC bus voltage response sensible to the grid voltage harmonics and maybe can destabilize the system. In order to solve this problem, the proposed solution consists of damping the response by injecting the medium frequency disturbances in the current setpoint. For this reason, the DC bus voltage, where the medium frequency disturbances appear, is controlled via a PI controller.
The output of the voltage controller is added to the output of the current controller.

The third level represents the final stage of the control strategy. It is the modulation block which transforms the output of the control laws into a switching order for the DAB converter. It can be divided into two steps:

- The first step consists of using the output of the current and voltage controllers in

the phase shift calculation. The aim is to obtain the average value of the inductor current $\overline{i_L}$ presented in Equations (5.3) and (5.8) for the SPS and DPS modulations respectively. To do this, i_c in Equation (5.16) is added to the DC bus voltage controller output $u_{V_{DC}}$ in Equation (5.18) to obtain $\overline{i_L}$ as presented in Equation (5.19):

$$\overline{i_L} = i_c + u_{V_{DC}} \tag{5.19}$$

Then, based on Equation (5.19), the necessary phase shift angle(s) can be obtained using either Equation (5.4) for SPS or Equation (5.9) for DPS.

- In the final step, the obtained phase shift(s) is used as input of the modulation block. The modulation block can be based on SPS or DPS. The aim of this block is to generate the pulses of the MOSFETs for the DAB converter at a fixed switching frequency of 140 kHz.

5.6 Simulations and Results

5.6.1 System and simulation configuration

The analysis of the DAB converter operation and its performance requires the implementation of different modulation strategies and comparison of their results.
MATLAB/SIMULINK is used to implement the charger model and control system (Discrete solver with fixed step of T_s). Table 5.3 displays the parameter settings.

$C_{DC-bus}(\mu F)$	0.2	$L(\mu H)$	0.1
$T_s(\eta s)$	10	$f_s(kHz)$	140
V_{ab-max} (V)	325	n	1
V_{b-max} (V)	430	P_{max} (W)	7400

Table 5.3 – DAB charger configuration

A quick demonstration of the above discussed control strategies is done for a real-world model of the bidirectional charger using the DAB converter.
It worth mentioning that the simulation takes into account the system with the input/output filters (and line impedance) as presented in Figure 5.1. Moreover, the voltage and current measurements based on the real EV charger model are used for the control system implementation.

The following simulations show the results of some operating points in both G2V and V2G modes.
In G2V mode, the efficiency is computed by dividing the average value of the power from the battery side by the average value of that from the grid side, and inversely in V2G mode.

5.6.2 G2V mode

Operating point: V_b=430 V and P=7400 W

For this simulation, the power request P is presented in Figure 5.6 where it increases to reach 7400 W.

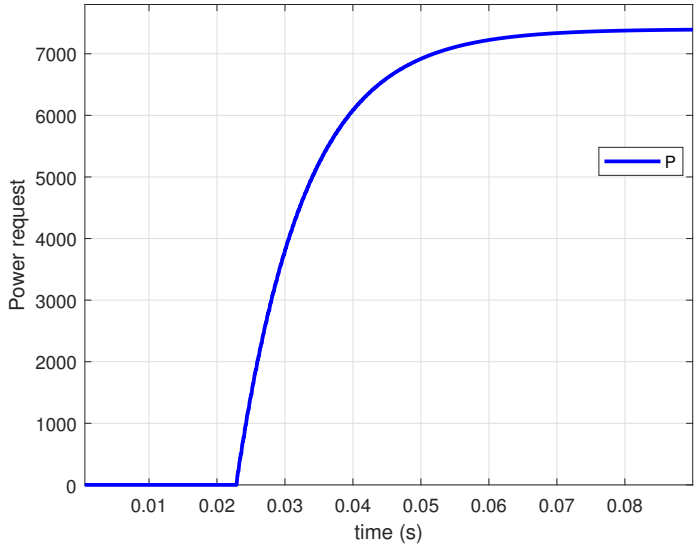

Figure 5.6 – Power request in G2V mode

SPS modulation

The grid voltage and current are shown in Figure 5.7. It is clearly seen that the phase current i_a follows the current setpoint $i_a^\star$ and is in phase with the phase voltage V_{ab}. For the SPS modulation, we noted that the current response at zero crossing (when V_{ab} passes through zero) is disturbed. This is due to a delay introduced either by filters or by a bad estimation of the voltage by the PLL (Phase Locked Loop).

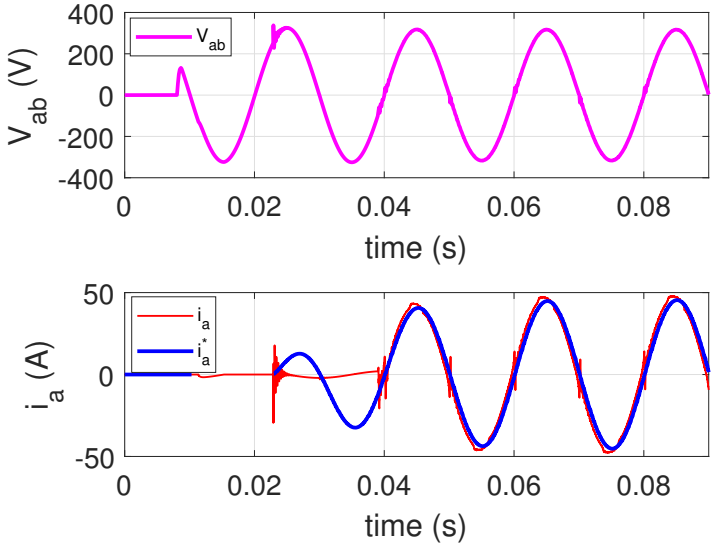

Figure 5.7 – Phase voltage and current with SPS in G2V mode for V_b=430 V and P=7,4 kW

In Figure 5.8, the DC bus voltage V_{DC} is presented where it follows the DC bus voltage request V_{DC}^{*} with maximal tracking error of 2 V.

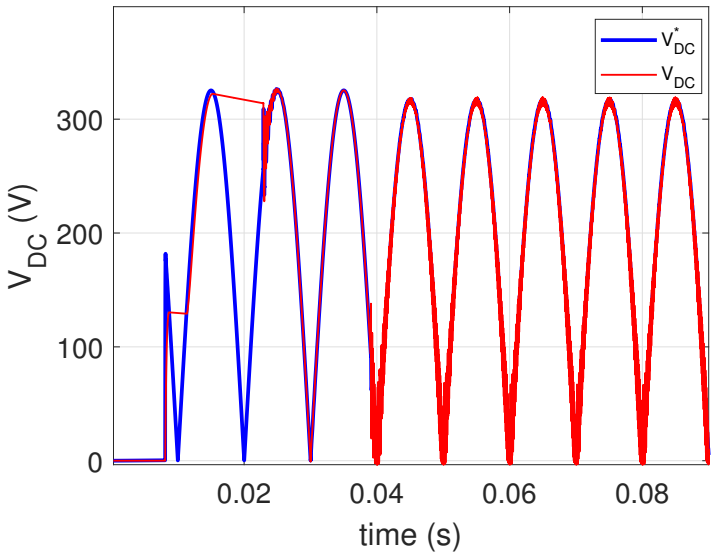

Figure 5.8 – DC bus voltage with SPS in G2V mode for V_b=430 V and P=7400 W

The inductor current i_L of the DAB converter is shown in Figure 5.9. It is clearly seen, especially when there is a zero crossing of the phase voltage, that there is an important current magnitude which exceeds 100 A and increases conduction losses.

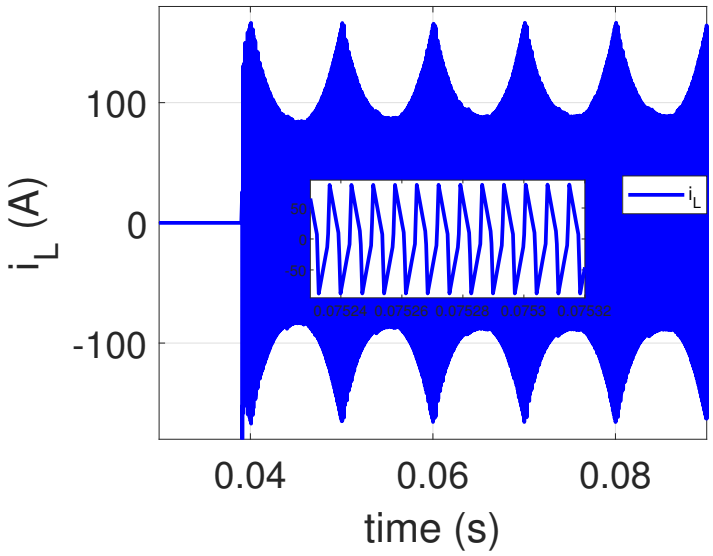

Figure 5.9 – Inductor current with SPS in G2V mode for V_b=430 V and P=7400 W

The controlled phase shift angle δ, presented in Equation (5.4), and a zoom of the main waveforms of the MOSFETs' signals of the DAB converter (S_1 and S_5) are presented respectively in Figures 5.10 and 5.11.

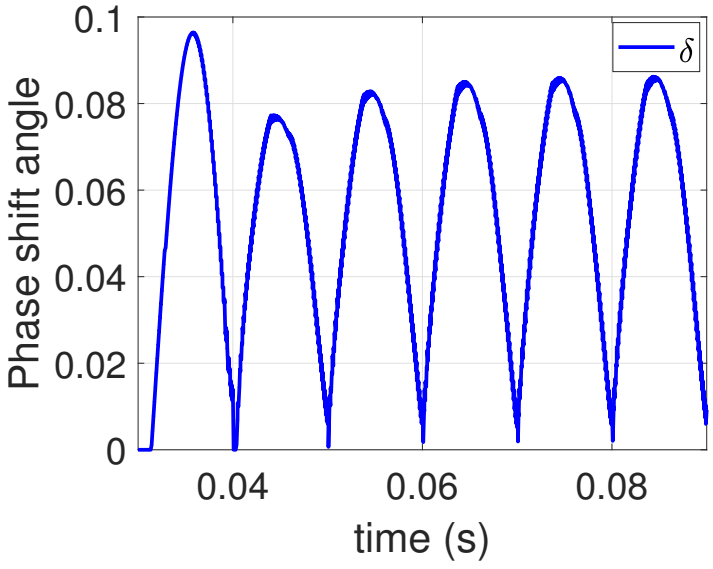

Figure 5.10 – Phase shift angle with SPS in G2V mode for V_b=430 V and P=7400 W

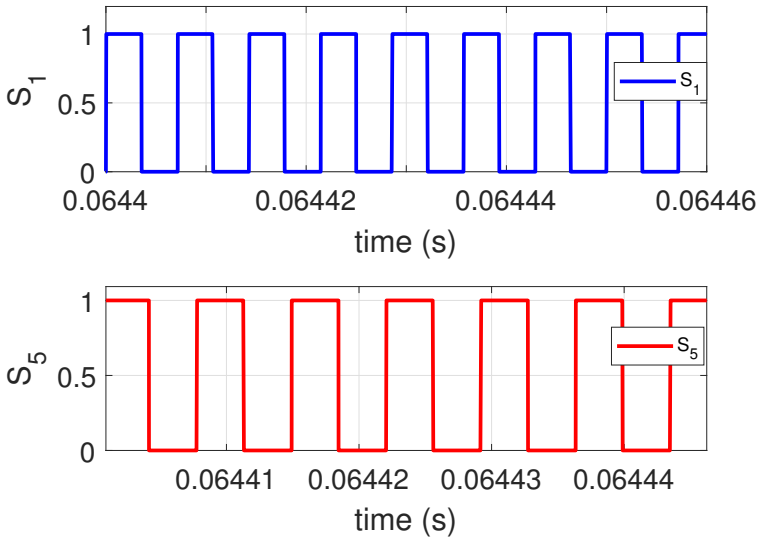

Figure 5.11 – MOSFETs' waveforms with SPS in G2V mode for V_b=430 V and P=7,4 kW

DPS modulation

The grid voltage and current are shown in Figure 5.12. The DPS modulation provides a better current response than that with the SPS modulation in terms of control performance (a comparison table will be shown at the end of this section).

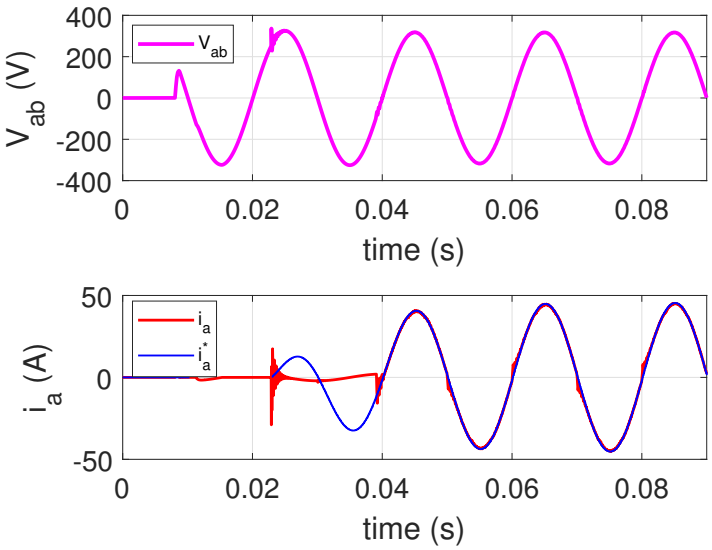

Figure 5.12 – Phase voltage and current with DPS in G2V mode for V_b=430 V and P=7,4 kW

The DC bus voltage and inductor current reponses are presented in Figures 5.13 and 5.14 respectively. It is clearly seen that the DPS modulation presents lower current magnitude than that with the SPS modulation which reduces the conduction losses and can improve the efficiency.

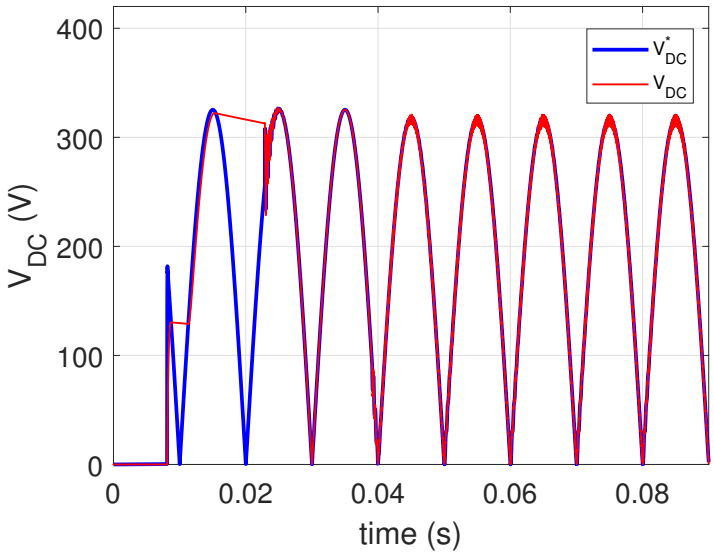

Figure 5.13 – DC bus voltage with DPS in G2V mode for V_b=430 V and P=7400 W

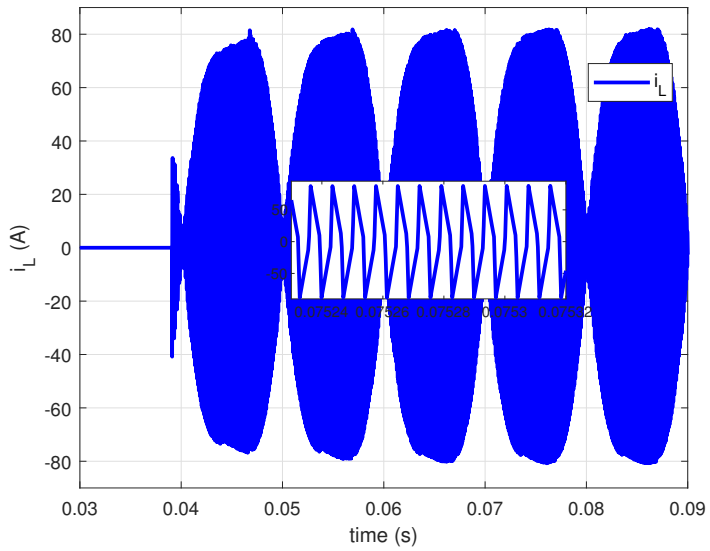

Figure 5.14 – Inductor current with DPS in G2V mode for V_b=430 V and P=7400 W

The two controlled phase shift angles ϕ_2 and ϕ_{21} of the DPS, presented in Equation (5.9), and the MOSFETs' signals of the DAB converter are presented respectively in Figures 5.15 and 5.16.

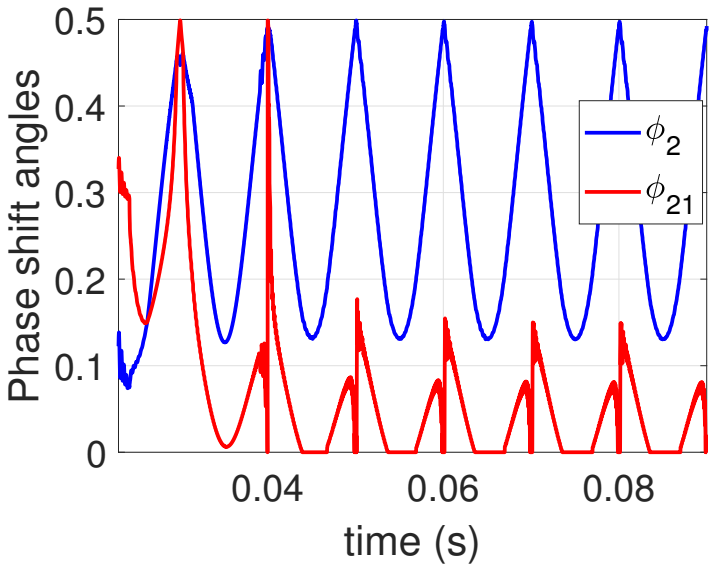

Figure 5.15 – Phase shift angles with DPS in G2V mode for V_b=430 V and P=7400 W

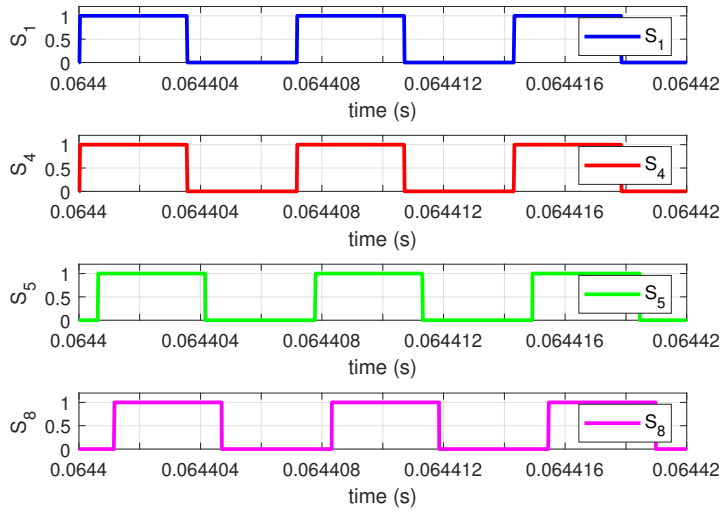

Figure 5.16 – MOSFETs' waveforms with DPS in G2V mode for V_b=430 V and P=7,4 kW

Comparison

A comparison table of the modulation strategies is shown in Figure 5.17.

G2V V_b=430 V, P=7400 W	$\lvert e_{i_a-max} \rvert$ (A)	$\lvert e_{V_{DC}-max} \rvert$ (V)	$\lvert i_{L-max} \rvert$ (A)	Efficiency (%)
SPS	5	2	160	92
DPS	1	2	80	94,5

Figure 5.17 – Comparison table in G2V mode for V_b=430 V and P=7400 W

It should be noted that $|e_{i_a-max}|$ is the maximal absolute value of the grid current

tracking error e_{i_a}, $|e_{V_{DC}-max}|$ is the maximal absolute value of the DC bus voltage tracking error $e_{V_{DC}}$ and $|i_{L-max}|$ is the maximal magnitude of the DAB inductor current i_L.
It can be observed that the DPS modulation presents better control performance than the SPS modulation in terms of the grid current and DC bus voltage tracking error. Furthermore, the DPS modulation reduces the peak value of the DAB inductor current which reduces the losses and leads to improve the charger efficiency.

Operating point: V_b=350 V and P=1000 W

In this paragraph, the results are shown for the SPS and DPS modulations with another operating point in order to ensure the advantage of the DPS modulation compared to the SPS modulation in improving the control performance and charger efficiency.

SPS modulation

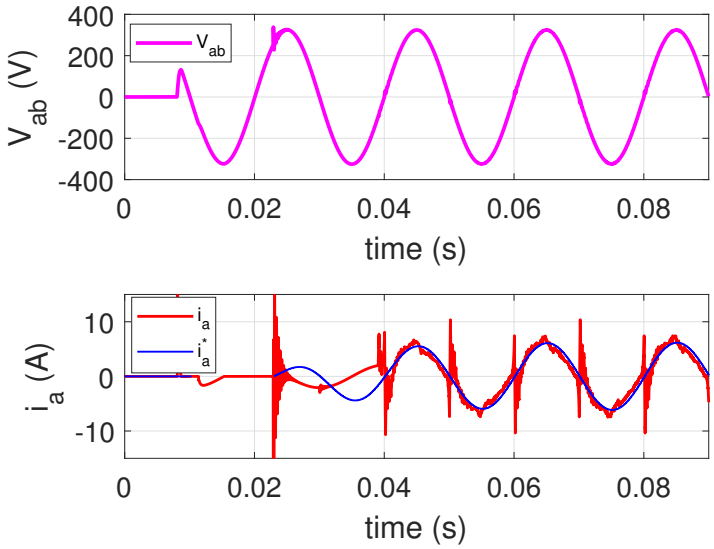

Figure 5.18 – Phase voltage and current with SPS in G2V mode for V_b=350 V and P=1 kW

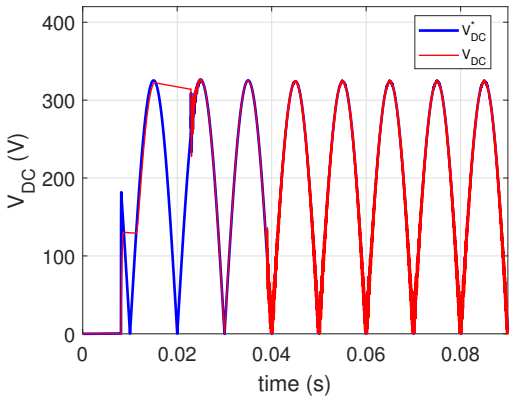

Figure 5.19 – DC bus voltage with SPS in G2V mode for V_b=350 V and P=1000 W

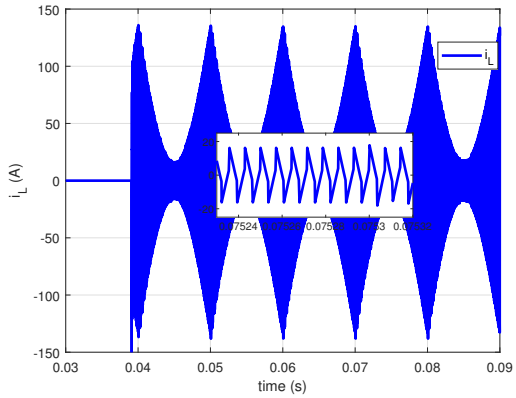

Figure 5.20 – Inductor current with SPS in G2V mode for V_b=350 V and P=1000 W

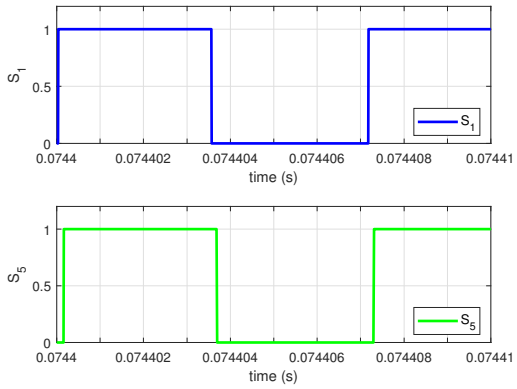

Figure 5.21 – MOSFETs' waveforms with SPS in G2V mode for V_b=350 V and P=1000 W

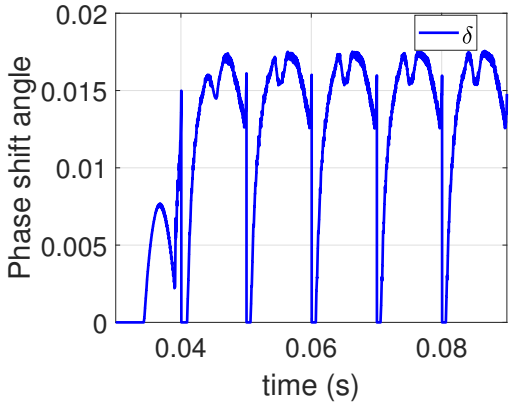

Figure 5.22 – Phase shift angle with SPS in G2V mode for V_b=350 V and P=1000 W

DPS modulation

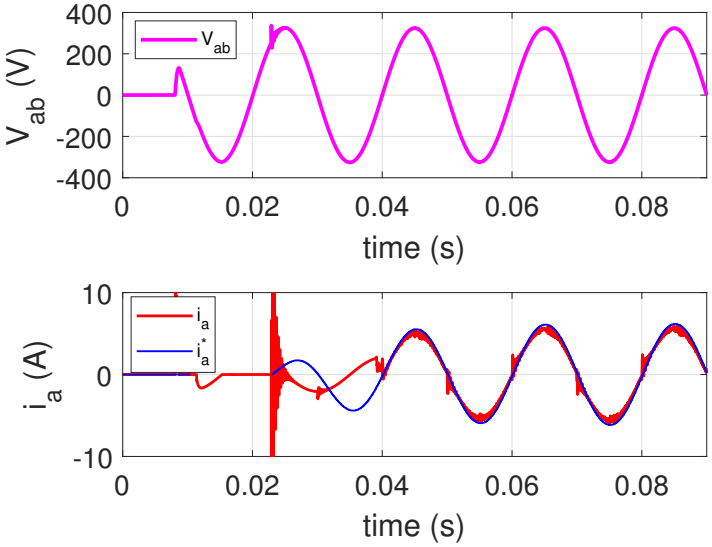

Figure 5.23 – Phase voltage and current with DPS in G2V mode for V_b=350 V and P=1 kW

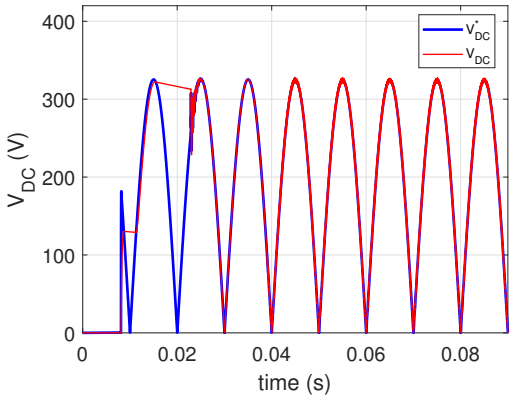

Figure 5.24 – DC bus voltage with DPS in G2V mode for V_b=350 V and P=1000 W

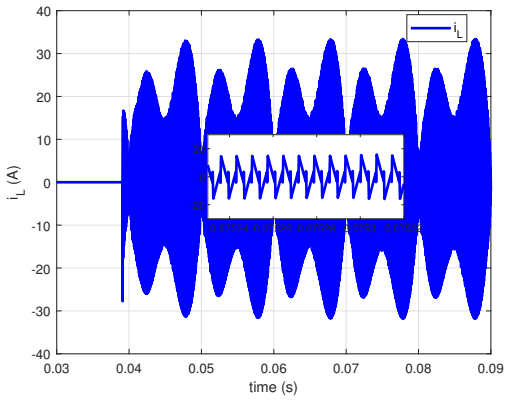

Figure 5.25 – Inductor current with DPS in G2V mode for V_b=350 V and P=1000 W

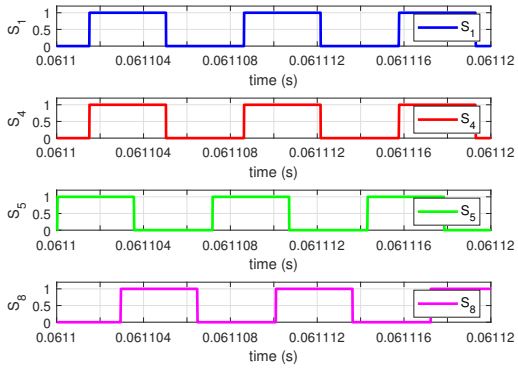

Figure 5.26 – MOSFETs' waveforms with DPS in G2V mode for V_b=350 V and P=1 kW

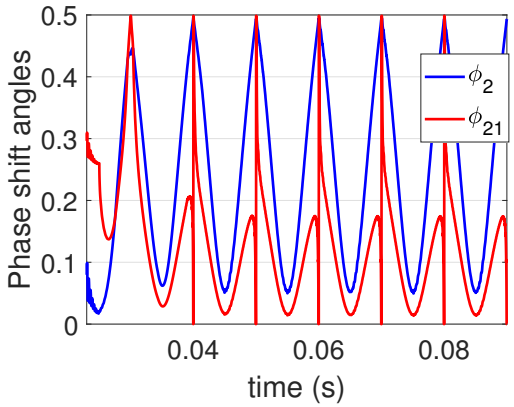

Figure 5.27 – Phase shift angles with DPS in G2V mode for V_b=350 V and P=1000 W

Comparison

As shown in Figure 5.28, the comparison table reflects the advantage of the DPS modulation in improving the current control performance and charger efficiency.

G2V V_b=350 V, P=1000 W	$\lvert e_{i_a-max} \rvert$ (A)	$\lvert e_{V_{DC}-max} \rvert$ (V)	$\lvert i_{L-max} \rvert$ (A)	Efficiency (%)
SPS	5	1	135	80
DPS	1	1	33	95

Figure 5.28 – Comparison table in G2V mode for V_b=350 V and P=1000 W

5.6.3 V2G mode

Operating point: V_b=430 V and P=7400 W

For this simulation, the power request is presented in Figure 5.29 where it increases to reach 7400 W. The minus sign represents the sens of the power flow i.e. V2G mode.

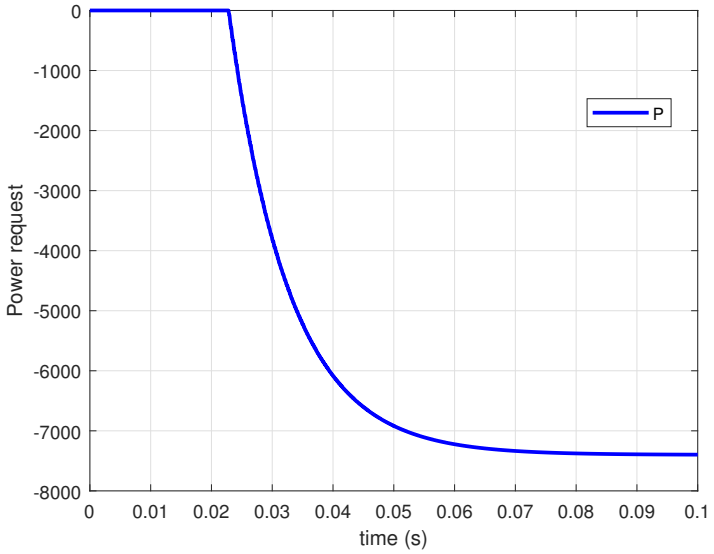

Figure 5.29 – Power request in V2G mode

SPS modulation

The grid voltage and current are shown in Figure 5.30.

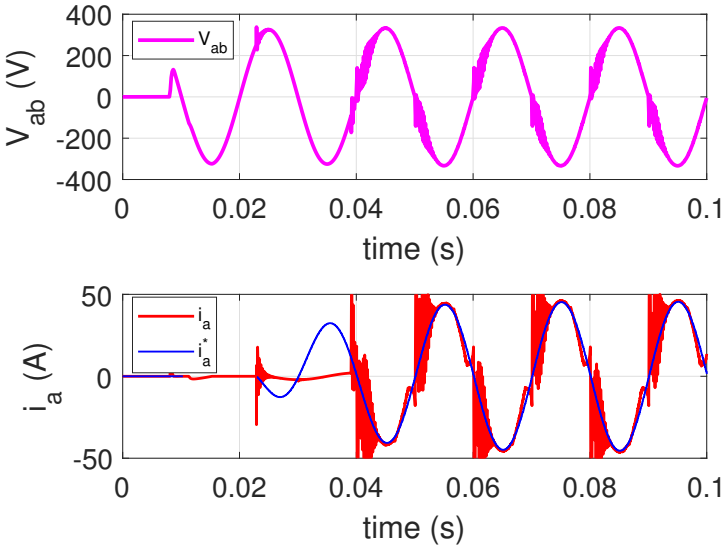

Figure 5.30 – Phase voltage and current with SPS in V2G mode for V_b=430 V and P=7400 W

It is clearly seen that the phase current i_a, which is in opposition of phase with V_{ab}, follows the current setpoint i_a^* but with an important tracking error. For the SPS modulation, we noted that the current response at zero crossing (when V_{ab} passes through zero) is disturbed. This is due to a delay introduced either by filters or by a bad estimation of the voltage by the PLL (Phase Locked Loop).

The DC bus voltage, inductor current, MOSDETs signals and the phase shift are shown in Figures 5.31, 5.32, 5.33 and 5.34 respectively.

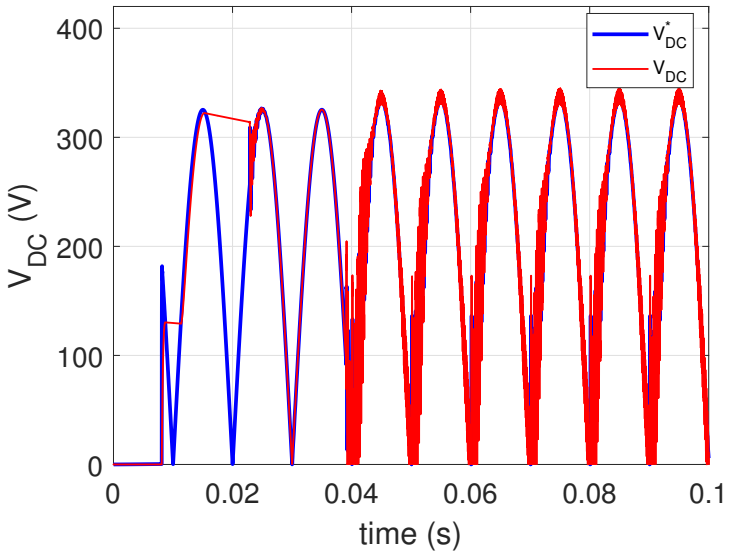

Figure 5.31 – DC bus voltage with SPS in V2G mode for V_b=430 V and P=7400 W

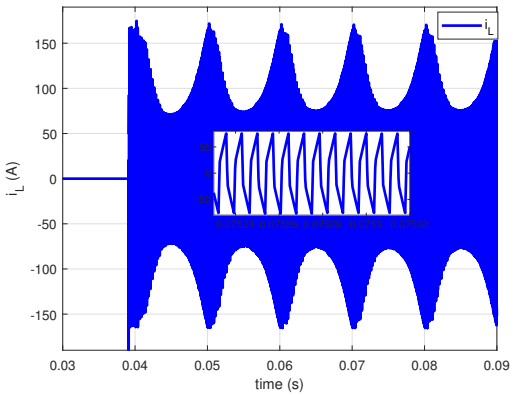

Figure 5.32 – Inductor current with SPS in V2G mode for V_b=430 V and P=7400 W

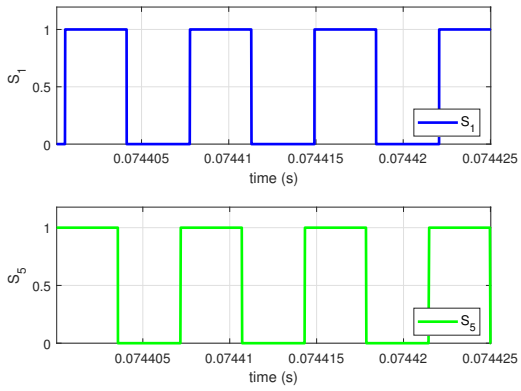

Figure 5.33 – MOSFETs' waveforms with SPS in V2G mode for V_b=430 V and P=7400 W

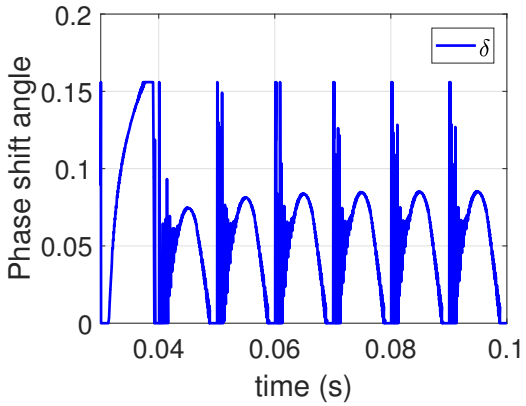

Figure 5.34 – Phase shift angle with SPS in V2G mode for V_b=430 V and P=7400 W

DPS modulation

The results with the DPS modulation for this operating point are shown in Figures 5.35, 5.36, 5.37, 5.38 and 5.39 respectively.

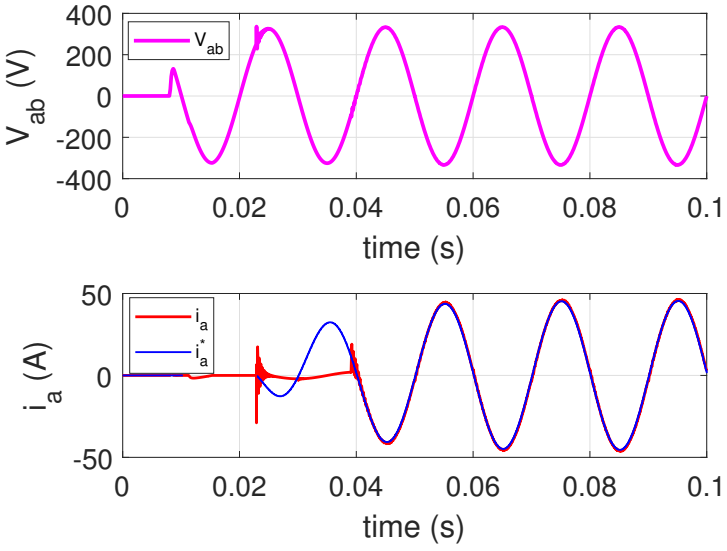

Figure 5.35 – Phase voltage and current with DPS in V2G mode for V_b=430 V and P=7400 W

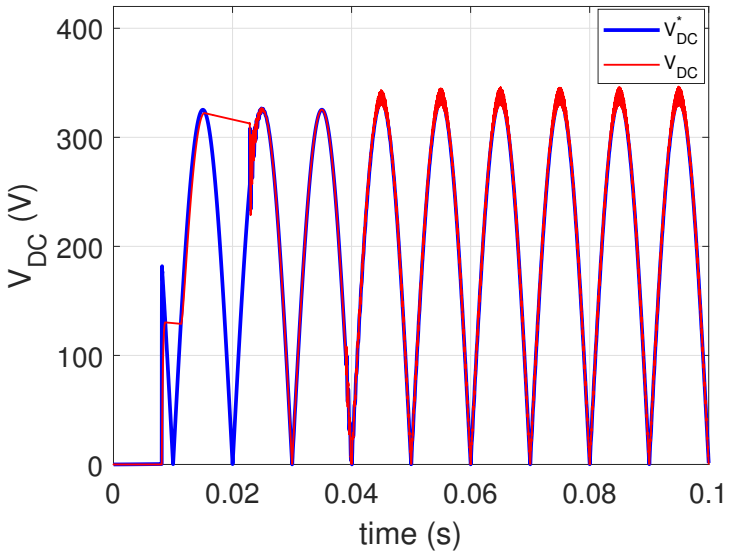

Figure 5.36 – DC bus voltage with DPS in V2G mode for V_b=430 V and P=7400 W

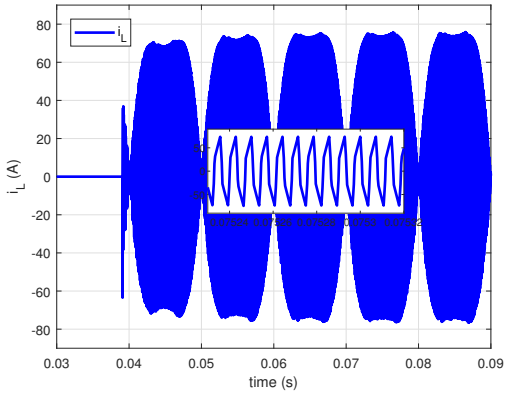

Figure 5.37 – Inductor current with DPS in V2G mode for V_b=430 V and P=7400 W

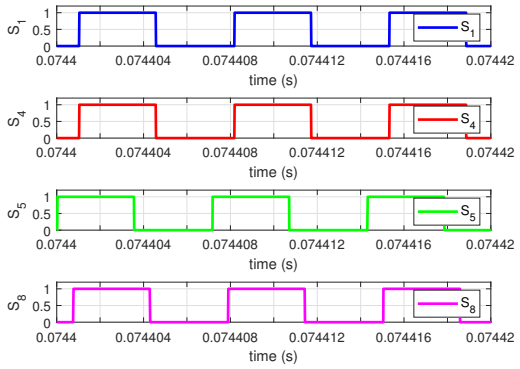

Figure 5.38 – MOSFETs' waveforms with DPS in V2G mode for V_b=430 V and P=7400 W

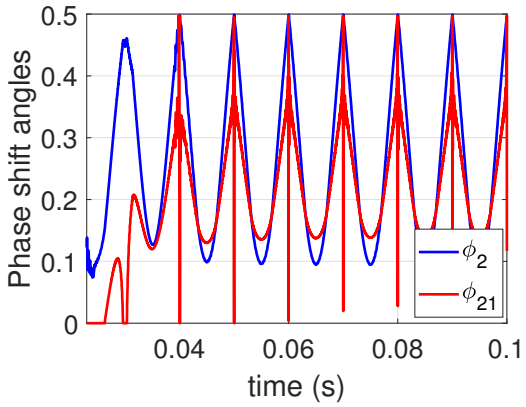

Figure 5.39 – Phase shift angles with DPS in V2G mode for V_b=430 V and P=7400 W

Comparison

A comparison table is presented in Figure 5.40.

V2G V_b=430 V, P=7400 W	$\lvert e_{i_a-max} \rvert$ (A)	$\lvert e_{V_{DC}-max} \rvert$ (V)	$\lvert i_{L-max} \rvert$ (A)	Efficiency (%)
SPS	30	10	170	88
DPS	2	2	74	93

Figure 5.40 – Comparison table in V2G mode for V_b=430 V and P=7400 W

Like G2V mode, the DPS modulation in V2G mode presents its superiority compared to the SPS modulation where it can significantly reduce the DC bus voltage and grid current tracking errors and the DAB inductor current magnitude, and improves the charger efficiency.

5.7 Conclusion

The bidirectional power flow, low component stress, small size and high-power density characteristics of the DAB converter topology make it particularly appealing for the EV charger application.

In this chapter, a single-phase bidirectional EV charger structure made of an AC-DC converter connected to the DC-DC DAB converter is studied. The AC-DC converter is used for rectification, while the role of the DAB converter is to ensure the grid current and DC bus voltage stability.

Several research works in the literature studied the DAB converter. To the best of our knoweldge, most existing work in the literature focused on the modulation strategies (SPS, DPS, EPS and TZM) for the DAB converter alone or as a part of an EV charger but in an open loop without a phase shift control law. Moreover, the existing work, which includes a closed loop phase shift control law, aimed to only regulate the battery voltage or current without any power factor correction.

The new challenge of this chapter is to provide a bidirectional charger control, comprising a bidirectional DAB converter control strategy, that aims to ensure the grid current and the DC bus voltage control and improve the charger efficiency in both G2V and V2G modes. Common modulation strategies for the DAB converter existing in the literature, such as SPS and DPS, as well as their advantages and disadvantages are studied and applied in the DAB control strategy.

The proposed control strategy has been implemented in order to provide the necessary phase shift angle for the adopted modulation strategy (SPS or DPS) based on an averaged DAB model.

Many simulations are given to validate the performance of the proposed control algorithm based on a real DAB charger model. A comparative study between the SPS and DPS modulation strategies has been conducted in terms of control performance and charger efficiency in both G2V and V2G modes.

The results show the effectiveness of the proposed control strategy and the superiority of the DPS modulation compared to the SPS modulation.

General Conclusion

This thesis is supported by the project Chair between Centrale Nantes and Renault in Guyancourt about EV performances. It is classified under the research area of energy management and control of the EV charging and static converters.

Minimizing our use of fossil fuels as much as possible in transformation plans will contribute to halting the climate change catastrophe. Therefore, the first evident step to reduce the CO2 footprint is to replace thermal vehicles with electric ones. Energy transport is today a major component of the energy transition. As part of the energy transition, the technology of the bidirectional charger for EVs is gaining importance. It allows to return the electricity stored in the EV battery to Grid (V2G), Home (V2H), or Load (V2L), which is in one word defined as Vehicle-to-Everything (V2X) mode. The EV OnBoard charger is of two parts: AC-DC converters and DC-DC converters. The two modes Grid-to-Vehicle (G2V) and V2X are provided by the bidirectional AC-DC and DC-DC converters.

In this thesis, we have been interested in the control of the bidirectional EV charger. The main goal has been to find new solutions to control the bidirectional converters of the EV charger in order to improve the performance and efficiency as well as to reduce the cost. The reason behind this interest was to respond to the need of covering the whole operating zone of the EV charger with a highest performance and lowest cost.
Futhermore, the aim was to address many difficulties that still exist regarding the control of bidirectional isolated DC-DC converters frequently chosen for applications requiring great power density, such as EV chargers. Therefore, one of the objectives of this thesis was to try to bring together the work specific to power electronics and that in the field of automatic control.

Motivated by the industrial collaboration, the work has been firstly focused on the bidirectional DC-DC LLC resonant converter in order to improve the charger efficiency across both battery power and voltage ranges in V2X mode. The feasibility conditions and constraints of the EV charger provide a cost minimization challenge related to software (control performance) and hardware (charger dimension and efficiency) implementation in both G2V and V2G modes.
In an advanced stage, the work focused on implementing a control strategy of the entire charger composed of AC-DC and DC-DC converters. Different solutions have been proposed to improve the performance of the bidirectional EV charger with the DC-DC LLC

converter topology.
Finally, another bidirectional EV charger with the DC-DC DAB converter topology has been studied. The DAB topology has not been predicted from the beginning of the thesis. Many advantages of this topology, especially the use of less components (less cost) and easier control, interest the manufacturer.

In chapter 1, a state of the art has been presented. Firstly, a literature review of many topologies of bidirectional isolated DC-DC converters has been generated. The characteristics and limitations related to each topology have been presented. A comparative study between these topologies in terms of some essential parameters, such as converter efficiency, design complexity and soft switching (ZVS or ZCS) range, has been conducted. Moreover, existing modulation strategies for DC-DC converters, such as PFM, PWM and PSM, have been defined.
The bidirectional DC-DC LLC resonant converter has been studied. Modelling approaches of LLC converter such as large and small signal modelling have been presented. The small signal model concept applied to the DC-DC LLC converter in the forward mode (i.e. G2V mode), presented in the literature, will be used in chapter 2 to represent the DC-DC LLC converter in the reverse mode (i.e. V2X mode) and apply linear controllers. On the other hand, the existing large signal model will be rewritten, in chapter 3, combined with the PSM strategy in order to apply non-linear controllers.
Several control and optimization strategies, proposed in the literature for the LLC resonant converter, have been studied. The existing solutions for the DC-DC LLC converter are only related to the forward mode (G2V mode) with narrow battery voltage and power zones. Furthermore, many research studies that focused on different topologies of the EV charger have been highlighted.

Chapter 2 represents the first contribution of the thesis related to software and hardware based performance improvement for DC-DC LLC converter. It proposes a solution to the open problem related to the control of the DC bus voltage of the DC-DC LLC converter in V2X mode over a wide variation of the battery voltage and power. On the one hand, several modulation strategies of the LLC resonant converter, in V2X mode, have been designed and implemented according to an averaged small signal model based on the FHA. DC bus voltage control based on the Gain Inversion (GI) method has been highlighted. The drawbacks of the PFM strategy have been presented. Then, fixed switching frequency strategies, such as PWM and PSM, have been proposed to avoid PFM strategy limitations. The benefits and drawbacks of each strategy have been studied. The results show the advantages of the PSM strategy in improving the DC-DC LLC converter control performance and efficiency for the entire operating zone in V2X mode.
On the other hand, an optimized design of the bidirectional DC-DC LLC resonant converter for a bidirectional EV charger application has been proposed. To the best of our knowledge, compared to what is existing, this problem was not yet treated. The main goal was to reduce the converter cost and increase the soft-switching range for a wide

variation of the battery voltage and power in both G2V and V2X modes. The decision variables have been chosen considering the LLC resonant structure and the control frequencies in both G2V and V2X modes. The linear and non-linear constraints have been defined based on the hardware and control requirements. An optimization methodology has been generated for wide battery voltage and power ranges. The converter cost has been minimized and control frequency feasibility zones have been improved. The optimization results show an important improvement in the converter efficiency and control performance in both G2V and V2X modes.

In chapter 3, the main contribution has been to propose robust control strategies in order to ensure robustness against different disturbances and uncertainties in the DC-DC LLC converter system. Two control laws combined with the PSM strategy have been designed and implemented in V2X mode. On the one hand, a control strategy based on the Model Free Control (MFC) has been highlighted. The proposed MFC provides a robust control law against disturbances without prior knowledge of the mathematical complex model of the DC-DC LLC converter.
On the other hand, an improved LLC model has been designed based on the PSM approach to get enough information about the DC-DC LLC converter dynamics, which helps later in the control design and stability proof. Based on this model, the non-linear Adaptive Super Twisting Control (ASTC) has been proposed to provide the DC bus voltage control and ensure robustness in the event of disturbances. A theoretical study of the DC-DC LLC converter model and PSM approach combining the ASTC has been developed. The stability of the DC-DC LLC converter dynamics has been analytically proven.
Simulation results were presented to verify the effectiveness of proposed control strategies (MFC and ASTC) under several disturbances in comparison with the conventional control laws, which demonstrate a great agreement with the theoretical analysis.

Chapter 4 deals with problematic of the bidirectional EV charger control including bidirectional AC-DC and DC-DC converters. In this chapter, the AC-DC Vienna converter has been used to ensure the grid current control with a high power factor. The DC-DC LLC converter, studied alone in chapters 2 and 3, is implemented beside the AC-DC converter. The control strategy, in both G2V and V2G modes, has been proposed to the EV charger and compared to the DC-DC LLC converter alone. The aim is to cover the whole operating zone of the bidirectional EV charger with good control performance and high efficiency. In G2V mode, two solutions have been presented. The PFM strategy with variable DC bus voltage request has been firstly applied for the DC-DC LLC converter. On the other hand, a backstepping control strategy by the help of the AC-DC converter has been designed. In V2G mode, the PSM strategy has been applied for the the DC-DC LLC converter in order to avoid the PFM limitations. The proposed strategies ensure the DC bus voltage and grid current control across battery voltage and power variation in both G2V and V2G modes. Compared to the common PFM and PSM strategies applied to the DC-DC LLC converter alone, it has been confirmed that the proposed control

strategy applied to the EV charger improves the control performance and efficiency.

In chapter 5, another topology of a bidirectional single phase EV charger including the DAB converter topology has been studied. The AC-DC converter, implemented in this charger, is used only for rectification in order to obtain a rectified sine type voltage at the input of the DAB converter stage. The DAB converter is the responsible for the charger control in both G2V and V2G modes. Two common modulation strategies for the DAB converter with a fixed switching frequency, such as SPS and DPS, have been presented. A control strategy of the bidirectional charger, including the DAB converter's control, that aims to ensure the grid current stability and DC bus voltage control has been proposed. The output of grid current and DC bus voltage controllers allows to obtain the necessary phase shift angle(s) in order to apply the adopted modulation strategy. The effectiveness of the proposed control algorithm has been validated by many simulations based on a real DAB charger model. A comparative study between the SPS and DPS modulations has been conducted in terms of the control performance and charger efficiency in both G2V and V2G modes.

Perspectives and open topics include:

- Experimental validation of the proposed control strategies for a bidirectional EV charger setup
- Design and control strategies' implementation for a three phase bidirectional EV charger using the DAB topology.
- Study and implementation of advanced modulation strategies for different AC-DC converter topologies used for bidirectional EV chargers in order to conduct a comparative study in terms of control performance, efficiency, total harmonic distortion, and design complexity.
- Study of the ability to provide more improved models for DC-DC converters (such as LLC and DAB) and AC-DC converters (such as Vienna) which will be closer to the real models by including different system parameters' effect (other harmonics, transformer, EMI,....)

A

Proof of the i_{rs} sign

The aim of this appendix is to give a proof for the formula (3.43) where i_{rs} is defined as only positive quantity and cannot be negative. First of all, (3.43) is based on (3.22) in which i_p could be seen as an amplitude of the series resonant current i_r.
The input voltage of the resonant tank V_{in} is expressed in (3.15). As a consequence, the resonant current i_r will be sinusoidal as well, with a RMS value I_{rm} and a phase shift angle ϕ with respect to the input voltage V_{in} as expressed in (A.1):

$$\begin{aligned} i_r(t) &= \sqrt{2} I_{rm} \sin(w_s t - \phi) \\ &= \sqrt{2} I_{rm} \cos\phi \sin(w_s t) - \sqrt{2} I_{rm} \sin\phi \cos(w_s t) \end{aligned} \tag{A.1}$$

Another way to express i_r is presented in (3.16). By identification, comparing (A.1) and (3.16), the following expression of i_{rs} (A.2) can be obtained:

$$i_{rs} = \sqrt{2} I_{rm} \cos\phi \tag{A.2}$$

It is now enough to prove that $\cos\phi$ is positive. To do this, the simplest way is to obtain the transfer function T_{vi} of the V_{in} and i_r in order to define $\cos\phi$. Based on Fig.3.1, T_{vi}

is given as follows (A.3):

$$\begin{aligned} T_{vi} = \frac{V_{in}}{i_r} &= (Z_{C_r} + Z_{L_r} + \frac{Z_{C_f} R}{Z_{C_f} + R_d})\, i_r \\ &= (L_r\, w_s - \frac{1}{C_r\, w_s})j + \frac{R_d}{1 + R_d C_f w_s j} \\ &= \frac{R_d}{1 + R_d^2 {C_f}^2 {w_s}^2} + (L_r\, w_s - \frac{1}{C_r\, w_s} - \frac{R_d^2 C_f w_s}{1 + R_d^2 {C_f}^2 {w_s}^2})j \\ &= Re(T_{vi}) + Im(T_{vi})\, j \end{aligned} \tag{A.3}$$

Where Re and Im are the real and imaginary part of T_{vi} respectively. Then, $\cos\phi$ can be defined as follows:

$$\cos\phi = \frac{Re(T_{vi})}{\sqrt{(Re(T_{vi}))^2 + (Im(T_{vi}))^2}} \tag{A.4}$$

Based on (A.3), it is clearly seen that $Re(T_{vi})$, which depends on R_d, C_f and w_s, is always positive that gives a positive $\cos\phi$. Thus, i_{rs} is also positive based on equation (**??**). Consequently, (3.43) is the unique expression of i_{rs}^*.

Bibliography

[1] XORZEMAR, "Overview of eMobility ecosystem CPO & EMP, electric vehicles and charging stations." Apr. 2020. [Online]. Available: https://www.youtube.com/watch?v=UNErmGXlNXI 9, 19

[2] M. Garcés Quílez, M. Abdel-Monem, M. El Baghdadi, Y. Yang, J. Van Mierlo, and O. Hegazy, "Modelling, analysis and performance evaluation of power conversion unit in g2v/v2g application—a review," *Energies*, vol. 11, no. 5, 2018. [Online]. Available: https://www.mdpi.com/1996-1073/11/5/1082 9, 20

[3] N. Vazquez and M. Liserre, "Peak current control and feed-forward compensation for the dab converter," in *2019 IEEE International Conference on Industrial Technology (ICIT)*, 2019, pp. 685–690. 12, 140

[4] S. M. S. I. Shakib and S. Mekhilef, "A frequency adaptive phase shift modulation control based llc series resonant converter for wide input voltage applications," *IEEE Transactions on Power Electronics*, vol. 32, no. 11, pp. 8360–8370, 2017. 19

[5] S. O. Showers and A. K. Raji, "Electric vehicles in south africa: Status and challenges," in *2021 IEEE PES/IAS PowerAfrica*, 2021, pp. 1–5. 19

[6] H. Chen, Z. Qian, R. Zhang, Z. Zhang, J. Wu, H. Ma, and X. He, "Modular Four-Channel 50 kW WPT System With Decoupled Coil Design for Fast EV Charging," *IEEE Access*, vol. 9, pp. 136 083–136 093, 2021. [Online]. Available: https://ieeexplore.ieee.org/document/9552889/ 20

[7] H. Wang, M. Shang, and A. Khaligh, "A psfb-based integrated pev onboard charger with extended zvs range and zero duty cycle loss," *IEEE Transactions on Industry Applications*, vol. 53, no. 1, pp. 585–595, 2017. 20

[8] D.-C. Urcan and D. Bica, "Integrating and modeling the Vehicle to Grid concept in Micro-Grids," in *International Conference on ENERGY and ENVIRONMENT (CIEM)*. Timisoara, Romania: IEEE, Oct. 2019, pp. 299–303. 21, 29, 30, 109

[9] F. Jarraya, A. Khan, A. Gastli, L. Ben-Brahim, and R. Hamila, "Design considerations, modelling, and control of dual-active full bridge for electric vehicles charging applications," *The Journal of Engineering*, vol. 2019, no. 12, pp. 8439–8447, Dec. 2019. [Online]. Available: https://onlinelibrary.wiley.com/doi/10.1049/joe.2018.5279 21

[10] A. Chub, D. Vinnikov, R. Kosenko, E. Liivik, and I. Galkin, "Bidirectional DC–DC Converter for Modular Residential Battery Energy Storage Systems," *IEEE Transactions on Industrial Electronics*, vol. 67, no. 3, pp. 1944–1955, Mars 2020. [Online]. Available: https://ieeexplore.ieee.org/document/8663606/ 22, 29, 30

[11] W. Feng and L. Yutao, "Modelling of a Power Converter with Multiple Operating Modes," *World Electric Vehicle Journal*, vol. 9, no. 1, p. 7, June 2018. [Online]. Available: http://www.mdpi.com/2032-6653/9/1/7 22, 29, 30, 47

[12] F. Krismer, J. Biela, and J. Kolar, "A comparative evaluation of isolated bi-directional DC/DC converters with wide input and output voltage range," in *Fourtieth IAS Annual Meeting. Conference Record of the Industry Applications Conference*, vol. 1, Hong Kong, China, Oct. 2005, pp. 599–606. 22, 29, 30

[13] S. S. Shah, V. M. Iyer, and S. Bhattacharya, "Exact Solution of ZVS Boundaries and AC-Port Currents in Dual Active Bridge Type DC–DC Converters," *IEEE Transactions on Power Electronics*, vol. 34, no. 6, pp. 5043–5047, June 2019. [Online]. Available: https://ieeexplore.ieee.org/document/8554182/ 22, 29

[14] Xiaodong Li and A. K. S. Bhat, "Analysis and Design of High-Frequency Isolated Dual-Bridge Series Resonant DC/DC Converter," *IEEE Transactions on Power Electronics*, vol. 25, no. 4, pp. 850–862, Apr. 2010. 22, 29

[15] N. Yildiran, "Design Methodology and Implementation of Half-Bridge LLC Resonant Converter," in *International Conference on Electrical, Communication, and Computer Engineering (ICECCE)*. Istanbul, Turkey: IEEE, Jun. 2020, pp. 1–6. 22, 30, 34, 110

[16] Y. Wei, Q. Luo, Z. Wang, and H. A. Mantooth, "A Complete Step-by-Step Optimal Design for *LLC* Resonant Converter," *IEEE Transactions on Power Electronics*, vol. 36, no. 4, pp. 3674–3691, April 2021. [Online]. Available: https://ieeexplore.ieee.org/document/9162487/ 22, 48, 49

[17] A. Hillers, D. Christen, and J. Biela, "Design of a Highly efficient bidirectional isolated LLC resonant converter," in *15th International Power Electronics and Motion Control Conference (EPE/PEMC)*, Novi Sad, Serbia, Sep. 2012. 22, 34, 67, 87

[18] G.-C. Hsieh, C.-Y. Tsai, and S.-H. Hsieh, "Design Considerations for LLC Series-Resonant Converter in Two-Resonant Regions," in *IEEE Power Electronics Specialists Conference*, Orlando, FL, USA, 2007, pp. 731–736. 22, 30, 34, 45

[19] Y. Wei, Z. Wang, Q. Luo, and H. Alan Mantooth, "Matlab gui based steady state open-loop and closed-loop simulation tools for different llc converters with all operation modes," *IEEE Open Journal of Industry Applications*, vol. 2, pp. 320–336, 2021. 22

[20] H. Al Attar, M. Ghanes, M. Hamida, and M. Taleb, "Control strategies design and comparison of dc-dc llc converter in v2x mode for electric vehicle charger application," in *2021 IEEE Conference on Control Technology and Applications (CCTA)*, 2021, pp. 1154–1159. 22, 27, 30, 56, 61, 66, 85, 90, 102, 110

[21] H. Al Attar, M. A. Hamida, M. Ghanes, and M. Taleb, "Llc dc-dc converter performances improvement for bidirectional electric vehicle charger application," *World Electric Vehicle Journal*, vol. 13, no. 1, 2022. 22, 27, 29, 30, 56, 110

[22] Y. Wei, D. Woldegiorgis, and A. Mantooth, "Control strategies overview for llc resonant converter with fixed frequency operation," in *2020 IEEE 11th International Symposium on Power Electronics for Distributed Generation Systems (PEDG)*, 2020, pp. 63–68. 22

[23] Q. Cao, Z. Li, B. Xue, and H. Wang, "Fixed frequency phase shift modulated llc resonant converter adapted to ultra wide output voltage range," in *2019 IEEE Applied Power Electronics Conference and Exposition (APEC)*, 2019, pp. 817–822. 22, 46

[24] S. De Simone, C. Adragna, C. Spini, and G. Gattavari, "Design-oriented steady-state analysis of LLC resonant converters based on FHA," in *International Symposium on Power Electronics, Electrical Drives, Automation and Motion, SPEEDAM*, Taormina, Italy, May 2006, pp. 200–207. 22, 44, 45, 57, 58

[25] H. Al Attar, M. Taleb, M. Ghanes, and A. Maloum, "Stratégie de commande psm d'un convertisseur dcdc llc par inversion de gain dans le mode v2x pour application ve," 2021. 26, 56

[26] H. Al Attar, M. Taleb, M. Hamida, and A. Maloum, "Stratégies de commande pwm d'un convertisseur dcdc llc par inversion de gain dans le mode v2x pour application ve," 2021. 27, 56

[27] H. Al Attar, M. Taleb, M. Hamida, and M. Ghanes, "Control performances improvement for bidirectional ev charger," 2021. 27, 111

[28] ——, "Adaptive control design of dc-dc llc converter with phase shift modulation in v2x mode for ev charger application," 2022. 27, 86

[29] ——, "Model free control design of dc-dc llc converter with phase shift modulation in v2x mode for ev charger application," 2022. 27, 86

[30] H. Al Attar, M. Hamida, M. Ghanes, J.-P. Barbot, and M. Taleb, "Adaptive control design and stability analysis of the bidirectional dc-dc llc converter," *IEEE Transactions on Control Systems Technology*, 2022. 27, 86

[31] H. Al Attar, M. Ghanes, M. Hamida, and M. Taleb, "Model free control design of dc-dc llc converter with phase shift modulation in v2x mode for ev charger application," in *2022 IEEE Conference on Control Technology and Applications (CCTA)*, 2022. 27, 86

[32] ——, "Electric vehicle charger control design combining phase shift modulation with an adaptive super twisting algorithm," in *2022 IEEE 16th International Workshop on Variable Structure Systems VSS*, 2022. 27, 86

[33] ——, "Bidirectional electric vehicle charger control design with performance improvement," in *2022 IEEE Conference of the Industrial Electronics Society (IECON)*, 2022. 28, 111

[34] ——, *DC-DC Converters: Modelling and Control Strategies*. Elsevier, 2023. 28, 30

[35] A. Fekik and N. Benamrouche, *Modeling and Control of Static Converters for Hybrid Storage Systems*. IGI Global, 2021. 29

[36] A. Fekik, H. Mohamed Lamine, H. Houassine, A. Azar, N. Kamal, H. Denoun, S. Vaidyanathan, and A. Sambas, *Power Quality Improvement for Grid-Connected Photovoltaic Panels Using Direct Power Control*, 01 2022, pp. 107–142. 29

[37] A. Fekik, M. L. Hamida, H. Denoun, A. T. Azar, N. A. Kamal, B. Amar, and N. Benamrouche, *Multilevel Inverter for Hybrid Fuel Cell/PV Energy Conversion System*. IGI Global, 2022. 29

[38] A. Vieira, L. Mazza, F. Antunes, and D. Oliveira, "Bidirectional dual-active-bridge DC-DC converter for vehicle-to-grid applications in DC microgrids," in *Simposio Brasileiro de Sistemas Eletricos (SBSE)*. Niteroi: IEEE, May 2018, pp. 1–6. 29

[39] W. G. Gerekial, "Bi-directional power converters for smart grids," Norwegian University of Science and Technology, Tech. Rep., Jun. 2014. 30, 36, 40

[40] H. Ma, Q. Liu, and J. Guo, "A sliding-mode control scheme for llc resonant DC/DC converter with fast transient response," in *IECON - 38th Annual Conference on IEEE Industrial Electronics Society*, Montreal, QC, Canada, Oct. 2012, pp. 162–167. 30, 40, 41, 42, 45, 85, 94

[41] L. Yao, D. Li, and L. Liu, "An improved large signal model of full-bridge LLC converter," *PLOS ONE*, vol. 13, no. 10, p. e0205904, Oct. 2018. 30, 40, 94

[42] Z. Fang, J. Wang, S. Duan, K. Liu, and T. Cai, "Control of an LLC Resonant Converter Using Load Feedback Linearization," *IEEE Transactions on Power Electronics*, vol. 33, no. 1, pp. 887–898, Jan. 2018. 30, 40, 41, 42, 45, 85, 94

[43] C. Liu, H. Liu, G. Cai, S. Cui, H. Liu, and H. Yao, "Novel Hybrid LLC Resonant and DAB Linear DC–DC Converter: Average Model and Experimental Verification," *IEEE Transactions on Industrial Electronics*, vol. 64, no. 9, pp. 6970–6978, Sep. 2017. 30, 40, 45

[44] D. Ravi, B. Reddy, S. Sudha Letha, and P. Samuel, "Bidirectional dc to dc Converters: An Overview of Various Topologies, Switching Schemes and Control Techniques," *International Journal of Engineering and Technology*, vol. 7, pp. 360–365, Sep. 2018. 31

[45] S. Y. Kim, H.-S. Song, and K. Nam, "Idling port isolation control of three-port bidirectional converter for evs," *IEEE Transactions on Power Electronics*, vol. 27, no. 5, pp. 2495–2506, 2012. 31

[46] T. Kang, C. Kim, Y. Suh, H. Park, B. Kang, and D. Kim, "A design and control of bi-directional non-isolated dc-dc converter for rapid electric vehicle charging system," in *2012 Twenty-Seventh Annual IEEE Applied Power Electronics Conference and Exposition (APEC)*, 2012, pp. 14–21. 31

[47] M. Yilmaz and P. T. Krein, "Review of battery charger topologies, charging power levels, and infrastructure for plug-in electric and hybrid vehicles," *IEEE Transactions on Power Electronics*, vol. 28, no. 5, pp. 2151–2169, 2013. 31

[48] S. TALBI, "Conception, Modélisation et Commande d'un Convertisseur DCDC Bidirectionnel pour le Stockage de l'Energie dans une Application Aéronautique | Modélisation, Information & Systèmes," 2019. 32

[49] Y. Gu, Z. Lu, L. Hang, Z. Qian, and G. Huang, "Three-level llc series resonant dc/dc converter," *IEEE Transactions on Power Electronics*, vol. 20, no. 4, pp. 781–789, 2005. 32

[50] R. Naayagi and A. Forsyth, "Bidirectional DC-DC converter for aircraft electric energy storage systems," in *5th IET International Conference on Power Electronics, Machines and Drives (PEMD 2010)*, Apr. 2010, pp. 1–6. 32, 33

[51] R. T. Naayagi, A. J. Forsyth, and R. Shuttleworth, "High-Power Bidirectional DC–DC Converter for Aerospace Applications," *IEEE Transactions on Power Electronics*, vol. 27, no. 11, pp. 4366–4379, Nov. 2012. [Online]. Available: http://ieeexplore.ieee.org/document/6135512/ 33

[52] X. Li and A. K. S. Bhat, "Analysis and Design of High-Frequency Isolated Dual-Bridge Series Resonant DC/DC Converter," *IEEE Transactions on Power Electronics*, vol. 25, no. 4, pp. 850–862, Apr. 2010, conference Name: IEEE Transactions on Power Electronics. 33, 34

[53] W. Chen, P. Rong, and Z. Lu, "Snubberless Bidirectional DC–DC Converter With New CLLC Resonant Tank Featuring Minimized Switching Loss," *IEEE Transactions on Industrial Electronics*, vol. 57, no. 9, pp. 3075–3086, Sep. 2010, conference Name: IEEE Transactions on Industrial Electronics. 35

[54] B. Zhao, Q. Song, W. Liu, and Y. Sun, "Overview of Dual-Active-Bridge Isolated Bidirectional DC–DC Converter for High-Frequency-Link Power-Conversion System," *IEEE Transactions on Power Electronics*, vol. 29, no. 8, pp. 4091–4106, Aug. 2014, conference Name: IEEE Transactions on Power Electronics. 35, 36

[55] J.-H. Jung, H.-S. Kim, M.-H. Ryu, and J.-W. Baek, "Design Methodology of Bidirectional CLLC Resonant Converter for High-Frequency Isolation of DC Distribution Systems," *IEEE Transactions on Power Electronics*, vol. 28, no. 4, pp. 1741–1755, Apr. 2013, conference Name: IEEE Transactions on Power Electronics. 36

[56] S. Tzafestas and G. Frangakis, "Design and implementation of pulse frequency modulation control systems," *Transactions of the Institute of Measurement and Control*, vol. 2, no. 2, pp. 65–78, Apr. 1980, publisher: SAGE Publications Ltd STM. 38

[57] A. Das, H. Nademi, and L. Norum, "A Pulse Width Modulation technique for reducing switching frequency for modular multilevel converter," in *India International Conference on Power Electronics 2010 (IICPE2010)*, Jan. 2011, pp. 1–6, iSSN: 2160-3170. 38

[58] Y. Liu, X. Wang, W. Qian, A. Janabi, B. Wang, X. Lu, K. Zou, C. Chen, and F. Z. Peng, "A Simple Phase-Shift Modulation Using Parabolic Carrier for Dual Active Bridge DC–DC Converter," *IEEE Transactions on Power Electronics*, vol. 35, no. 8, pp. 7729–7734, Aug. 2020, conference Name: IEEE Transactions on Power Electronics. 39

[59] C. Buccella, C. Cecati, H. Latafat, P. Pepe, and K. Razi, "Observer-Based Control of LLC DC/DC Resonant Converter Using Extended Describing Functions," *IEEE Transactions on Power Electronics*, vol. 30, no. 10, pp. 5881–5891, Oct. 2015. 40, 41, 42

[60] B. Cheng, F. Musavi, and W. G. Dunford, "Novel small signal modeling and control of an LLC resonant converter," in *IEEE Applied Power Electronics Conference and Exposition - APEC*, Fort Worth, TX, USA, Mar. 2014, pp. 2828–2834. 43

[61] Z. Shi, Y. Tang, Y. Guo, X. Li, and H. Sun, "Optimal design method of llc half-bridge resonant converter considering backflow power analysis," *IEEE Transactions on Industrial Electronics*, vol. 69, no. 4, pp. 3599–3608, 2022. 44

[62] G. Zhang, J. Zeng, S. S. Yu, W. Xiao, B. Zhang, S.-Z. Chen, and Y. Zhang, "Control design and performance analysis of a double-switched llc resonant rectifier for unity power factor and soft-switching," *IEEE Access*, vol. 8, pp. 44 511–44 521, 2020. 44

[63] F. Liu, X. Ruan, X. Huang, and Y. Qiu, "Second harmonic current reduction for two-stage inverter with dcx-llc resonant converter in front-end dc–dc converter: Modeling and control," *IEEE Transactions on Power Electronics*, vol. 36, no. 4, pp. 4597–4609, 2021. 44

[64] Y. Liao, G. Xu, Y. Sun, T. Peng, M. Su, B. Guo, and W. Xiong, "Single-stage dab-llc hybrid bidirectional converter with tight voltage regulation under dcx operation," *IEEE Transactions on Industrial Electronics*, vol. 68, no. 1, pp. 293–303, 2021. 44

[65] K. Zheng, G. Zhang, D. Zhou, J. Li, and S. Yin, "Modeling, Dynamic Analysis and Control Design of Full-Bridge LLC Resonant Converters with Sliding-Mode and PI Control Scheme," *Journal of Power Electronics*, vol. 18, no. 3, pp. 766–777, May 2018. 45

[66] A. Mansour, M. Hajer, B. Faouzi, and G. Jamel, "Analysis and Modeling of LLC Resonant Converter Used in Electric Vehicle," in *International Conference on Ad-*

vanced Systems and Emergent Technologies (IC_ASET). Hammamet, Tunisia: IEEE, Mar. 2019, pp. 357–362. 45

[67] F. Ajmal, H. Pan, C. He, G. Chen, and H. Chen, "Pulse-width modulation control strategy for high efficiency LLC resonant converter with light load applications," *IET Power Electronics*, vol. 7, no. 11, pp. 2887–2894, Nov. 2014. 45, 64, 65, 66

[68] Y. Dong, Y. Wang, F. Wang, and S. Wang, "Zero input current ripple llc resonant converter with integrated interleaved boost converter," in *2021 IEEE International Conference on Computer Science, Electronic Information Engineering and Intelligent Control Technology (CEI)*, 2021, pp. 602–606. 45, 110

[69] L. A. D. Ta, N. D. Dao, and D.-C. Lee, "High-efficiency hybrid llc resonant converter for on-board chargers of plug-in electric vehicles," *IEEE Transactions on Power Electronics*, vol. 35, no. 8, pp. 8324–8334, 2020. 45, 110

[70] M. Salem, V. K. Ramachandaramurthy, A. Jusoh, S. Padmanaban, M. Kamarol, J. Teh, and D. Ishak, "Three-phase series resonant dc-dc boost converter with double llc resonant tanks and variable frequency control," *IEEE Access*, vol. 8, pp. 22 386–22 399, 2020. 45, 110

[71] F. Zhang, Y. Wang, F. Wang, and C. Teng, "Pulse frequency modulation and unilateral dual-phase-shift hybrid control strategy for bidirectional full-bridge LLC resonant converter," *The Journal of Engineering*, vol. 2019, no. 16, pp. 3120–3126, Mar. 2019. 45, 67

[72] Z. Li, B. Xue, and H. Wang, "An interleaved secondary-side modulated llc resonant converter for wide output range applications," *IEEE Transactions on Industrial Electronics*, vol. 67, no. 2, pp. 1124–1135, 2020. 45

[73] S. Khan, D. Sha, X. Jia, and S. Wang, "Resonant llc dc–dc converter employing fixed switching frequency based on dual-transformer with wide input-voltage range," *IEEE Transactions on Power Electronics*, vol. 36, no. 1, pp. 607–616, 2021. 45

[74] A. Awasthi, S. Bagawade, and P. K. Jain, "Analysis of a hybrid variable-frequency-duty-cycle-modulated low-q llc resonant converter for improving the light-load efficiency for a wide input voltage range," *IEEE Transactions on Power Electronics*, vol. 36, no. 7, pp. 8476–8493, 2021. 45

[75] A. Mustafa and S. Mekhilef, "Dual phase llc resonant converter with variable frequency zero circulating current phase-shift modulation for wide input voltage range applications," *IEEE Transactions on Power Electronics*, vol. 36, no. 3, pp. 2793–2807, 2021. 45, 46

[76] M. Wang, S. Pan, X. Zha, J. Gong, W. Lin, J. Gao, and Q. Deng, "Hybrid control strategy for an integrated dab–llc–dcx dc–dc converter to achieve full-power-range zero-voltage switching," *IEEE Transactions on Power Electronics*, vol. 36, no. 12, pp. 14 383–14 397, 2021. 46

[77] S. M. Tayebi, H. Hu, S. Abdel-Rahman, and I. Batarseh, "Dual-input single-resonant tank llc converter with phase shift control for pv applications," *IEEE Transactions on Industry Applications*, vol. 55, no. 2, pp. 1729–1739, 2019. 46

[78] E. Tahoumi, F. Plestan, M. Ghanes, and J.-P. Barbot, "New robust control schemes based on both linear and sliding mode approaches: Design and application to an electropneumatic actuator," *IEEE Transactions on Control Systems Technology*, vol. 29, no. 2, pp. 818–825, 2021. 46

[79] C. A. Soriano-Rangel, W. He, F. Mancilla-David, and R. Ortega, "Voltage regulation in buck–boost converters feeding an unknown constant power load: An adaptive passivity-based control," *IEEE Transactions on Control Systems Technology*, vol. 29, no. 1, pp. 395–402, 2021. 46

[80] S. Zong, H. Luo, W. Li, X. He, and C. Xia, "Theoretical evaluation of stability improvement brought by resonant current loop for paralleled llc converters," *IEEE Transactions on Industrial Electronics*, vol. 62, no. 7, pp. 4170–4180, 2015. 46

[81] S. S. Shah, S. K. Rastogi, and S. Bhattacharya, "Paralleling of llc resonant converters," *IEEE Transactions on Power Electronics*, vol. 36, no. 6, pp. 6276–6287, 2021. 46

[82] Z. Fang, J. Wang, S. Duan, J. Shao, and G. Hu, "Stability analysis and trigger control of llc resonant converter for a wide operational range," *Energies*, vol. 10, no. 10, 2017. [Online]. Available: https://www.mdpi.com/1996-1073/10/10/1448 46

[83] S. Tian, F. C. Lee, and Q. Li, "Equivalent circuit modeling of llc resonant converter," *IEEE Transactions on Power Electronics*, vol. 35, no. 8, pp. 8833–8845, 2020. 46

[84] Z. Fang, T. Cai, S. Duan, and C. Chen, "Optimal Design Methodology for LLC Resonant Converter in Battery Charging Applications Based on Time-Weighted Average Efficiency," *IEEE Transactions on Power Electronics*, vol. 30, no. 10, pp. 5469–5483, October 2015. [Online]. Available: http://ieeexplore.ieee.org/document/6981942/ 47, 49

[85] R. Beiranvand, B. Rashidian, M. R. Zolghadri, and S. M. Hossein Alavi, "A Design Procedure for Optimizing the LLC Resonant Converter as a Wide Output Range Voltage Source," *IEEE Transactions on Power Electronics*, vol. 27, no. 8, pp. 3749–3763, August 2012. [Online]. Available: http://ieeexplore.ieee.org/document/6153061/ 47, 49

[86] Z. Liu, J. Du, and B. Yu, "Design Method of Double-Boost DC/DC Converter with High Voltage Gain for Electric Vehicles," *World Electric Vehicle Journal*, vol. 11, no. 4, p. 64, October 2020. [Online]. Available: https://www.mdpi.com/2032-6653/11/4/64 48

[87] T. Ahmadi, E. Rokrok, and M. Hamzeh, "Supervisory control of bipolar DC microgrids equipped with three-port multidirectional DC–DC converter for efficiency and system damping optimization," *Sustainable Energy, Grids and Networks*, vol. 16, pp. 327–340, December 2018. [Online]. Available: https://linkinghub.elsevier.com/retrieve/pii/S2352467718301942 48

[88] K. Bi, Y. Liu, Y. Zhu, and Q. Fan, "An impedance source modular DC/DC converter for energy storage system: analysis and design," *International Journal of Electrical Power & Energy Systems*, vol. 133, p. 107261, December 2021. [Online]. Available: https://linkinghub.elsevier.com/retrieve/pii/S0142061521005007 48

[89] R. Shi, S. Li, P. Zhang, and K. Y. Lee, "Integration of renewable energy sources and electric vehicles in V2G network with adjustable robust optimization," *Renewable Energy*, vol. 153, pp. 1067–1080, June 2020. [Online]. Available: https://linkinghub.elsevier.com/retrieve/pii/S0960148120302135 48

[90] Y. Dahmane, R. Chenouard, M. Ghanes, and M. Alvarado-Ruiz, "Optimized time step for electric vehicle charging optimization considering cost and temperature," *Sustainable Energy, Grids and Networks*, vol. 26, p. 100468, June 2021. [Online]. Available: https://linkinghub.elsevier.com/retrieve/pii/S2352467721000394 48

[91] S. Zorica, M. Vukšić, and T. Betti, "Design considerations of the multi-resonant converter as a constant current source for electrolyser utilisation," *International Journal of Electrical Power & Energy Systems*, vol. 111, pp. 237–247, October 2019. [Online]. Available: https://linkinghub.elsevier.com/retrieve/pii/S0142061518319860 48

[92] Y. Matsushita, T. Noguchi, K. Shimizu, N. Taguchi, and M. Ishii, "Control of Dual-Output DC/DC Converters Using Duty Cycle and Frequency," *World Electric Vehicle Journal*, vol. 11, no. 4, p. 72, November 2020. [Online]. Available: https://www.mdpi.com/2032-6653/11/4/72 48

[93] Y. Wei, Q. Luo, and A. Mantooth, "LLC Resonant Converter Design Based on the Worst Operation Point," in *2020 IEEE 11th International Symposium on Power Electronics for Distributed Generation Systems (PEDG)*. Dubrovnik, Croatia: IEEE, September 2020, pp. 219–224. [Online]. Available: https://ieeexplore.ieee.org/document/9244325/ 48, 49

[94] Y.-C. Liu, K.-D. Chen, C. Chen, Y.-L. Syu, G.-W. Lin, K. A. Kim, and H.-J. Chiu, "Quarter-Turn Transformer Design and Optimization for High Power Density 1-MHz *LLC* Resonant Converter," *IEEE Transactions on Industrial Electronics*, vol. 67, no. 2, pp. 1580–1591, February 2020. [Online]. Available: https://ieeexplore.ieee.org/document/8663607/ 48, 49

[95] G. K. Y. Ho, Y. Fang, and B. M. H. Pong, "A Multiphysics Design and Optimization Method for Air-Core Planar Transformers in High-Frequency

LLC Resonant Converters," *IEEE Transactions on Industrial Electronics*, vol. 67, no. 2, pp. 1605–1614, February 2020. [Online]. Available: https://ieeexplore.ieee.org/document/8691685/ 48, 49

[96] D. Ahmed and L. Wang, "Optimal Area-Product Model (OAPM) Based Non-Iterative Analytical Design Methodology for Litz-Wired High-Frequency Gapped-Transformer (LHFGT) in LLC Converters," *IEEE Access*, vol. 8, pp. 18 134–18 148, 2020. [Online]. Available: https://ieeexplore.ieee.org/document/8955851/ 48, 49

[97] R. Yu, G. K. Y. Ho, B. M. H. Pong, B. W.-K. Ling, and J. Lam, "Computer-Aided Design and Optimization of High-Efficiency LLC Series Resonant Converter," *IEEE Transactions on Power Electronics*, vol. 27, no. 7, pp. 3243–3256, July 2012. [Online]. Available: http://ieeexplore.ieee.org/document/6104164/ 48, 49

[98] M. Frivaldský, J. Kandráč, and P. Špánik, "Optimized design of the main circuit of LLC converter for high frequency application," in *2010 International Conference on Applied Electronics*, September 2010, pp. 1–4, iSSN: 1803-7232. 48, 49

[99] E. Khoobroo and M. Akhbari, "Optimal design of LLC series resonant converter with enhanced controllability characteristic," in *2012 3rd Power Electronics and Drive Systems Technology (PEDSTC)*. Tehran, Iran: IEEE, February 2012, pp. 392–396. [Online]. Available: http://ieeexplore.ieee.org/document/6183361/ 48, 49

[100] V. Monteiro, J. G. Pinto, and J. L. Afonso, "Operation Modes for the Electric Vehicle in Smart Grids and Smart Homes: Present and Proposed Modes," *IEEE Transactions on Vehicular Technology*, vol. 65, no. 3, pp. 1007–1020, Mar. 2016. [Online]. Available: http://ieeexplore.ieee.org/document/7273953/ 49

[101] D. C. Erb, O. C. Onar, and A. Khaligh, "Bi-directional charging topologies for plug-in hybrid electric vehicles," in *2010 Twenty-Fifth Annual IEEE Applied Power Electronics Conference and Exposition (APEC)*, 2010, pp. 2066–2072. 50

[102] O. Hegazy, J. Van Mierlo, and P. Lataire, "Control and analysis of an integrated bidirectional dc/ac and dc/dc converters for plug-in hybrid electric vehicle applications," *Journal of Power Electronics*, vol. 12, 07 2011. 50, 110

[103] K. Ribeiro de Faria Santos, "Design of a bidirectional on-board charger and a DC-DC converter for low voltage battery in Electric Vehicles," Theses, Université Paris-Saclay, Dec. 2020. [Online]. Available: https://tel.archives-ouvertes.fr/tel-03245704 50, 110

[104] W. W. Chen, "Bidirectional three-phase ac-dc power conversion using dc-dc converters and a three-phase unfolder," 2017. 50, 110

[105] B. Singh, V. Jain, Seema, A. Chandra, and K. Al-Haddad, "Power quality improvement in a pv based ev charging station interfaced with three phase grid," in *IECON 2021 – 47th Annual Conference of the IEEE Industrial Electronics Society*, 2021, pp. 1–6. 51

[106] F. Mohammadi, G.-A. Nazri, and M. Saif, "A bidirectional power charging control strategy for plug-in hybrid electric vehicles," *Sustainability*, vol. 11, no. 16, 2019. [Online]. Available: https://www.mdpi.com/2071-1050/11/16/4317 51

[107] N. Ali, Z. Liu, H. Armghan, and A. Armghan, "Double integral sliding mode controller for wirelessly charging of fuel cell-battery-super capacitor based hybrid electric vehicle," *Journal of Energy Storage*, vol. 51, p. 104288, 2022. [Online]. Available: https://www.sciencedirect.com/science/article/pii/S2352152X22003140 51

[108] A. S. Al-Ogaili, I. B. Aris, R. Verayiah, A. Ramasamy, M. Marsadek, N. A. Rahmat, Y. Hoon, A. Aljanad, and A. N. Al-Masri, "A three-level universal electric vehicle charger based on voltage-oriented control and pulse-width modulation," *Energies*, vol. 12, no. 12, 2019. [Online]. Available: https://www.mdpi.com/1996-1073/12/12/2375 51

[109] M. A. TALEB and A. MALOUM, "PROCEDE DE COMMANDE EN FREQUENCE DE LA TENSION D'ENTREE D'UN CONVERTISSEUR COURANT CONTINU-COURANT CONTINU - FR3083929A1 | PatentGuru," France Patent FR3 083 929A1, Jan., 2020. [Online]. Available: https://www.patentguru.com/FR3083929A1 58

[110] Seung-Hee Ryu, Dong-Hee Kim, Min-Jung Kim, Jong-Soo Kim, and Byoung-Kuk Lee, "Adjustable Frequency–Duty-Cycle Hybrid Control Strategy for Full-Bridge Series Resonant Converters in Electric Vehicle Chargers," *IEEE Transactions on Industrial Electronics*, vol. 61, no. 10, pp. 5354–5362, Oct. 2014. 66

[111] M. Fliess and C. Join, "Intelligent pid controllers," in *2008 16th Mediterranean Conference on Control and Automation*, 2008, pp. 326–331. 87, 88

[112] M. Fliess, C. Join, and H. Sira-Ramírez, "Complex continuous nonlinear systems: Their black box identification and their control," *14th IFAC Symposium on Identification and System Parameter Estimation*, vol. 39, no. 1, pp. 416–421, 2006. 88

[113] C. Buccella, C. Cecati, H. Latafat, P. Pepe, and K. Razi, "Observer-based control of llc dc/dc resonant converter using extended describing functions," *IEEE Transactions on Power Electronics*, vol. 30, no. 10, pp. 5881–5891, 2015. 94

[114] L. Zhang, H. Obeid, and S. Laghrouche, "Adaptive twisting controller for linear induction motor considering dynamic end effects," in *2018 15th International Workshop on Variable Structure Systems (VSS)*, 2018, pp. 19–24. 95

[115] Y. Shtessel, M. Taleb, and F. Plestan, "A novel adaptive-gain supertwisting sliding mode controller: Methodology and application," *Automatica*, vol. 48, no. 5, pp. 759–769, 2012. 95, 97, 98

[116] E. Tahoumi, F. Plestan, M. Ghanes, and J.-P. Barbot, "Adaptive exponent parameter: a robust control solution balancing between linear and twisting controllers,"

in *2018 15th International Workshop on Variable Structure Systems (VSS)*, 2018, pp. 186–191. 95

[117] L. Beghou, M. Popat, and S. MacDonald, "Pwm control of 3-phase pfc vienna rectifier derived from an average current-based control of single-phase pfc boost converter," in *2021 IEEE Energy Conversion Congress and Exposition (ECCE)*, 2021, pp. 3452–3459. 110

[118] P. Kvieska, A. Maloum, and L. Merienne, "Procédé de commande d'un redresseur triphasé pour un dispositif de charge embarqué sur un vehicule électrique ou hybride." France Patent FR3 058 592B1, Nov., 2018. 116, 117, 119

[119] Y. Park, S. Chakraborty, and A. Khaligh, "Dab converter for ev onboard chargers using bare-die sic mosfets and leakage-integrated planar transformer," *IEEE Transactions on Transportation Electrification*, vol. 8, no. 1, pp. 209–224, 2022. 136, 137, 143

[120] S. Dutta, S. Hazra, and S. Bhattacharya, "A digital predictive current-mode controller for a single-phase high-frequency transformer-isolated dual-active bridge dc-to-dc converter," *IEEE Transactions on Industrial Electronics*, vol. 63, no. 9, pp. 5943–5952, 2016. 136, 137, 143

[121] P. Nayak, S. Mandal, Y. Gupta, A. Shukla, and S. Doolla, "Improving the efficiency of the dab converter of an on-board ev charger using different modulation techniques," in *2020 IEEE International Conference on Power Electronics, Drives and Energy Systems (PEDES)*, 2020, pp. 1–6. 136

[122] C. K. gowda, V. G. Khedekar, N. Anandh, L. R. S. Paragond, and P. Kulkarni, "Bidirectional on-board ev battery charger with v2h application," in *2019 Innovations in Power and Advanced Computing Technologies (i-PACT)*, vol. 1, 2019, pp. 1–5. 136

[123] Y. Yan, H. Bai, A. Foote, and W. Wang, "Securing full-power-range zero-voltage switching in both steady-state and transient operations for a dual-active-bridge-based bidirectional electric vehicle charger," *IEEE Transactions on Power Electronics*, vol. 35, no. 7, pp. 7506–7519, 2020. 137, 143

[124] P. Guzmán, N. Vázquez, M. Liserre, R. Orosco, S. E. Pinto Castillo, and C. Hernández, "Two-stage modulation study for dab converter," *Electronics*, vol. 10, no. 21, 2021. [Online]. Available: https://www.mdpi.com/2079-9292/10/21/2561 137, 143

[125] G. Xu, D. Sha, J. Zhang, and X. Liao, "Unified boundary trapezoidal modulation control utilizing fixed duty cycle compensation and magnetizing current design for dual active bridge dc–dc converter," *IEEE Transactions on Power Electronics*, vol. 32, no. 3, pp. 2243–2252, 2017. 137, 143

[126] J. Hu, S. Cui, and R. W. De Doncker, "Natural boundary transition and inherent dynamic control of a hybrid-mode-modulated dual-active-bridge converter," *IEEE Transactions on Power Electronics*, vol. 37, no. 4, pp. 3865–3877, 2022. 137, 143

[127] J. Ding, G. Li, H. Zhang, A. Zhang, and J. Huang, "A novel dps control of dual active bridge dc-dc converters to minimize current stress and improve transient response," in *2021 33rd Chinese Control and Decision Conference (CCDC)*, 2021, pp. 2130–2135. 137, 143

[128] L. Martins, *Modelling and Analysis of DC-DC Converters for Bidirectional EV Charging Applications*. University of Sheffield, 2019. [Online]. Available: https://books.google.fr/books?id=SPLkzQEACAAJ 138, 139

[129] B. M. Kumar, A. Kumar, A. H. Bhat, and P. Agarwal, "Comparative study of dual active bridge isolated dc to dc converter with single phase shift and dual phase shift control techniques," in *2017 Recent Developments in Control, Automation & Power Engineering (RDCAPE)*, 2017, pp. 453–458. 140, 142

[130] M. Kim, M. Rosekeit, S.-K. Sul, and R. W. A. A. De Doncker, "A dual-phase-shift control strategy for dual-active-bridge dc-dc converter in wide voltage range," in *8th International Conference on Power Electronics - ECCE Asia*, 2011, pp. 364–371. 141

[131] J. Wu, D. Liu, Y. Wang, and Z. Chen, "A hybrid-bridge based dual active bridge dc/dc converter with compact structure," in *2020 IEEE 21st Workshop on Control and Modeling for Power Electronics (COMPEL)*, 2020, pp. 1–6. 141

[132] CIRTEM, "DAB charger study," 2021. 142

Titre : Contrôle du Chargeur Réversible pour Véhicule Electrique

Mot clés : Chargeur VE réversible, Convertisseur AC-DC, Convertisseurs DC-DC (LLC et DAB), Modulation par Fréquence d'Impulsion, Modulation par Décalage de Phase, Contrôle Non-linéaire Robuste.

Résumé : Dans cette thèse inscrite dans le cadre de la chaire Renault-Centrale Nantes, l'objectif est de concevoir des stratégies de contrôle pour améliorer les performances et le rendement du chargeur réversible du Véhicule Electrique (VE). Dans le mode décharge, le nouveau défi consiste à concevoir une stratégie de Modulation par Décalage de Phase (MDP) pour améliorer la zone de fonctionnement et le rendement du convertisseur DC-DC. La loi de commande est basée sur l'inversion de gain du convertisseur DC-DC LLC. Du point de vue coût, la contribution porte essentiellement sur la conception d'une stratégie d'optimisation pour diminuer le dimensionnement du convertisseur DC-DC LLC mais aussi d'améliorer les performances de la stratégie de Modulation par Fréquence d'Impulsion (MFI).

Ensuite, un développement d'un modèle grand signal du convertisseur LLC basé sur la stratégie MDP est élaboré. La contribution principale consiste à implémenter des stratégies du contrôle robuste, telles que la commande sans modèle et la commande adaptive super twisting, combinées avec la stratégie MDP.

D'autre part, l'apport principal conduit à fournir une stratégie de contrôle hybride du chargeur afin de réguler la tension du bus DC dans les zones de saturation du convertisseur DC-DC.

Enfin, une nouvelle topologie d'un chargeur VE avec la structure DAB est étudiée. Une stratégie de contrôle en cascade est proposée pour régler le bus DC et le courant réseau. Différentes stratégies de modulation, telles que les modulations par décalage d'un ou de deux déphasages, sont étudiées.

Des résultats de simulation de modèles de chargeurs réels sont présentés afin de mettre en évidence l'efficacité des stratégies de contrôle proposées.

Title: Bidirectional Electric Vehicle Charger Control

Keywords: Bidirectional EV charger, AC-DC converter, DC-DC converters (LLC and DAB), Pulse Frequency Modulation, Phase Shift Modulation, Robust Non-linear Control.

Abstract: In this thesis, part of the chair Renault/Centrale Nantes, the aim is to design control strategies to improve the performance and efficiency of the bidirectional charger of the Electric Vehicle (EV). In the discharging mode, the new challenge is to design a Phase Shift Modulation (PSM) strategy to improve the operating zone and efficiency of the DC-DC converter. The control law is based on the DC-DC LLC gain inversion. In terms of cost, the contribution is mainly about the design of an optimization strategy, not only to reduce the sizing of the DC-DC LLC converter, but also to improve the performance of the Pulse Frequency Modulation (PFM) strategy.

Then, a large signal model of the LLC converter based on the PSM strategy is developed. The main contribution consists of implementing robust control strategies, such as model-free control and adaptive super twisting control, combined with the PSM strategy.

On the other hand, the key contribution leads to provide a hybrid control strategy of the charger in order to be able to regulate the DC bus voltage in the saturation zones of the DC-DC converter.

Finally, a new topology of an EV charger with the DAB structure is studied. A backstepping control strategy is proposed to regulate the DC bus voltage and the grid current. Different modulation strategies, such as single and dual phase shift modulation, are studied.

Simulation results of real charger models are presented in order to highlight the effectiveness of the proposed control strategies.